IDŐJÁRÁS

QUARTERLY JOURNAL
OF THE HUNGARIAN METEOROLOGICAL SERVICE

CONTENTS

****

http://www.met.hu/Journal-Idojaras.php

VOL. 116 * NO. 4 * OCTOBER – DECEMBER 2012

IDŐJÁRÁS

Quarterly Journal of the Hungarian Meteorological Service

Editorial Office: Kitaibel P.u. 1, H-1024 Budapest, Hungary
P.O. Box 38, H-1525 Budapest, Hungary
E-mail: journal.idojaras@met.hu
Fax: (36-1) 346-4669

Indexed and abstracted in Science Citation Index Expanded™ and Journal Citation Reports/Science Edition
Covered in the abstract and citation database SCOPUS®

Subscription by

mail: IDŐJÁRÁS, P.O. Box 38, H-1525 Budapest, Hungary
E-mail: journal.idojaras@met.hu

IDŐJÁRÁS

Quarterly Journal of the Hungarian Meteorological Service
Vol. 116, No. 4, October–December 2012, pp. 237–251

Environmental modeling using graphical processing unit with CUDA

Róbert Mészáros[1], **Ferenc Molnár Jr.**[2], **Ferenc Izsák**[3], **Tibor Kovács**[4], **Péter Dombovári**[5], **Ákos Steierlein**[1], **Roland Nagy**[1], and **István Lagzi**[6]*

[1] *Department of Meteorology, Eötvös Loránd University, Pázmány Péter sétány 1/A, H-1117 Budapest, Hungary*

[2] *Department of Physics, Applied Physics and Astronomy, Rensselaer Polytechnic Institute, 110 Eighth Street, Troy,12180-New York, USA*

[3] *Department of Applied Analysis and Computational Mathematics, Eötvös Loránd University, Pázmány Péter sétány 1/A, H-1117 Budapest, Hungary*

[4] *Institute of Radiochemistry and Radioecology, University of Pannonia, Egyetem u. 10, H-8200 Veszprém, Hungary*

[5] *Department of Radiation Protection, Nuclear Power Plant of Paks, P.O.Box. 71, H-7031 Paks, Hungary*

[6] *Department of Physics, Budapest University of Technology and Economics, Műegyetem rkp. 3, H-1111 Budapest, Hungary*

**Corresponding author E-mail: istvanlagzi@gmail.com*

(Manuscript received in final form May 14, 2012)

Abstract—Modeling transport and deposition processes of toxic materials in the atmosphere is one of the most challenging environmental tasks. These numerical simulations with dispersion models are very time consuming, therefore, their acceleration is extremely important. One possible, effective solution for increasing the computational time can be the parallelization of the source codes. At the same time, the technological improvement of graphics hardware created a possibility to use desktop video cards to solve numerically intensive tasks. In this study, we present a new and powerful parallel computing structure for solving different environmental model simulations using the graphics processing units (GPUs) with CUDA (compute unified device architecture). Two different types of dispersion models were developed and applied based on this

technology: a stochastic Lagrangian particle model and an Eulerian model. We present and discuss the results and advantages of both methods. A Lagrangian particle model was applied to simulate the transport of radioactive pollutants from a point source after a hypothetical accidental release at local scale. In addition, an Eulerian model was used to simulate sulfur dioxide transport and transformation in the troposphere at regional scale. Moreover, in both cases, CPU and GPU computational times were also compared. We can achieve typical acceleration values in the order of 80–120 times in case of Lagrangian model and 30–40 times in case of Eulerian model using this new parallel computational framework compared to CPU using a single-threaded implementation. Next to the obvious advantages, the barriers of this new method are also discussed in this study.

Key-words: environmental modeling; accidental release; air pollution; CUDA; GPU computing

1. Introduction

Protecting the environment and developing new green technologies are among the most important issues of the society that should be addressed in this century. Computer aided models already assist many aspects of our everyday life as well as our future, and are important drivers of our decisions. Their presence in environmental sciences continuously serves the society in short term practical decisions, e.g., through weather forecasts (*Csima* and *Horányi*, 2008) or air pollution modeling (*Leelőssy et al.*, 2011; *Mészáros et al.*, 2011) as well as in concluding global consequences affecting several generations, e.g., modeling and simulation of climate change and their impacts on global and regional environment (*Bartholy et al.*, 2008; *Torma et al.*, 2008). It is well-known that environmental model simulations must have a high degree of accuracy and must be achieved faster than in real time to be of use in decision support (*Lagzi et al.*, 2004; *Mészáros et al.*, 2010). In the past few years, the graphics processing unit (GPU) has became a powerful tool for parallel computing and both performance and capabilities of GPUs have increased noticeably (e.g., *Stone et al.*, 2007; *Liu et al.*, 2008; *Preis et al.*, 2009; *Block et al.*, 2010; *Komatitsch et al.*, 2010; *Preis*, 2011). NVIDIA created a parallel computing framework, the so-called compute unified device architecture (CUDA) to utilize this performance and simplify programming of general purpose computations (NVIDIA, 2011).

We have developed applications of GPU using CUDA framework for environmental studies serving as a basement for decision-making strategies. A stochastic Lagrangian model was developed on CUDA to estimate the transport and transformation of the radionuclides from a single point source during hypothetical accidental releases. With the Lagrangian particle model (*Molnár et al.*, 2010) the dispersion of radionuclides was simulated in a 30 km radius circle around the Paks Nuclear Power Plant (Hungary). This advanced computational platform is used by the Paks NPP as a part of the nuclear safety system called TREX (Transport–Exchange) model (*Mészáros et al.*, 2010, *Molnár et al.*, 2011). Our other environmental application of GPU with CUDA was the

simulation of the atmospheric dispersion and transformation of sulfur dioxide using an Eulerian modeling system.

In this study, we present the efficiency and barriers of calculations on GPU in case of environmental tasks, compared the advantages of this new technique during the applications of Lagrangian and Eulerian modeling methods.

2. CUDA

The parallel computing model of CUDA is fundamentally different from previous parallel computers. Supercomputer architectures, clusters, and grids share the property that each node is responsible only for one, or a few number of threads (sequence of instructions), and generally, they may execute different computations. In contrast, a CUDA program defines thousands of threads for a single GPU, all of which are executing the same computation (the kernel function) on different data elements. These threads are lightweight in the sense that they only coordinate the distribution of the computational work to the physical computing units. Threads are grouped into blocks, which are always executed by a single multiprocessor. However, a GPU usually contains several multiprocessors, allowing many blocks (and threads within) to run simultaneously. On the level of multiprocessors, the threads of a block are executed in a time-sliced way in small batches called *warps*; different blocks are scheduled one after another on available multiprocessors. This scheduling and executing procedure takes place at every kernel launch, but gives practically zero overhead.

The two-level of splitting a computation into blocks, and further into threads is not arbitrary. Threads within a single block can synchronize their execution using a barrier, and they may share data via the common *shared memory* (*Fig. 1*). However, threads from different blocks cannot communicate with each other directly, because the order of block allocation and execution on multiprocessors is arbitrarily decided by the GPU. The only guaranteed barrier between executions of blocks is the completion of a kernel function: a new kernel is not launched until all blocks from the previous kernel launch are finished.

There are many memory resources available, optimized for various purposes on the video card. The most important is the *global memory*, which is essentially the large RAM available on the video card (*Fig. 1*). It can be accessed by any threads at any time, and it is responsibility of the programmer to avoid writing the same address at the same time. This is where the main data of the computation is located. From here, threads read the data, process it, and write back the results during a kernel execution. Further, there are cached memory areas, which provide read-only data for the threads. These are optimized for a specific reading pattern, e.g., the *constant memory* is optimized

to provide data to all threads at the same time, the *texture memory* is optimized to provide interpolated sampling of 2D or 3D data in a localized region for threads of the same block (*Fig. 1*). All of these memory areas are accessible from the host (the CPU-part of the program).

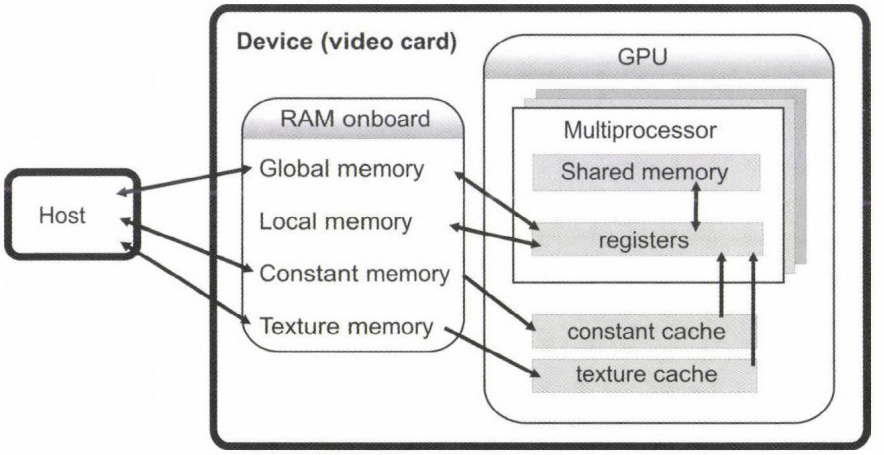

Fig. 1. The structure of a video card.

In order to create optimal CUDA applications, one needs to understand the proper usage and limitations of resources, and follow development guidelines, which are detailed in the programming guide of CUDA (*NVIDIA CUDA Programming Guide*). Here we only provided a brief overview of the most important features that will be explicitly mentioned in our applications.

3. Models

3.1. Lagrangian particle model

A stochastic Lagrangian particle model was developed for simulating accidental release of radionuclides on local scale. This model type has an advantage on local scale simulations, because it can handle steep gradient of emitted species near a point source (*Bartnicki et al.*, 2003; *Lepicard et al.*, 2004; *Molnár et al.*, 2010). In the Lagrangian model, individual particles are released from a point source in each time step. Each particle represents a given mass or activity, and they can be moved in space by advection (wind field) and turbulent diffusion, they can transform to other species (by radioactive decay), and particles can be removed from the atmosphere to the surface via dry and wet deposition pathways. This means that the model is continuous in space and discontinuous

in time. In this model, the advection is deterministic, but the effect of the turbulent diffusion is stochastic. The new spatial position of the particles can be calculated by the following equations:

$$X_i^{new} = X_i^{old} + v_i^{adv}\Delta t + \tilde{x}_i, \tag{1}$$

where X_i^{new} and X_i^{old} are the spatial coordinates of particles after and before the time step, respectively. v_i^{adv} is the ith coordinate of the wind velocity vector, Δt is the time step (10 s in the model simulation). The last term in the Eq. (1) ($\tilde{x}_i$) describes the effect of stochastic, turbulent processes, and i denotes the spatial dimension (i = 1, 2, 3). The stochastic term is calculated by

$$\tilde{x}_i = (rand)\sqrt{2K_i\Delta t}\,. \tag{2}$$

Random numbers (*rand*) with normal distribution (with mean 0.0 and variance 1.0) were generated using Mersenne Twister random number generator and Box-Muller transformation. K_i is the turbulent diffusion coefficient in each direction. For horizontal dispersion a constant value was used ($K_x = K_y = 100\ \mathrm{m^2 s^{-1}}$). Vertical diffusion coefficient (K_z) depends on the height, and it was calculated using the Monin–Obuhov similarity theory.

Released radioactive particles can decay and deposit by dry and wet pathways. The probability that individual particles during a time step Δt will decay or deposit can be estimated by the following relation:

$$p = 1 - e^{-k\Delta t}, \tag{3}$$

where k is either the radioactive decay constant or wet or dry deposition constant. These constants depend on the chemical nature of the toxic species. During dry deposition, particles can deposit below the mixing layer height. Wet deposition occurs only in case of precipitation.

Implementing a single-threaded CPU version of the model is straightforward. Assuming that the emission profile (the amount of emitted particles in every time step) for all species and the maximum number of particles released during the simulation are known, activities or masses can be a priori assigned to the particles. The maximum number of particles is the dominant variable that affects simulation time and precision. It is limited only by available memory. In every iteration, the main steps for every particle are the same: interpolating (sampling) meteorological data obtained from a numerical weather prediction model in x, y, z, and time dimensions using linear

interpolation, calculating the turbulent diffusion coefficient, moving the particle by the wind, then by turbulent diffusion, and finally testing for dry and wet depositions. Particles may become inactive, meaning they are no longer moved by wind or turbulent diffusion, when the particle is deposited or it reaches the predefined boundaries of the simulated area. Activities or masses of particles were summarized on a rectangular grid for visualization and further statistical evaluation.

In the parallelized CUDA version of the program, we utilize the various memory types available. Meteorological data are loaded into three-dimensional textures, to utilize the hardware-implemented trilinear interpolation. Since the meteorological data are four-dimensional (3 space and 1 time), an extra interpolation step is necessary. Using texture memory is also useful because the plume usually propagates in a specific direction, giving the required spatial locality for the texture cache to work efficiently. Physical constants of the isotopes are loaded to constant memory. Shared memory is used for caching the particle data (position, state information). The data is loaded from global memory to shared memory when a kernel starts, and written back at the end, if data was modified.

The calculations in each time step are done by two kernel functions. First step is generating random numbers, using the Mersenne Twister random number generator. A large buffer (on the GPU) is used to store the numbers, because the random number generator works more efficiently if large amount of numbers is asked for at once. The second step is the main kernel. Each thread is responsible for updating the status of a single particle. First, particle information and random numbers are loaded from global memory to shared memory. Second step is sampling the meteorological data, interpolating in vertical direction, and calculating the turbulent diffusion coefficient using the Monin–Obukhov similarity theory. These results are stored in shared memory. Next step is moving the particles by wind field and turbulent diffusion, and testing for radioactive decay and deposition. This step uses the interpolated outputs of weather prediction model and the random numbers for calculation of turbulent motion, radioactive decay, and stochastic deposition. The final step is writing the changed particle information back to global memory.

3.2. Eulerian model – solving reaction-advection-diffusion equations

Solving reaction-advection-diffusion equations fits to the architecture of CUDA as well. The atmospheric reaction-advection-diffusion equation can be written in the following form:

$$\frac{\partial c}{\partial t} = -\nabla(\vec{u}c) + K\nabla^2 c + R + E - D, \tag{4}$$

where c is the concentration of the chemical species, $\vec{u}$ is the 3D wind velocity, K is the turbulent diffusion coefficient, R is the reaction term, which usually contains non-linear functions, E is the emission term, and D is the deposition term, which usually contains the effect of the dry and wet deposition processes. Solving diffusion-advection equations to describe the spread and/or transformation of air pollutants is a very time consuming computational task. The numerical simulations must be obviously achieved faster than in real time in order to use them in decision support. A feasible way is the parallelization of the source code using supercomputers, clusters, GRID, or GPU (*Martin et al.*, 1999; *Alexandrov et al.*, 2004; *Lovas et al.*, 2004).

During our simulations, a standard "method of line" technique was used to solve Eq. (4). The "method of lines" technique has two consecutive steps, the first is a spatial discretization of the partial differential equations followed by a temporal integration of the produced ordinary differential equations with an upwind approximation to provide a stable solution.

Our Eulerian model has 32 horizontal layers and each layer contains 96×90 equidistant grid cells (this mesh covers the central part of Europe). No-flux (Neumann) boundary condition was applied for chemical species at the boundary of the computational domain. Meteorological data (wind field, surface temperature, cloud coverage, relative humidity, mixing layer height) were obtained from the ALADIN limited area weather prediction model operated at the Hungarian Meteorological Service. The model calculates the energy balance and the Monin–Obukhov length from which the vertical turbulent diffusion coefficient can be estimated. The vertical turbulent diffusion coefficient plays an important role in the vertical mixing of pollutants. Therefore, its parameterization is one of the most important tasks in the air pollution modeling. However, it should be noted that the contribution of the horizontal turbulence to the mass transport of pollutants comparing to the effect of the advection is negligible. Horizontally, the transport is mostly governed by the wind field.

In the CUDA implementation, concentrations of the species in a simulation can be stored in global memory on the device. We can assign computation of the next time level to a kernel function, assigning threads to compute individual grid points. The rectangular space represented by the grid points can easily be split to smaller parts, which can be assigned to blocks. Shared memory within a block utilized in the approximation of the spatial derivatives, because this computation requires data which belongs to neighboring grid points (and threads). Physical constants and other parameters of a simulation can be stored in the constant memory.

The communication between threads, required by the computation of spatial derivatives, gives a challenging optimization task. Access to the shared memory must be coordinated by barrier synchronization, and for optimal execution, the bank structure of the shared memory must be

considered as well. Further, in order to provide communication between spatially neighboring blocks, a layer of grid points must overlap between the blocks. This gives non-contiguous memory addressing of grid points in the threads of blocks, which causes a significant performance drop on the first generation of CUDA devices. A sophisticated solution (*Molnár et al.*, 2011) is required to maintain optimal performance. Nevertheless, the coordination and communication between threads gives a significant (but unavoidable) overhead to the computations.

4. Results

Since the particles (in fact particle packages) are independent in the Lagrangian model, there is no communication, and therefore, no synchronization is necessary between threads. This allows us to split the computation arbitrarily on a very fine-grained level, specifically, in a way to best fit to the capabilities of the GPU. Additionally, the trilinear interpolation provided by the hardware significantly reduces the amount of computation needed per particle, while this is a necessary computation on the CPU. These factors lead to about 80–120 times speedup on a first-generation device (GeForce 8800GTX) and about 100–140 times speedup on a second-generation device (GeForce GTX 275) compared to the single-threaded CPU computation (on a 2.33 GHz Core 2 CPU). This means, for example, that in case of an accidental release, a Lagrangian particle model simulation takes 2 hours on CPU, but it decreases to only 1 minute using GPU.

Fig. 2 shows an example of the plume structure and the deposited amount of the I-131 isotope originated from the Paks Nuclear Power Plant in a hypothetical accidental release. For this simulation the stochastic Lagrangian particle model was used. In the figure, the structures of a radioactive plume in a homogeneous wind field at different wind velocities are presented. It can be noticed that a Lagrangian particle model can also be used at low wind velocity, where the traditional Eulerian or Gaussian models cannot handle the extremely steep concentration gradient of chemical species near the point source. This low wind speed causes unpredictable plume profile in Gaussian models and numerical instability in Eulerian models near the source due to the high concentration gradients. Therefore, this approach can be successfully used to describe the air pollution transport from a single, but strong emission source even in regional scale.

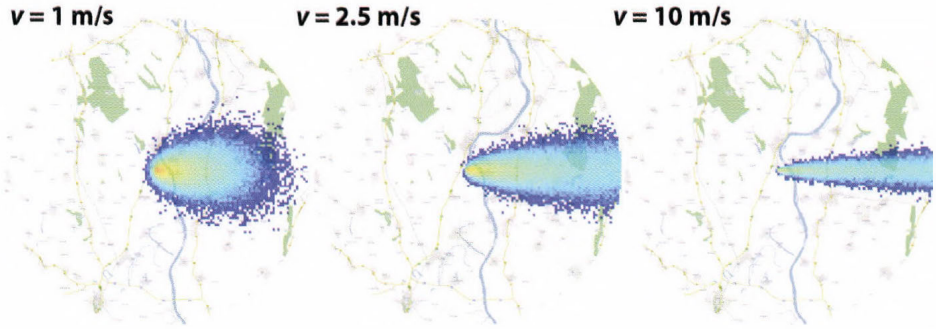

Fig. 2. Accidental release of I-131 isotope at the Paks Nuclear Power Plant using a stochastic Largangian particle model at different wind velocities.

At the same time, in regional scale, the Eulerian models could be more appropriate tools for dispersion simulations, as they can more easily handle the 3D meteorological fields on a previously defined grid. To illustrate the capacity and power of Eulerian models, we developed a model, which can calculate the spread and chemical transformation of air pollutants in the atmosphere. Here, we present the results of model simulations for sulfur dioxide (SO_2) emitted from area sources. Emission inventory of the European Monitoring and Evaluation Programme (EMEP) for SO_2 was used and converted from the EMEP to the model grid (*Fig. 3*), and we supposed a continuous emission rate in the simulations. The exact heights of the emission sources are unknown, therefore, we assumed that the emitted amount of SO_2 was distributed evenly in the model layers in the lower 100 m. A simple, first order chemical reaction was considered to describe the transformation of SO_2 to sulfate aerosol ($R = -k_r c$; $k_r = 1.083 \times 10^{-5}$ s^{-1}) (*Luria et al.*, 2001; *Woo et al.*, 2003), and dry deposition was also considered as a first order chemical reaction ($D = k_{dry} c$; $k_{dry} = 6.38 \times 10^{-4}$ s^{-1}). A homogeneous initial condition was used in the domain with $[SO_2]_0 = 0.01$ mg/m^3.

Fig. 4 shows the spatial distribution of the SO_2 in the surface layer (first layer) over the central part of Europe in daytime and night. We can see higher concentration near strong emitting sources (south Poland, Romania), which is a trivial consequence of the SO_2 dispersion and chemical transformation. However, we can clearly see that the average concentration in the surface layer is higher at daytime than at night. This is attributed to the fact that the height of the mixing layer is much smaller at nighttime than in daytime because of the lack of irradiation, therefore, a large part of the emitted SO_2 remains above the mixing layer at night.

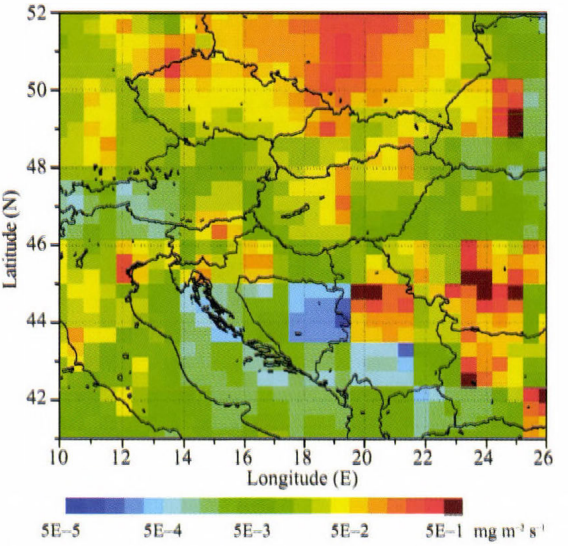

Fig. 3. EMEP Emission inventory of sulfur dioxide used in the Eulerian model.

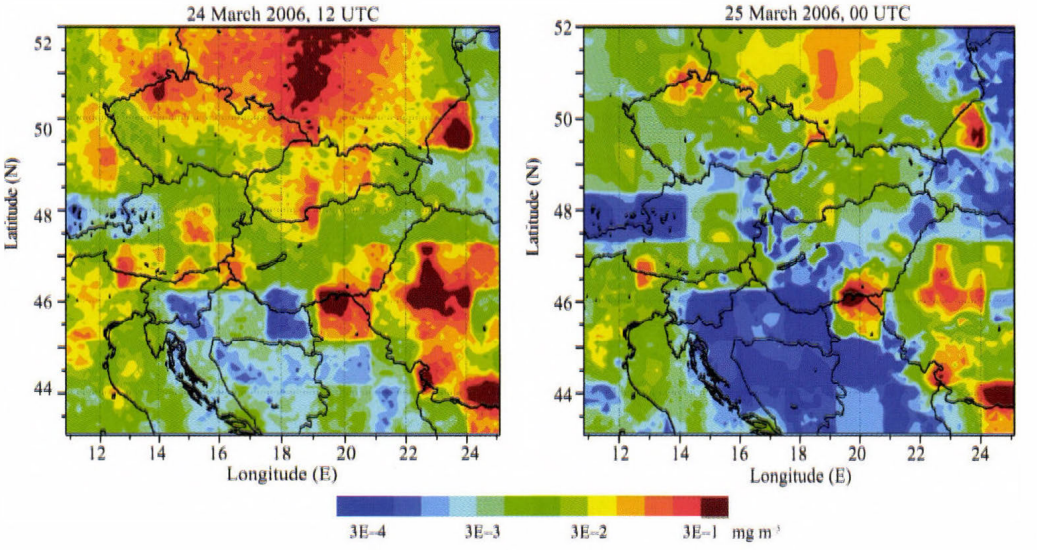

Fig. 4. Concentration of sulfur dioxide in the surface layer on March 24, 2006, at 12 UTC and March 25, at 00 UTC.

An important aspect of a model development is the validation of the model results against the field measurements. *Fig. 5* shows the modeled SO_2 concentration and the observed one at an EMEP monitoring station in Illmitz. The calculated concentration values are in a good accordance with the observed concentrations. Moreover, the Eulerian model could also capture the temporal variation of the SO_2.

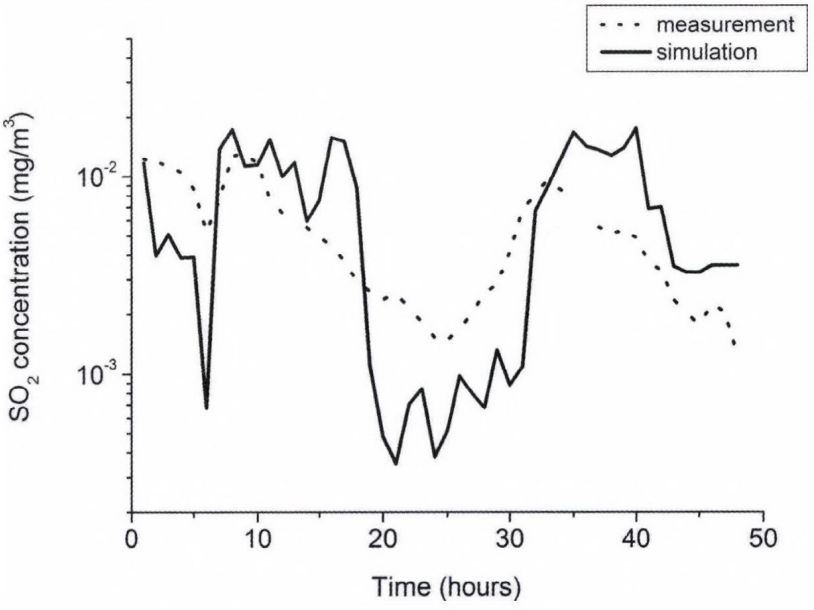

Fig. 5. Measured and modeled concentration of sulfur dioxide in the surface layer at Illmitz EMEP monitoring station (47° 46'N, 16° 46'E). Simulation started on March 24, 2006, at 00 UTC.

The application of GPU in case of Eulerian model was also investigated. We can achieve speedups up to 20–25 times on first-generation devices (GeForce 8800GTX) and 30–40 times on second-generation devices (GeForce GTX 275) compared to the single-threaded CPU implementation (2.33 GHz Core 2 CPU). We should emphasize, however, that this model is fundamentally different from the Lagrangian model; this is essentially a PDE solver using finite difference method, while the Lagrangian model is more like a Monte-Carlo-type simulation. The speedups alone should not be used to compare these models, because we need different amounts of computation to reach the same quality of results.

5. *Conclusions*

In this paper we showed and discussed the capability of two types of models, Lagrangian and Eulerian. Most of the models used in environmental protection and air quality management fall into these two categories. Therefore, it is important to know the real advantages and drawbacks of the applied models. From results presented in this study, we can clearly see that if we estimate the dispersion of pollutants from a strong point source in local scale, a Lagrangian particle model should inevitably be used. This model has the main advantage that the positions of each particle are continuous functions in space. This can overcome the problem of steep concentration gradients arising near a point source, and the Lagrangian particle model can be used even in case of extremely low wind speed, where other models (Gaussian, Eulerian) simply fail and they cannot provide a stable and/or realistic solution. On the other hand, the main problem with this approach is that each particle represents a given mass or activity (in case of radionuclides), therefore, it is very hard to obtain a continuous physical quantity, like concentration with small number of particles, and increasing this number results in an increase in computational time. Using Lagrangian particle model to simulate the transport of air pollutants from multi-emission sources is practically impossible because of huge computational task. However, this task is really suitable for Eulerian models, and they can easily provide and calculate continuous quantities. Eulerian models can be predominantly used to calculate the transport of chemical species from multi-emission sources. In this framework, the chemical reactions occurring between chemical species can be easily handled, because the chemical rate can be calculated from concentrations, which are prognostic variables in Eulerian models. Modeling of the chemical interactions between particles in Lagrangian models is very challenging task, and it involves consideration of the stochastic nature of chemical reactions. In conclusion, the model should always be chosen to a given air pollution problem to provide accurate and cost-efficient solution. Development of such cost-efficient strategies requires very accurate calculations, and numerical simulations need a huge computational effort.

There are numerous solutions to address this issue. Parallelization of the models and using supercomputers, clusters, or grid systems to solve problems is a common technique. These systems are built by connecting numerous processors, either by some sort of direct link or by a network connection. Several computing centers can be connected to each other by the Internet, thus creating grids. We investigated a new parallel computational framework to solve environmental related problems using graphical processing unit. We developed a stochastic Lagrangian particle model and an Eulerian model on CUDA to estimate the transport and transformation of the radionuclides from a single point source during hypothetical accidental releases. Our results show that parallel implementation achieves typical acceleration values in the order of a

hundred times in case of Lagrangian model and tens of times in case of Eulerian model compared to CPU using a single-threaded implementation on a regular desktop computer (*Fig. 6*). The relatively high speedup with no additional costs to maintain this parallel architecture could result in a wide usage of GPU for diversified environmental applications in the near future.

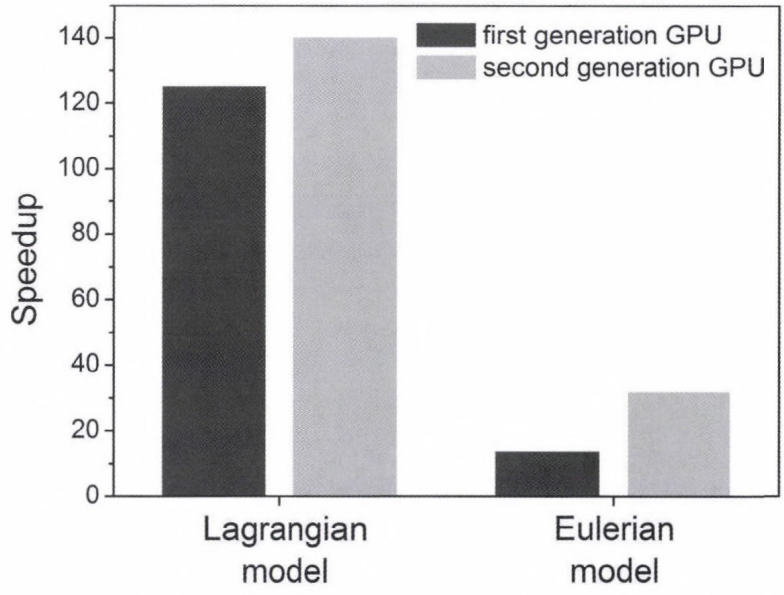

Fig. 6. Speedup of different applications on first and second generation CUDA-capable video cards (GeForce 8800 GTX and GeForce GTX 275, respectively) compared to CPU (2.33 GHz Core 2).

We should also mention some important aspects of this technology. In the past years, as this technology has developed, many papers have been published (for as review see *Lee et al.*, 2010), and it seems that the "speedup" gained over general CPU solutions has become the measure of CUDA technology. However, one must be very careful to interpret such results correctly. There are numerous parameters that formulate the final performance gain over the CPU, such as the GPU type, clock frequency, number of CUDA cores, amount of memory, speed of memory on the video card, CPU type, CPU clock, host memory amount and speed, and most importantly, the implementation of the algorithm itself. These together make it almost impossible to predict a given computational speedup when ported to CUDA. Some of the published works show speedups of several hundred times (*Lee et al.*, 2010). This is never the "magical" power of CUDA, it is always the result of the unoptimized CPU code which serves as the basis of comparison. Paper published by *Lee et al.* (2010) carries important information:

you can achieve great optimizations on CPU if you have enough experience and expertise, bringing down the relative performance gain of GPU solutions. This can be close to what you could expect by looking at the raw hardware performance of CPUs and GPUs. However, the amount of computational and programming knowledge required to do so, is usually so large, that only computer scientists of specific fields can afford to learn them. This is why CUDA has gained much popularity among scientists from different fields: with relatively limited (but still advanced) knowledge of CPU and GPU programming, the CUDA solution is much faster than the CPU solution. This is the main advantage of CUDA (together with its cost-effectiveness).

We believe that using GPU – as a new computational tool – will revolutionize the environmental computing and can provide a new, cost–efficient, and effective technique in environmental protection. This system can be effectively used, and hence, the most profitable it would be in simulation of an accidental release of hazardous materials from industrial facilities (e.g., nuclear power plants). The recent accident at the Fukushima Nuclear Power Plant highlights the importance of predicting accidental release of toxic materials (*Bolsunovsky* and *Dementyev*, 2011; *Leelőssy et al.*, 2011; *Manolopoulou et al.*, 2011; *Sinclair et al.*, 2011). Implementing a model using this easy-to-maintain and cost-efficient computational framework in all facilities storing hazardous materials would be realistic and could help to decrease environmental consequences of possible future accidents.

Acknowledgments—Authors acknowledge the financial support of the Hungarian Research Found (OTKA K81933, K81975, K104666, NK100296, and PD 104441) and the European Union and the European Social Fund (TÁMOP 4.2.1./B-09/KMR-2010-0003).

References

Alexandrov, V.N., Owczarz, W., Thomson, P.G. and *Zlatev, Z.*, 2004: Parallel runs of a large air pollution model on a grid of Sun computers. *Math. Comput. Simulat.*, *65*, 557–577.

Bartholy, J., Pongrácz, R., Gelybó, G. and *Szabó, P.*, 2008: Analysis of expected climate change in the Carpathian Basin using the PRUDENCE results. *Időjárás*, *112*, 249–264.

Bartnicki, J., Saltbones, J. and *Foss, A.*, 2003: Performance of the SNAP model in an ENSEMBLE exercise of simulating real-time dispersion from a nuclear accident. *Int. J. Environ. Pollut. 20*, 1–6, 22–32.

Bolsunovsky, A. and *Dementyev, D.*, 2011: Evidence of the radioactive fallout in the center of Asia (Russia) following the Fukushima nuclear accident. *J. Environ. Radioact.*, doi:10.1016/j.jenvrad.2011.06.007.

Block, B., Virnau, P. and *Preis, T.*, 2010: Multi-GPU accelerated multi-spin Monte Carlo simulations of the 2D Ising model. *Comput. Phys. Commun. 181*, 1549–1556.

Csima, G. and *Horányi, A.*, 2008: Validation of the ALADIN-Climate regional climate model at the Hungarian Meteorological Service. *Időjárás 112*, 155–177.

Komatitsch, D., Erlebacher, G., Goddeke, D. and *Michea, D.*, 2010: High-order finite-element seismic wave propagation modeling with MPI on a large GPU cluster. *J. Comput. Phys. 229*, 7692–7714.

Lagzi, I., Kármán, D., Turányi, T., Tomlin, A.S. and *Haszpra, L.*, 2004: Simulation of the dispersion of nuclear contamination using an adaptive Eulerian grid model, *J. Environ. Radioactiv. 75*, 59–82.

Lee, V.W., Kim, C., Chhugani, J., Deisher, M., Kim, D., Nguyen, A.D., Satish, N., Smelyanskiy, M., Chennupaty, S., Hammarlund, P., Singhal, R. and *Dubey, P.*, 2010: Debunking the 100X GPU vs. CPU myth: an evaluation of throughput computing on CPU and GPU. In: ISCA '10 Proceedings of the 37th annual international symposium on Computer architecture, ACM New York, NY, USA, 451–460.

Leelőssy, Á., Mészáros, R. and *Lagzi, I.*, 2011: Short and long term dispersion patterns of radionuclides in the atmosphere around the Fukushima Nuclear Power Plant, *J. Environ. Radioactiv. 102*, 1117–1121.

Lepicard, S., Heling, R. and *Maderich, V.*, 2004: POSEIDON/RODOS models for radiological assessment of marine environment after accidental releases: application to coastal areas of the Baltic, Black and North Seas. *J. Environ. Radioactiv. 72*, 153–161.

Liu, W., Schmidt, B., Voss, G. and *Müller-Wittig, W.*, 2008: Accelerating molecular dynamics simulations using Graphics Processing Units with CUDA. *Comput. Phys. Commun. 179*, 634–641.

Lovas, R., Kacsuk, P., Lagzi, I. and *Turányi, T.*, 2004: Unified development solution for cluster and Grid computing and its application in chemistry. *Lect. Notes Comp. Sc. 3044*, 226–235.

Luria, M., Imhoff, RE., Valente, RJ., Parkhurst, W.J., and *Tanner, R.L.*, 2001: Rates of conversion of sulfur dioxide to sulfate in a scrubbed power plant plume. *J. Air Waste Manag. Assoc. 51*, 1408–1413.

Mészáros, R., Vincze, Cs. and *Lagzi, I.*, 2010: Simulation of accidental release using a coupled transport (TREX) and numerical weather prediction (ALADIN) model. *Időjárás 114*, 101–120.

Mészáros, R., Leelőssy, Á., Vincze, Cs., Szűcs, M., Kovács, T. and *Lagzi. I.*, 2011: Estimation of the dispersion of an accidental release of radionuclides and toxic materials based on weather type classification *Theor. Appl. Climatol.* DOI: 10.1007/s00704-011-0482-0

Manolopoulou, M., Vagena, E., Stoulos, S., Ioannidou, A. and *Papastefanou, C.*, 2011: Radioiodine and radiocesium in Thessaloniki, Northern Greece due to the Fukushima nuclear accident. *J. Environ. Radioact. 102*, 796–797.

Martin, M., Oberson, O., Chopard, B., Mueller, F. and *Clappier, A.*, 1999: Atmospheric pollution transport: the parallelization of a transport & chemistry code. *Atmos. Environ. 33*, 1853–1860.

Molnár, F., Szakály, T., Mészáros, R. and *Lagzi, I.*, 2010: Air pollution modelling using a Graphics Processing Unit with CUDA. *Comput. Phys. Commun. 181*, 105–112.

Molnár, F., Izsák, F., Mészáros, R. and *Lagzi, I.*, 2011: Simulation of reaction-diffusion processes in three dimensions using CUDA. *Chemometr. Intell. Lab. 108*, 76–85.

NVIDIA CUDA Programming guide, NVIDIA corporation
http://developer.download.nvidia.com/compute/cuda/2_1/toolkit/docs/NVIDIA_CUDA_Programming_Guide_2.1.pdf.

Preis, T., Virnau, P., Paul, W. and *Schneider, J.J.*, 2009: GPU accelerated Monte Carlo simulation of the 2D and 3D Ising model. *J. Comput. Phys. 228*, 4468–4477.

Preis, T., 2011: GPU-computing in econophysics and statistical physics. *Eur. Phys. J.- Spec. Top. 194*, 87–119.

Sinclair, L.E., Seywerd, H.C.J., Fortin, R., Carson, J.M., Saull, P.R.B., Coyle, M.J., Van Brabant, R.A., Buckle, J.L., Desjardins, S.M. and *Hall, R.M.*, 2011: Aerial measurement of radioxenon concentration off the west coast of Vancouver Island following the Fukushima reactor accident. *J. Environ. Radioact.*, Doi:10.1016/j.jenvrad.2011.06.008.

Stone, J.E., Phillips, J.C., Freddolino, P.L., Hardy, D.J., Trabuco, L.G. and *Schulten, K.*, 2007: Accelerating molecular modeling applications with graphics processors. *J. Comput. Chem. 28*, 2618–2640.

Torma, C., Bartholy, J., Pongrácz, R., Barcza, Z., Coppola, E. and *Giorgi, F.*, 2008: Adaptation of the RegCM3 climate model for the Carpathian Basin. *Időjárás 112*, 233–247.

Woo, J.-H., Baek, J.M., Kim, J.-W., Carmichael, G.R., N. Thongbooncho, N., Kim, S.T., An, J.H., 2003: Development of a multi-resolution emission inventory and its impact on sulfur distribution for Northeast Asia. *Water Air Soil Pollut. 148*, 259–278.

IDŐJÁRÁS

Quarterly Journal of the Hungarian Meteorological Service
Vol. 116, No. 4, October–December 2012, pp. 253–280

Numerical study of the impact of the changes in the tropospheric temperature profile on the microphysics, dynamics and precipitation of mid-latitude summer continental convective clouds

Angelina Brandiyska[1], **Rumjana Mitzeva**[2]*, **Boryana Tsenova**[3], and **John Latham**[4,5]

[1] *Geophysical Institute, Acad. Bonchev str, Bl. 3, 1113 Sofia, Bulgaria*
imdnme@gmail.com

[2] *Faculty of Physics, University of Sofia, James Bourchier blv, 1164 Sofia, Bulgaria*
rumypm@phys.uni-sofia.bg

[3] *National Institute of Meteorology and Hydrology,*
66 Tsarigradsko chausse, 1784 Sofia,Bulgaria,
boryana.tsenova@meteo.bg

[4] *MMM Division, NCAR, 3450 Mitchell Lane, Boulder, 80301 Colorado, USA,*

[5] *SEAES, University of Manchester, Manchester, M13 9PL,UK*
latham@ucar.edu

**Corresponding author*

(Manuscript received in final form October 25, 2012)

Abstract—This paper investigates the effect of the expected changes of tropospheric temperature profile on the dynamical and microphysical characteristics of individual summertime convective storms and on the processes of precipitation development in these storms. Two dynamically different clouds (a 'big' and a 'small' one) were simulated with the Regional Atmospheric Modeling System (RAMS v6.0). The differences between simulations of the clouds, developed in a present-day and in a modified environment are discussed. Macro- and microphysical evolution is examined in detail, and the changes in precipitation intensity and total rainfall volume are explained physically as a consequence of the temperature increase in the upper troposphere. Results show that the warming leads to a decrease of precipitation in the 'small' cloud case, while in the 'big' cloud case, warming leads to the increase of precipitation. The detailed analysis reveals that the main reason for the opposite direction of the impact of the projected tropospheric changes on different sized clouds lies in the ice phase evolution.

Key-words: climate warming, convective cloud, numerical model, RAMS

1. Introduction

In the scientific community, it is expected that the projected global warming will give rise to greater frequency and severity of extreme precipitation events, as stated in the Report of the Intergovernmental Panel on Climate Change (IPCC, 2007), based on studies such as *Semenov* and *Bengtsson*, 2002; *Kharin* and *Zwiers*, 2005; *Meehl et al.*, 2006 and others. *Trenberth et al.*, 2003 studied different methods of assessing the impact of various thermodynamical factors on precipitation, and concluded that the increased moisture content as a result of climate warming would have a significant impact on precipitation amount and intensity. As extreme precipitation relates to increases in moisture content and due to the nonlinearities involved with the Clausius-Clapeyron relationship, for a given increase of temperature, the projected increase of extreme precipitation is more pronounced than the mean precipitation increase (*Allen* and *Ingram*, 2002). In mid-latitude continental regions, summertime precipitation falls mainly from convective clouds with a great vertical extent, often supplemented by lightning, hail, floods. Obviously, changes in extreme local weather events are connected to the airmass properties – changes occurring in temperature and humidity, their vertical profiles or concentration and size of aerosols. *McCaul et al.* (2005), using RAMS model, examined the sensitivity of supercell storms to environmental temperature by changing only the temperature at the lifting condensation level with convective available potential temperature and other parameters being fixed. Their simulations indicate that in the limit of their assumptions, the updraft speed and precipitation efficiency are higher at a colder environment, while the peak precipitation rate in a warmer environment is comparable to that in colder environment. Numerical simulations of *Takemi* (2010), by Advanced Research WRF model reveal the dependence of the precipitation intensity in mesoscale convective systems on the temperature lapse rate. In the frame of their model simulations they found that with the increase of the lapse rate the mean precipitation intensity increases and the maximum precipitation intensity decreases. They stress on the need for diagnosis of stability in climate simulations and the need to investigate further the effects of cloud microphysics on the production of precipitation in a given temperature environment. To clarify this question, preliminary investigations on the impact of change in temperature and humidity profiles on microphysical characteristics of convective storms and on the processes of precipitation development would be of use. In *Mitzeva et al.* (2008) the influence of global warming on convective cloud dynamics and microphysics is investigated with a 1.5 D cloud model and compared with the influence of the pollution represented by CCN concentration. Their results show that in warmer profile temperature more vigorous cloud form, with larger cloud, rain water, and ice content.

In the present study, the impact of changes in tropospheric temperature and humidity profiles on individual summertime convective continental cloud

development and precipitation is investigated. Numerical simulations are performed with RAMS (regional atmospheric modeling system) and changes of temperature and humidity are imposed on a reference sounding. Two clouds were simulated which are formed with the same meteorological conditions, but triggered by different sized thermal bubbles. The simulated clouds dynamical evolution, hydrometeor mixing ratios, and resulting precipitation are evaluated in detail. The analysis focuses on clarifying the changes in the process of formation of precipitation, with emphasis on the ice phase process. The present study is a first step for testing whether and how temperature profile changes would affect convective clouds development without pretending to be sufficient for the drawing of general conclusions.

2. Cloud model

The model used in the present study is the Regional Atmospheric Model System (RAMS v.6.0), which is developed by the Colorado State University and is widely used as a research tool for numerical studies of thunderstorms (*Pielke et al.*, 1992; *Cotton et al.*, 2003). It combines the capabilities of different types of atmospheric models, from mesoscale to large eddy simulations. RAMS is a 3-dimensional non-hydrostatic cloud resolving atmospheric model. It includes equations and parameterizations for a wide range of physical processes, as it is designed as a comprehensive meteorological modeling system: advection, diffusion, turbulence, radiation, and large-scale precipitation; it also includes a land surface model and a bulk microphysics scheme for resolved clouds and precipitation. Spatial resolution can vary from hundreds of meters to hundreds of kilometers and the time-step can be fixed or varying, user-defined, or automatically calculated by the model.

The two-moment bulk microphysics scheme in RAMS predicts both mass mixing ratio and number concentration of hydrometeor species thus allowing the mean diameter of hydrometeors to evolve. (*Meyers et al.*, 1997). CCN number concentration is defined in the beginning of the run and it is kept constant during the simulations. The size distribution of aerosols is included indirectly through the shape of the cloud droplet spectrum. Cloud droplet as well as other hydrometeor spectra are approximated by a gamma function, which depends on prognosed mean radius and number concentration, and it has a fixed shape.

Sensitivity studies (e.g., *Demott et al.*, 1994; *Van den Heever et al.*, 2006; *Phillips et al.,* 2007, and others) show that nucleation processes are fundamental microphysics processes that must be routinely included in cloud schemes to capture the lifecycle of convective clouds. For the present simulations, since we focus on the impact of the temperature profile changes on cloud formation and development by simulating idealized convective clouds, CCN concentration and

gamma shape parameters for different hydrometeor species are selected in an appropriate way to represent microphysical conditions typical for mid-latitude continental climate.

In the model, seven species of hydrometeors are categorized: cloud droplets, rain, pristine ice, snow, aggregates, graupel, and hail. Cloud droplets and pristine ice nucleate from vapor and may convert into other categories after they grow. Together, pristine ice and snow categories represent a bimodal distribution of ice crystals. Graupel has higher density than snow but still consists mostly of ice and can carry only a small percentage of liquid. If the percentage of liquid is higher than 30%, the ice particle is considered as hail – the highest density hydrometeor formed by freezing of raindrops, riming or partial melting of graupel. The fall speeds of the hydrometeors vary depending on diameter and category. Note, that the definitions of graupel and hail categories in the model emphasize their composition and density rather than their method of formation. Thus, a melting graupel particle will increase its liquid fraction and density, and it will be categorized as hail.

Apart from nucleation, vapor deposition, riming, and melting, coalescence is also taken into account by using pre-calculated look-up tables that contain approximate solutions of the stochastic collection equation. The two-moment scheme also includes breakup of raindrops (formulated into the collection efficiency), diagnosis of pristine ice and snow habit dependent on temperature and saturation, evaporation and melting of each species. Details of microphysical parameterization can be found in *Meyers et al.*, (1997).

3. Numerical simulations

In the present study, in order to lower the computational expense of the experiments, some of the schemes in the model are switched off (short-wave and long-wave radiation, soil model). They do not have significant influence on processes of such space and time scales like single convective storms. The microphysics parameters are selected in a way to represent an urban region with a mid-latitude continental climate. The hydrometeor shape-parameters as well as other initialization parameters are shown in *Table 1*. The time step is automatically calculated by the model, depending on the resolution.

The model domain dimensions are 30 × 30 × 15.5 km consisting of 50 × 50 × 60 points with 600 m grid spacing in a Lambert conformal projection. It covers the area of Sofia City with center point latitude/longitude of 42.65 N/23.38 E. The topography is simplified to a flat surface with elevation of 595 m above sea level. The vertical coordinate is terrain-following sigma coordinate with level thickness ΔZ increasing from 30 m at ground level to 300 m in the free troposphere with a stretch ratio of 1.25. Initial conditions (at the surface) are horizontally homogeneous and are taken from the aerological sounding

measurement in Sofia on 14 July 2006 – a day when a (moderate) thunderstorm was observed, or from the modified sounding.

Table 1. Forcing conditions of the numerical simulations

Parameter	Value
Horizontal resolution	600m
Vertical resolution at z=0m	30m
Vertical resolution above z=2000m	300m
Large time step	4s
Small time step	1s
CCN number	$1.0*10^9$ #/m^3
gamma shape parameter, cloud droplets	3.0
gamma shape parameter, raindrops	2.0
gamma shape parameter, pristine crystals	1.5
gamma shape parameter, snow	2.0
gamma shape parameter, aggregates	2.0
gamma shape parameter, graupel	2.0
gamma shape parameter, hail	2.0
Thermal bubble amplitude (ΔT)	2K
Thermal bubble relative humidity ratio	1.2
Thermal bubble horizontal size	3km; 4.2km
Thermal bubble vertical size	1.1km; 1.7km

Boundary conditions are open. Simulations were carried out for one hour starting at 12:00 UTC. A real sounding was used in order to assure that the environmental conditions chosen for model simulation are adequate for thunderstorm formation, rather than to simulate the real thunderstorm that developed over Sofia. Clouds were initiated by introducing a warm moist bubble at the surface. The so called "thermal bubble" had 2 K temperature excess and 20% higher relative humidity compared to the environmental air. By varying the thermal bubble's horizontal and vertical dimensions, two convective clouds were simulated – cloud A, simulated with initial bubble size of $4.2 \times 4.2 \times 1.7$ km and cloud B, simulated with initial bubble size of $3 \times 3 \times 1.7$ km. Thus, our study is an idealized modeling study. As a result of an appropriate choice of the initial conditions, two typical (for mid-latitude) single summer continental precipitating clouds were simulated. Hereafter, we will call them 'big' and 'small', because one (cloud A) is bigger than the other (cloud B). The 'control simulation' is the simulation carried out with the original sounding from July 14, 2006, for cloud A (simulated with the larger thermal bubble) and for cloud B (simulated with the smaller thermal bubble). The modifications of the temperature profile used in the present study (*Fig. 1*) are based on IPCC,

2007 and *Santer et al.*, (2003). IPCC climate projections predict an increase of global mean surface temperature from 2 to 6 °C till the end of the 21th century. The investigations of *Santer et al.*, (2003) reveal that temperature changes with height depend on latitude and the temperature increase in the upper troposphere for the mid-latitudes is about 1.5 times greater than the surface temperature with maximum around 300 mb. Due to the very limited studies and no clear trend in relative humidity (*Elliot* and *Angell*, 1997) in our simulations the dew-point temperature profile was modified to keep the relative humidity in accordance to the original sounding, i.e., the relative humidity was not modified.

The control simulation (with the original sounding) is hereafter denoted as ΔT=0 and the simulations with two modified profiles are denoted as ΔT=3 and ΔT=5 respectively, where the numbers 3 and 5 refer to the surface temperature increase in degrees Celsius. The original sounding is shown in Fig.1a and the modification of temperature profile is shown in *Fig. 1b*. The relative humidity is not modified among the runs.

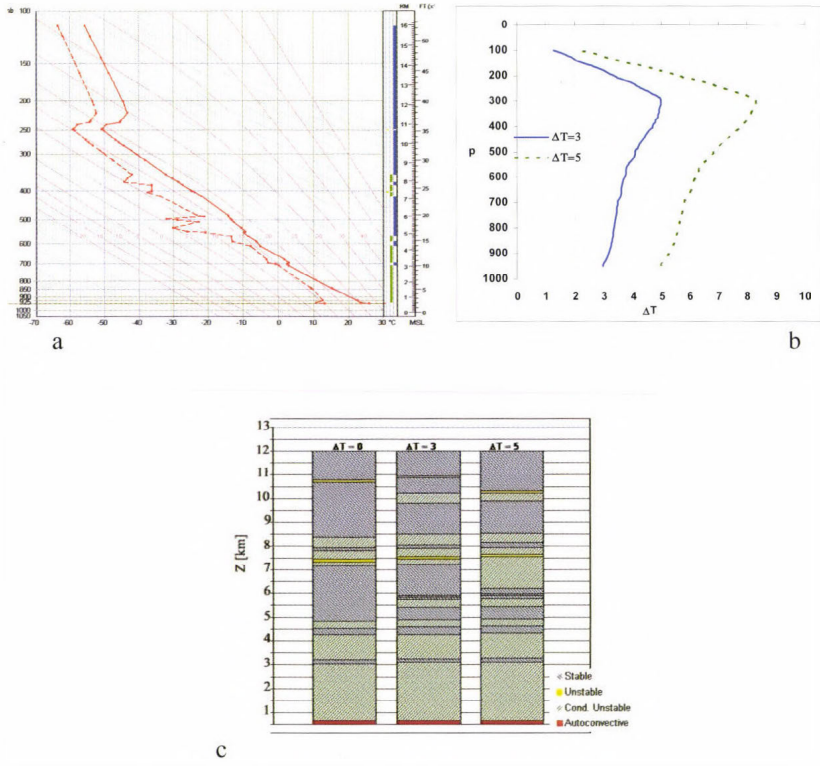

Fig. 1. a) Aerological sounding from 14 July 2006; b) increase of temperature ΔT used for the simulations of global warming; c) atmospheric stability for the simulated cases with ΔT=0, ΔT=3, ΔT=5, Z is in km ASL.

The original sounding is characterized by alternating moist conditionally unstable and stable layers (*Fig. 1c*), evaluated using the temperature lapse rate. The instability increases above 5.3 km in ΔT=3 and ΔT=5. This tendency is most pronounced in the layers between 6.1 km and 7.2 km in ΔT=5. In the original sounding, the zero isotherm is located at 3.6 km. The modifications lead to its upward displacement, at 4.1 km for ΔT=3 and 4.6 km for ΔT=5, respectively. The temperature interval where homogeneous freezing occurs is also shifted upward in the warmer environment. The 40 °C isotherm in the original sounding is at 9.4 km AGL above ground level, while for ΔT=3 it is at 10 km AGL and for ΔT=5 - at 10.3 km AGL. Due to the assumption that the relative humidity is kept constant with the warming, the condensation level is almost at the same altitude (around 1.7 km AGL). However, the temperature at cloud base (even at the same altitude) is higher with the warming modification.

4. Results

The results are presented in the following manner. First, we consider the dynamical and microphysical characteristics of cloud A ('big' cloud), simulated with the reference sounding. After that, the same characteristics of simulations ΔT=3 and ΔT=5 are analyzed, pointing to the differences between them and the control one. The analysis of cloud B ('small' cloud) is presented in the same way.

Cloud A simulated with the reference sounding has a maximum cloud top height of 12 km above ground level (AGL) and maximum updraft speed of 24 m/s. Its anvil is well above the level of maximum heating in warming scenarios. The smaller cloud (cloud B) simulated with the reference sounding has maximum cloud top at 10 km AGL and maximum updraft speed of 18 m/s.

4.1. Cloud A

4.1.1. Macro- and microphysical evolution of the control cloud

Condensation starts at 9 min model time (MT) at 1726 m above ground level (AGL), at temperature 14.2 °C. The cloud grows during the following 12 minutes (*Fig. 2*) and at 21 min MT the cloud top reaches the tropopause (10.7 km AGL). During the rapid growth stage (18–21 min), two maximums of the vertical velocity are visible in *Fig. 3*. At 18 min MT, these maximums can be seen at ~5 km AGL (21 m/s) and at ~7 km AGL (24 m/s), respectively. The sounding instability and high moisture (*Fig. 1*) provide the energy needed to accelerate the updraft. The level of the maximum water mixing ratio (*Fig. 2*) coincides with the level of the first updraft velocity maximum (*Fig. 3*). A slight decrease in velocity at 18 min MT is seen between 5 and 6 km in *Fig. 3*, due to the

dry and stable environment. The analyses reveal that above 6 km AGL (–14 °C), intensive freezing occurs and the updraft speed increases again. Between 18 and 21 min MT the cloud top reaches the layer above 7 km AGL where the moisture increases (*Fig. 1*) and the environment is unstable. The main reason for the increase of updraft velocity above 9 km AGL (*Fig. 3*) is the latent heat released by homogeneous freezing.

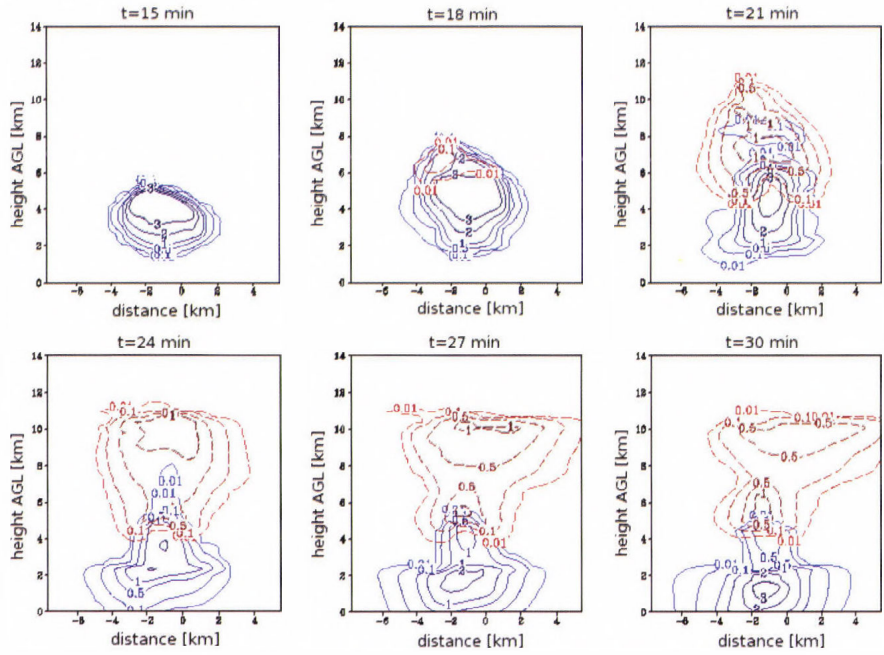

Fig. 2. Cloud A: sum of rain and cloud water mixing ratios (solid) and sum of pristine ice, snow, and aggregates mixing ratios (dashed) in the control simulation (ΔT=0)

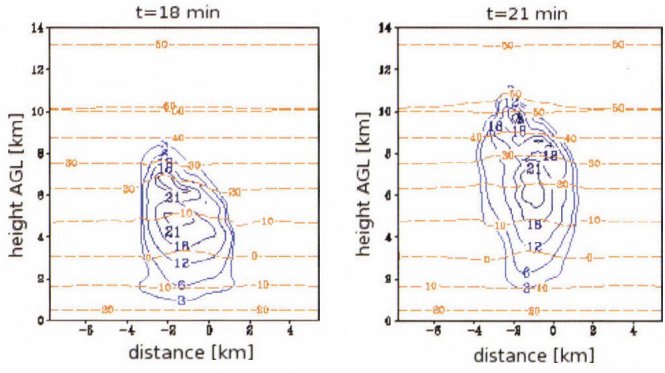

Fig. 3. Cloud A: updraft velocity (solid) and temperature (dashed) at 18 and 21 min model times in the control simulation (ΔT=0).

When the simulated cloud reaches the tropopause (at about 21 min MT), it stops moving upwards and an anvil begins to spread (*Fig. 2*). At this time the cloud is in a mature stage, precipitation reaches the ground (*Fig. 2* bottom panel), and the updraft core start to decay (not shown here).

When the simulated cloud reaches the tropopause (at about 24 min MT) it stops moving upwards and an anvil begins to spread (*Fig. 2*). At this time the cloud is in a mature stage and some of precipitation reaches the ground (*Fig. 2* bottom panel).

The first ice particles form between 15 and 18 min MT at 5.5 km AGL (see *Fig. 2*), where the in-cloud temperature is about –12°C. Afterwards, the mixing ratio of all ice species increases (*Fig. 2* and *Fig. 4*). Around 21 and 27 min MT, the maximum values of mixing ratio of hail and graupel, respectively, are reached (*Fig. 4*, *Table 2a*). At 27 min the updraft starts to weaken and part of graupel and hail particles fall down, melt, and transform to rain drops. As a result, graupel and hail mixing ratios in the simulated cloud A (*Fig. 4*) decrease. After 33 min MT the cloud–starts to dissipate. The precipitation intensity simulated by the model with reference sounding maximum (in space and time) is 66.18 mm/hr, and the maximum accumulated precipitation (in space) is 10.25 l/m^2. The total rainfall volume yield (total volume of liquid water fallen on the ground) is 1.98×10^6 m^3.

4.1.2. Effect of warming – comparison between simulations with modified soundings and the control run.

As it can be seen from *Fig. 1*, the increase in atmospheric temperature as a result of the projected regional climate change is expected to be the largest at 300 hPa. Below 4 km ASL (~650 hPa), in warmer environment, the lapse rate is slightly lower, and convection will be suppressed, while above 9 km (300 hPa) there is an increase of the lapse rate and stability decreases. Due to the assumption that the relative humidity is not changed, specific humidity increases where temperature increases. Increased humidity means increased reservoir of water and the associated latent energy, so there is a potential for intensification of cloud dynamics. Intensive storms (with strong updraft) usually reach the 300 hPa level which in our simulation is at 8900 m AGL.

Another important consequence of warming is the upward displacement of the zero isotherm (from 3.6 km in ΔT=0, to 4.1 km in ΔT=3 and 4.6 km in ΔT=5), which affects the formation and development of ice particles in the simulated clouds. Additionally, the cloud base in ΔT=3 is at 17.5 °C, while in ΔT=5 it is at 19.7 °C, or respectively, it is about 3.3 and 5.5 °C warmer than the control cloud base. Together with the zero isotherm upward displacement, the increase of the cloud base temperature due to the warming (and the keeping of the relative humidity unchanged) leads to an extension of the region with temperature higher than 0°C in the simulated 'warming' clouds in ΔT=3 and ΔT=5.

Table 2a. Maximum (in space and time) values for cloud, rain, pristine, snow, aggregates, graupel, hail mixing ratio [g/kg] for simulated "big" cloud

	Cloud	Rain	Pristine	Snow	Aggregate	Graupel	Hail
ΔT=0	6.39	4.09	0.59	0.67	1.14	2.5	7.14
ΔT=3	6.55	4.81	1.04	0.64	1.15	2.4	9.35
ΔT=5	6.78	7.93	1.42	0.69	1.37	2.23	11.04

Table 2b. Integrated (space and time) values for cloud; rain, pristine, snow, and aggregates; graupel and hail mixing ratios [g/kg] for simulated "big" cloud

	Cloud	Rain	Pristine+Snow+Aggregates	Graupel+Hail
ΔT=0	5758	9933	12766	33497
ΔT=3	6062	12696	17041	32558
ΔT=5	6163	14999	18335	28668

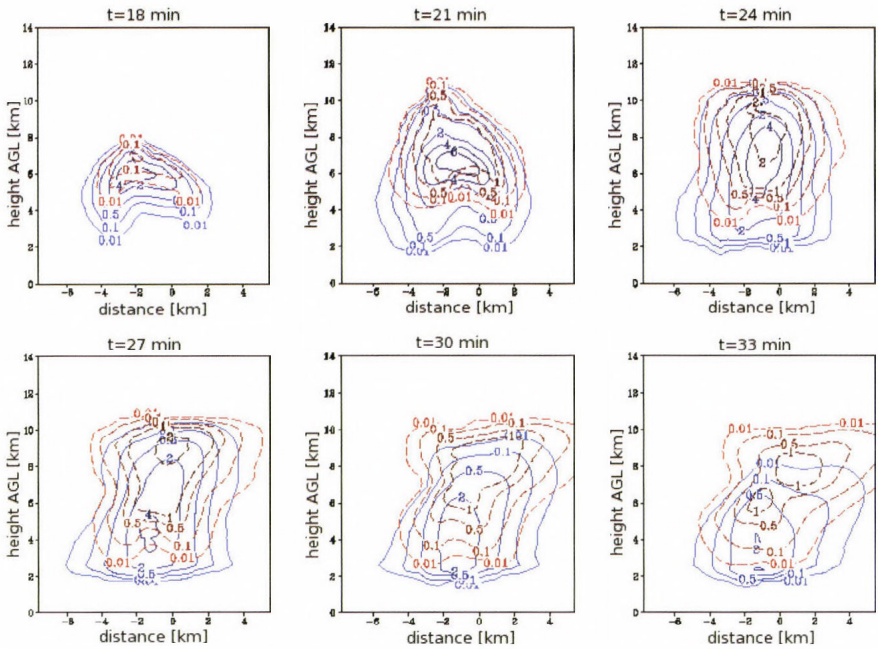

Fig .4. Cloud A: hail (solid) and graupel (dashed) mixing ratios from 18 to 33 min model time in the control simulation (ΔT=0).

The results presented in *Table 2a* show that maximum values of cloud water and aggregates mixing ratio only slightly increase with warming, while there is a significant increase in maximum values of pristine ice, rain, and hail mixing ratios. The warming leads to the increase of space and time integrated mixing ratio of liquid hydrometeors and of small ice particles and to the decrease of the sum of graupel and hail mixing ratio (*Table 2b*). An idea for changes of the evolution of space integrated mixing ratios as a result of warming gives *Figs. 5a – 5d.* The effect of warming on space integrated cloud water mixing ratio is not well pronounced (*Fig. 5a*), while a significant increase of space integrated rain water mixing ratio until 30 min MT is visible in *Fig. 5b* for warmer cases. After 22 min MT, the sum of space integrated ice, snow and aggregates mixing ratios also increases with warming (*Fig. 5c*). The decrease in sum of space integrated graupel and hail mixing ratios (*Fig. 5d*) can be explained by melting of graupel and hail in the warmer environment, which contributes to the increase of rain water mixing ratio.

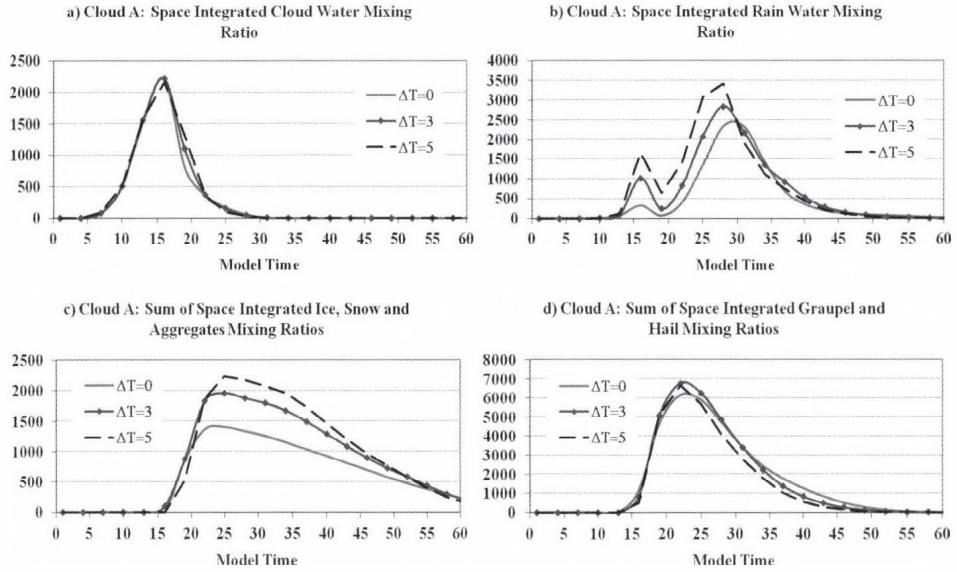

Fig. 5. Cloud A: temporal evolution of a) space integrated cloud water; b) space integrated rain water; c) sum of space integrated ice, snow and aggregates; d) sum of space integrated graupel and hail mixing ratios in g/kg as a function of model time MT in min for ΔT=0, 3, 5.

The top of the control cloud reaches 300 hPa (8.9 km AGL) at 18 min MT. After 18 min MT, the updraft velocity and the processes of formation and

growth of ice particles are intensified and the cloud top rises fast, due to the homogeneous freezing that occurs between –30 °C and –50 °C in the model. The analyses reveal that the clouds simulated with ΔT=3 and ΔT=5 experience similar stages of development to the control cloud (ΔT=0). There are only slight differences in cloud top height (*Fig. 6*) and location and intensity of updraft core (*Fig. 7*). From *Fig. 7* one can see that at 18 min MT, the updraft velocities are almost identical in ΔT=0, ΔT=3, and ΔT=5.

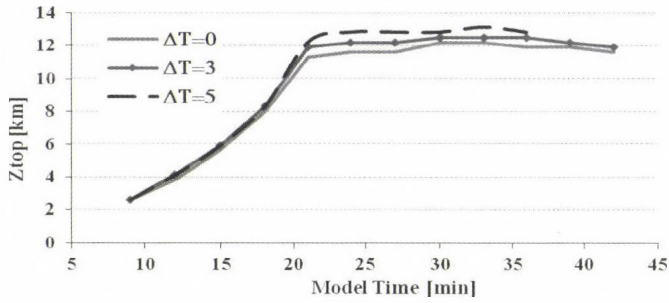

Fig. 6. Cloud A: cloud top height as a function of time for ΔT=0, 3, 5.

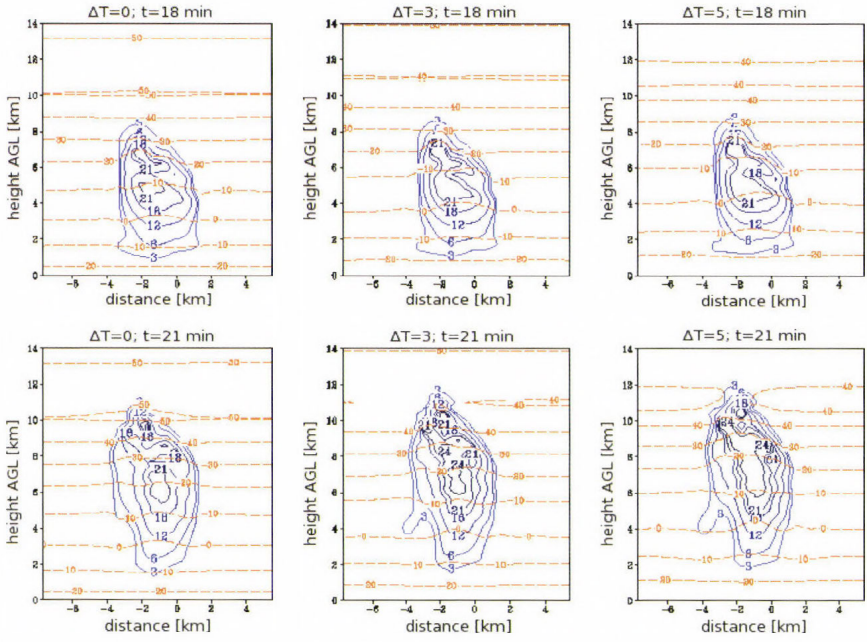

Fig. 7. Cloud A: updraft velocity (solid) and temperature (dashed) at 18 min MT (top panel) and 21 min MT (bottom panel) for ΔT=0, 3, 5 (left, middle, and right panel, respectively).

In the warmer environment, the updraft velocity in the lower parts of simulated clouds has slightly lower values due to slightly lower lapse rates at heights below 4 km. Later, above 4 km, the updraft velocity in the warming cases is larger due to the released latent heat from the frozen water during the formation of hail particles. The top panel of *Fig. 9* shows that the hail mixing ratio increases with warming. Ice crystal particles (*Fig. 8a*, top panel) form a few minutes earlier in the control run than in the clouds, simulated with ΔT=3 and ΔT=5. The reason for the earlier formation of ice particles at lower altitude in ΔT=0 is the lower temperature in the original sounding. At 21 min MT, all three clouds have passed the –40 °C isotherm which is at higher altitudes (9.3, 9.9, and 10.3 km AGL, respectively for the control run, ΔT=3, and ΔT=5) in warming cases. The updraft velocity in the latter case is highest, showing very intensive growth (*Fig. 7*). This corresponds to the thermodynamic effect of the increased lapse rate above 9 km AGL in warming cases. Another reason for the increase of the updraft velocity in the "big" cloud developed in the warmer environment is the higher water mixing ratio at higher levels in these cases (*Fig. 8a*, top panel). Liquid water, once frozen, leads to the increase of the ice mixing ratio (*Fig. 8a* , bottom panel) above –30 °C and the release of more latent heat. A strong maximum of 33 m/s is seen (*Fig. 7*) in ΔT=5 case (compared to 24 m/s in the control cloud and 30 m/s in ΔT=3).

From *Figs. 8* and *9* it is visible that the higher liquid water and higher ice mixing ratio (*Fig. 8a*) in the warmer environment lead to higher hail mixing ratio (*Fig. 9a*, top panel). At 24 min MT, the hail mixing ratio in the layer between 5 and 10 km is almost double in ΔT=5 compared to ΔT=0. The analyses show that in cases ΔT=3 and ΔT=5, the hail particles have larger liquid fraction, higher density, and larger fall velocity, so they fall earlier to lower levels in comparison with ΔT=0. Precipitation for all three simulations begins at about 21 min MT and stops at 50 min MT (*Fig. 10*). Melted hail particles contribute to the earlier occurrence of the maximum precipitation rate in the warming cases – 30 min MT in ΔT=5, compared to 33 min in ΔT=0. Precipitation rate, accumulated precipitation, and total rainfall volume increase in the warm simulations (*Table 3*). The peak precipitation rate in ΔT=5 is almost twice as high as in ΔT= 0.

Table 3. Peaks of rainfall rate, accumulated (for 50 min MT) rainfall, and accumulated total rainfall volume yield from cloud A ("big" cloud)

	Peak precipitation rate [mm/h]	**Peak accumulated precipitation [l/m^2]**	**Total rainfall volume [m^3]**
ΔT=0	66.18	10.25	1.98 10^6
ΔT=3	71.71	11.40	2.23 10^8
ΔT=5	112.24	12.75	2.42 10^8

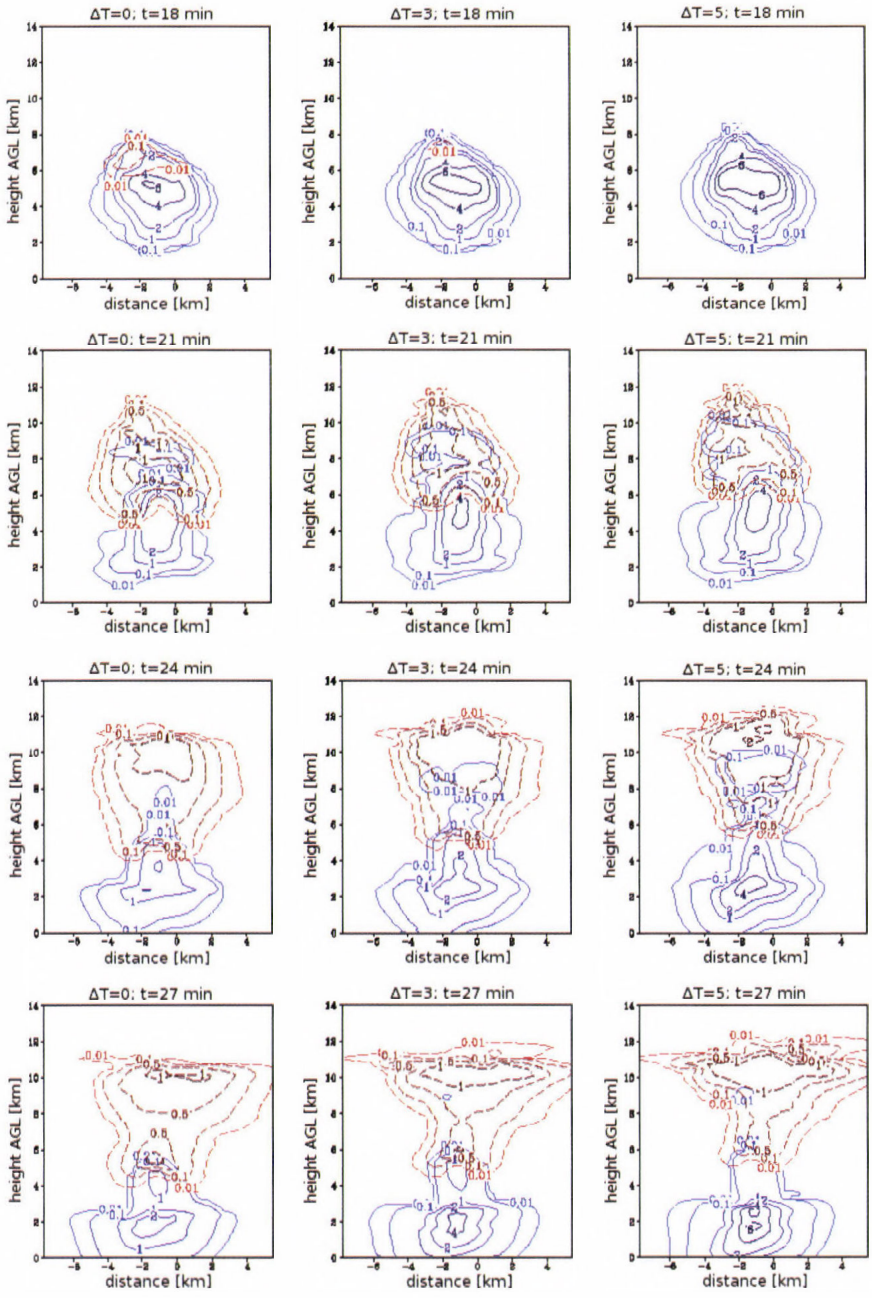

Fig. 8. Cloud A: sum of rain and cloud water mixing ratios (solid) and sum of pristine ice, snow, and aggregates mixing ratios (dashed) at 18 min MT, 21 min MT, 24 min MT, and 27 min MT (from top to bottom panel) for ΔT=0, 3, 5 (left, middle, and right panel, respectively).

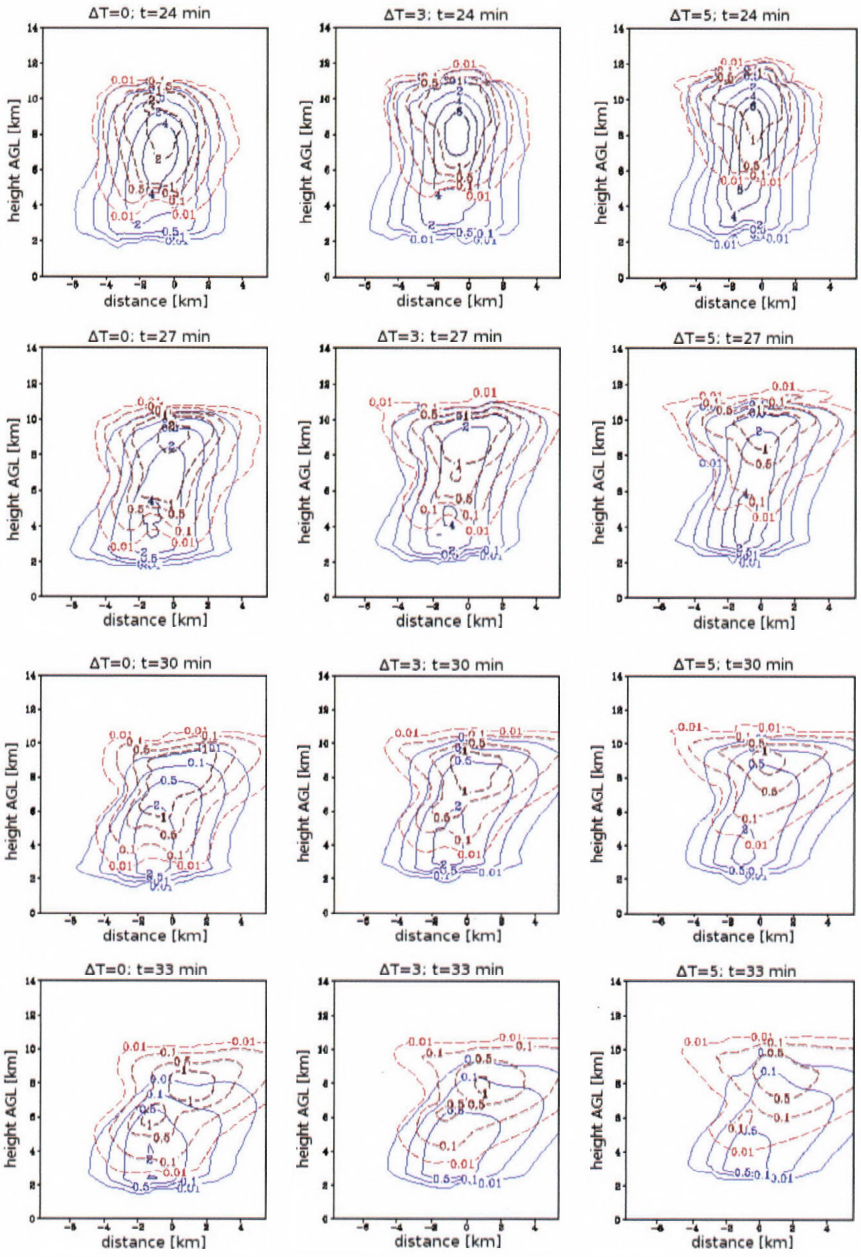

Fig. 9. Cloud A: hail (solid) and graupel (dashed) mixing ratios at 24 min MT, 27 min MT, 30 min MT, and 33 min MT (from top to bottom panel) for ΔT=0, 3, 5 (left, middle, and right panel, respectively).

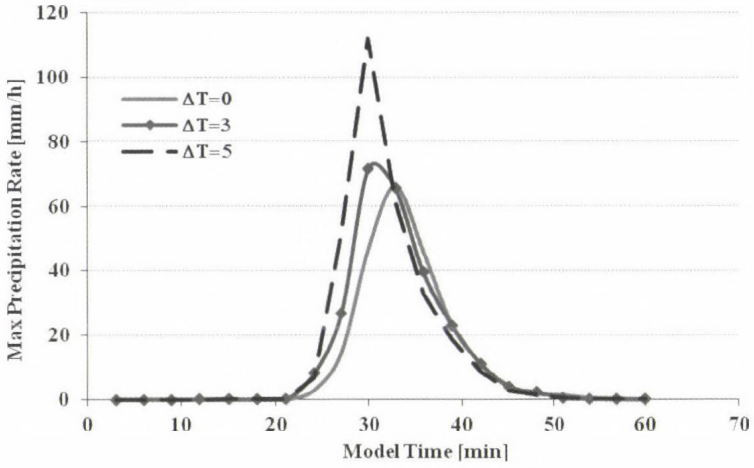

Fig. 10. Cloud A: peak rainfall rate as a function of time for ΔT=0, 3, 5.

4.2. Cloud B

Cloud B is the 'small' cumulonimbus that develops in the same environment as cloud A, but it is initiated with a smaller thermal bubble (see *Table 1*).

4.2.1. Macro- and microphysical evolution of the control cloud

Similarly to cloud A, cloud development begins at 9 min MT, and the cloud base height is at 1726 m AGL (14.16 °C). During the next 15 min, the cloud top rises at a rate of 10 m/s until 24 min MT and at 27 min MT it reaches its maximum height of 9.5 km AGL, where the temperature in the environment is –41 °C (*Figs. 12*, and *15*). The maximum updraft velocity (18 m/s) is reached at ~5 km AGL at 24 min MT (*Fig. 12*). After 24 min MT, the updraft velocity starts to decrease and after 30 min MT, the downdrafts prevail. Then the simulated cloud B begins to dissipate, and precipitation falls on the ground.

Ice formation (*Fig. 11*) starts after 18 min MT at an altitude above 4 km (about –5 °C). The formation of hail and graupel starts at the same time and altitude (*Fig. 13*). Maximum mixing ratios of hail and graupel are reached at 21 and 24 min MT, respectively (*Fig. 13* and *Table 4a*).

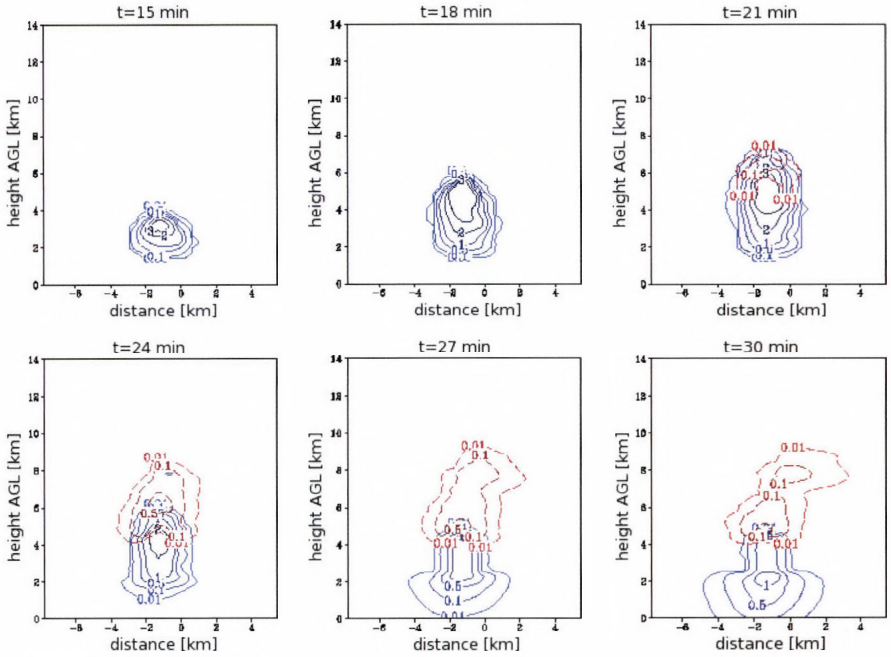

Fig. 11. Cloud B: sum of rain and cloud water mixing ratios (solid) and sum of pristine ice, snow, and aggregates mixing ratios (dashed) in the control simulation (ΔT=0).

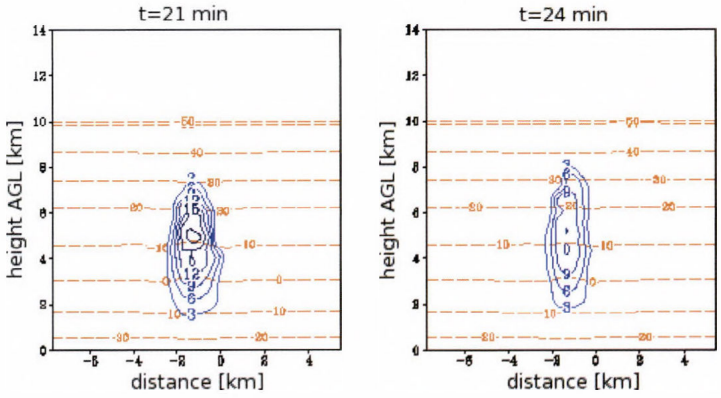

Fig. 12. Cloud B: updraft velocity (solid) and temperature (dashed) at 21 and 24 min model times in the control simulation (ΔT=0).

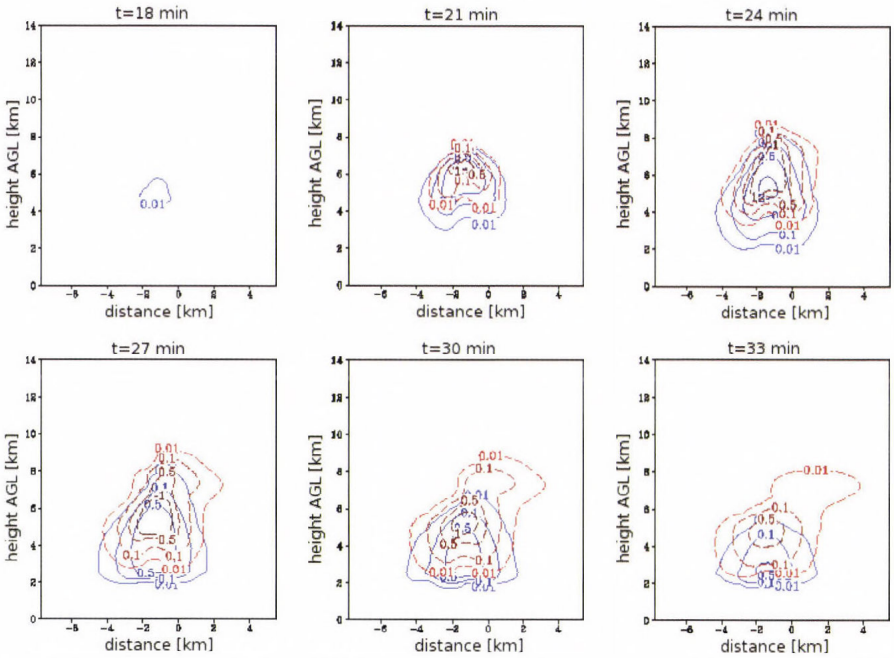

Fig. 13. Cloud B: hail (solid) and graupel (dashed) mixing ratios from 18 to 33 min model times in the control simulation (ΔT=0).

Table 4a. Maximum (in space and time) values for cloud, rain, pristine, snow, aggregates, graupel, hail mixing ratio [g/kg] for cloud B formed in different environmental conditions

	Cloud	**Rain**	**Pristine**	**Snow**	**Aggregate**	**Graupel**	**Hail**
ΔT=0	5.37	1.51	0.14	0.4	0.71	2.32	2.81
ΔT=3	5.43	1.47	0.08	0.51	0.55	1.62	3.58
ΔT=5	5.26	1.81	0.1	0.37	0.76	1.17	3.38

Table 4b. Integrated (space and time) values for cloud and rain water; pristine, snow and aggregates; graupel and hail mixing ratios [g/kg] for cloud B formed in different environmental conditions

	Cloud	**Rain**	**Pristine+Snow+Aggregates**	**Graupel+Hail**
ΔT=0	1743	1544	549.39	3895.28
ΔT=3	1542	1387	272.97	1810.96
ΔT=5	1372	1223	107.08	954.11

The lifecycle of this cloud is different from that of cloud A. There is less vigorous convection and less condensation takes place, so the cloud grows smaller and the mixing ratios of all hydrometeors are lower. Their size (not shown here) and fall velocity are also lower.

The simulated maximum (*Table 5*) precipitation intensity of space and time is 16.77 mm/hr and the peak accumulated precipitation is 2.25 l/m^2. The total rainfall volume yield is $0.253 \cdot 10^6$ m^3, which is ten times less than the rainfall volume yield in cloud A.

Table 5. Peaks of rainfall rate, accumulated (for 50 min MT) rainfall and accumulated total rainfall volume yield for Cloud B ("small" cloud)

	Peak precipitation rate [mm/h]	**Peak accumulated precipitation [l/m^2]**	**Total rainfall volume [m^3]**
ΔT=0	16.77	2.25	$0.25\ 10^6$
ΔT=3	15.01	1.65	$0.19\ 10^6$
ΔT=5	12.85	1.24	$0.14\ 10^6$

4.2.2. Effect of warming – comparison between the modified simulations and the control run.

From *Fig. 14* it can be seen, that cloud top heights of simulated "small" clouds in warmer environment are a few hundred meters lower than the cloud top height of control cloud B, although the maximum heights are reached at the same time, 27 min MT. However, the analyses reveals that the control run reaches temperatures around –42 °C, while the warming cases ΔT=3 and ΔT=5 reach –37 °C and –30 °C, respectively.

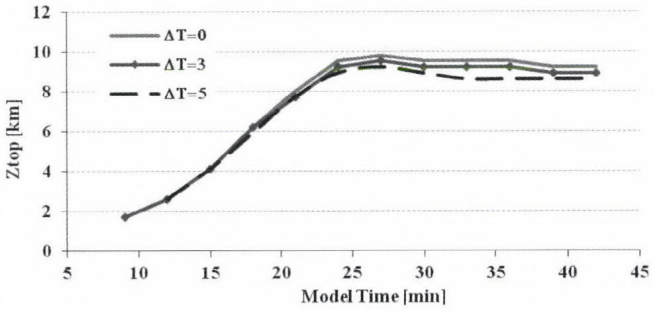

Fig. 14. Cloud B: cloud top height for cloud B as a function of time for ΔT=0, 3, 5.

Results presented in *Table 4a* show that there is no well defined tendency in the changes of maximum values of mixing ratios of the hydrometeors as a result of warming, while the integrated (in space and time) mixing ratios of solid hydrometeors are significantly lower (see column 3 and 4 of *Table 4b*) at higher environmental temperatures. The warming also leads to the decrease of both cloud (column 1 in *Table 4b*) and rain (column 2 in *Table 4b*) mixing ratios integrated in space and time. The evolution of space integrated mixing ratios (*Fig. 15*) reveals that the space integrated rain water mixing ratio in the clouds simulated with warmer environment is higher until 27 min MT, and after that it is lower in comparison to the space integrated rain water mixing ratio in the control cloud.

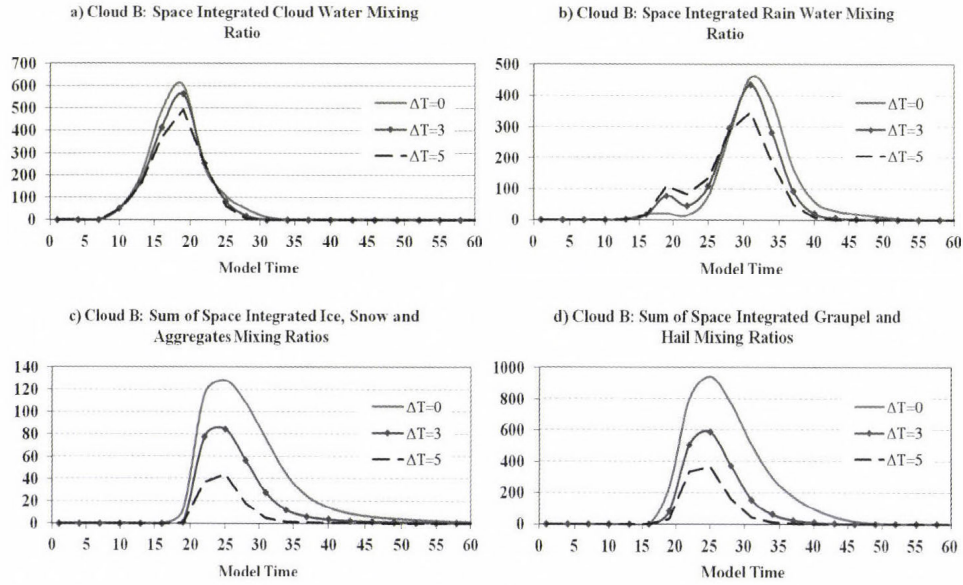

Fig. 15. Cloud B: temporal evolution of a) space integrated cloud water; b) space integrated rain water; c) sum of space integrated ice, snow, and aggregates; d) sum of space integrated graupel and hail mixing ratios in g/kg as a function of model time MT (in min) for ΔT=0, 3, 5.

Plots of the vertical velocity for 21 and 24 min MT (*Fig. 16*) show that the values of the maximum vertical velocity are almost the same, however, it is slightly decreasing and located at lower altitudes with the warming. In the three simulated clouds there is almost no difference in updraft velocities below 5 km, while above 5 km in the warming cases the updraft velocity is lower. In the upper parts of clouds in ΔT=3 and ΔT=5, compared to the control one, there is a smaller amount of freezing water due to the higher temperature. Furthermore,

the clouds denoted with ΔT=3 and ΔT=5 do not reach the level of ~40 °C where intensive homogeneous freezing occurs. Since freezing provides latent heat to accelerate the updraft, this leads to lower values of updraft velocity, despite the decreased stability.

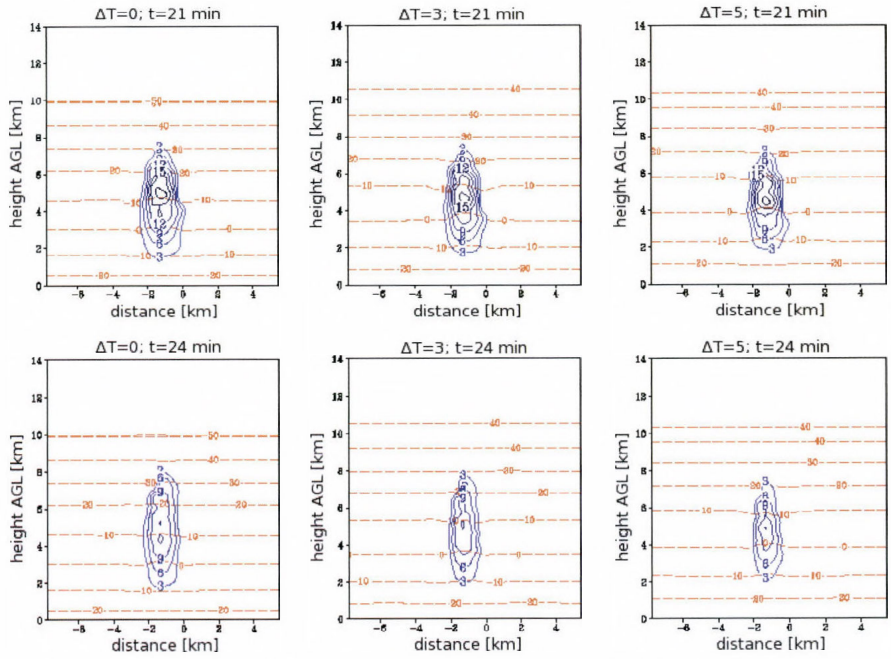

Fig. 16. Cloud B: updraft velocity (solid) and temperature (dashed) at 21 and 24 min model times for ΔT =0, 3, 5.

The analysis of mixing ratio of hydrometeors in vertical cross section at different moments of time (*Figs. 17* and *18*) shows that in clouds developed in a warmer environment the total liquid water mixing ratio is slightly higher than in the simulated ΔT=0 cloud, while due to higher temperatures, the values of ice (the sum of pristine, snow, and aggregates) and graupel mixing ratio (*Fig. 18*) are lower compared to the control cloud. There is higher rain water mixing ratio in warming cases (*Fig. 17*). The more detailed analysis shows, that in ΔT=0 at 21 min MT, ice starts to form at 5–7 km by freezing of cloud and rain drops, while in ΔT=5 there is still no ice. Coagulation of drops with graupel and hail in ΔT=0 further contributes to the decrease of the liquid water mixing ratio at these altitudes. On the other hand, in ΔT=5 the mixing ratios of cloud and rain water

continue to increase. After the formation of ice in ΔT=5 (see bottom panel of *Fig. 17*), the rain mixing ratio also starts to decrease. Hail mixing ratio increases in ΔT=3 compared to ΔT=0 and decreases in ΔT=5 compared to ΔT=3. The increase in hail mixing ratio in ΔT=3 and ΔT=5 is accompanied by an increase of hail liquid fraction (not shown here). The reason for that can be found in the definition of hail as a higher density hydrometeor than graupel that can carry a larger fraction of liquid water. The sources for hail particles are coalescence between solid and liquid particles (when water freezes slowly) or partial melting of graupel, and the sinks are shedding and melting into rain. In warming cases, due to the increased temperature, water droplets colliding with an ice particle freeze slower, thus increasing the ice particle density and leading to the formation of hail rather than graupel. This could be a reasonable explanation for the fact that the hail mixing ratio increases in ΔT=3. Obviously, in warming cases more hail particles grow in wet regime. In ΔT=5 hail, particles carry a larger fraction of liquid, have higher density and consequently a higher fall velocity, so more hail particles fall to levels having positive temperature and melt to form rain. This can be the reason for the decrease of maximum hail mixing ratio in ΔT=5 compared to ΔT=3. These speculations are supported by the results presented in *Fig. 17*, where plots of the sum of cloud and rain and the sum of pristine, snow, and aggregates are shown, and in *Fig. 18*, where graupel and hail mixing ratios are shown. From *Fig. 17* it is evident that ice starts to form later in warming cases compared to the control run. At 27 min MT, the difference in microphysical development can be seen – the control cloud still has lots of ice in its upper part, a slightly lowered liquid water mixing ratio and some graupel and hail close to cloud base (*Fig. 18*), while ΔT=5 has lost much of its ice mixing ratio above 5 km and has more hail close to cloud base, compared to ΔT=0 and ΔT=3. The melting of ice is visible in *Fig. 18* where hail mixing ratios for 24 min MT are high in all three clouds, but later it decreases faster in warming cases, and there is almost no ice in ΔT=5 at 33 min. From the same figure it can be seen that during the mature stage (27–33 min), the hail mixing ratio close to cloud base slightly decreases in the warm simulations, while graupel mixing ratio decreases significantly.

These differences in the clouds' microphysical evolution lead to differences in precipitation. In ΔT=5 at 24 min, large amount of liquid water is "found" in the layer between 4–6 km, consisting mostly of raindrops, and it decreases sharply at 27 min (*Fig. 17*). At 33 min MT, there is a low amount of graupel and hail in ΔT=5 compared to ΔT=0, while the liquid mixing ratio in the clouds (not shown here) has similar values. Precipitation starts at the same MT for the three clouds (*Fig. 19*), but it is less intensive in warming cases. Despite the increased reservoir of water vapor in the warmer atmosphere, the precipitation (intensity and total volume) is lower than the precipitation from the control cloud (see *Table 5*, *Fig. 19*) The peak in the ΔT=5 case is earlier than ΔT=0. The decrease in total rainfall volume is 25% for "ΔT=3" and another 25% for ΔT=5 compared to ΔT=3.

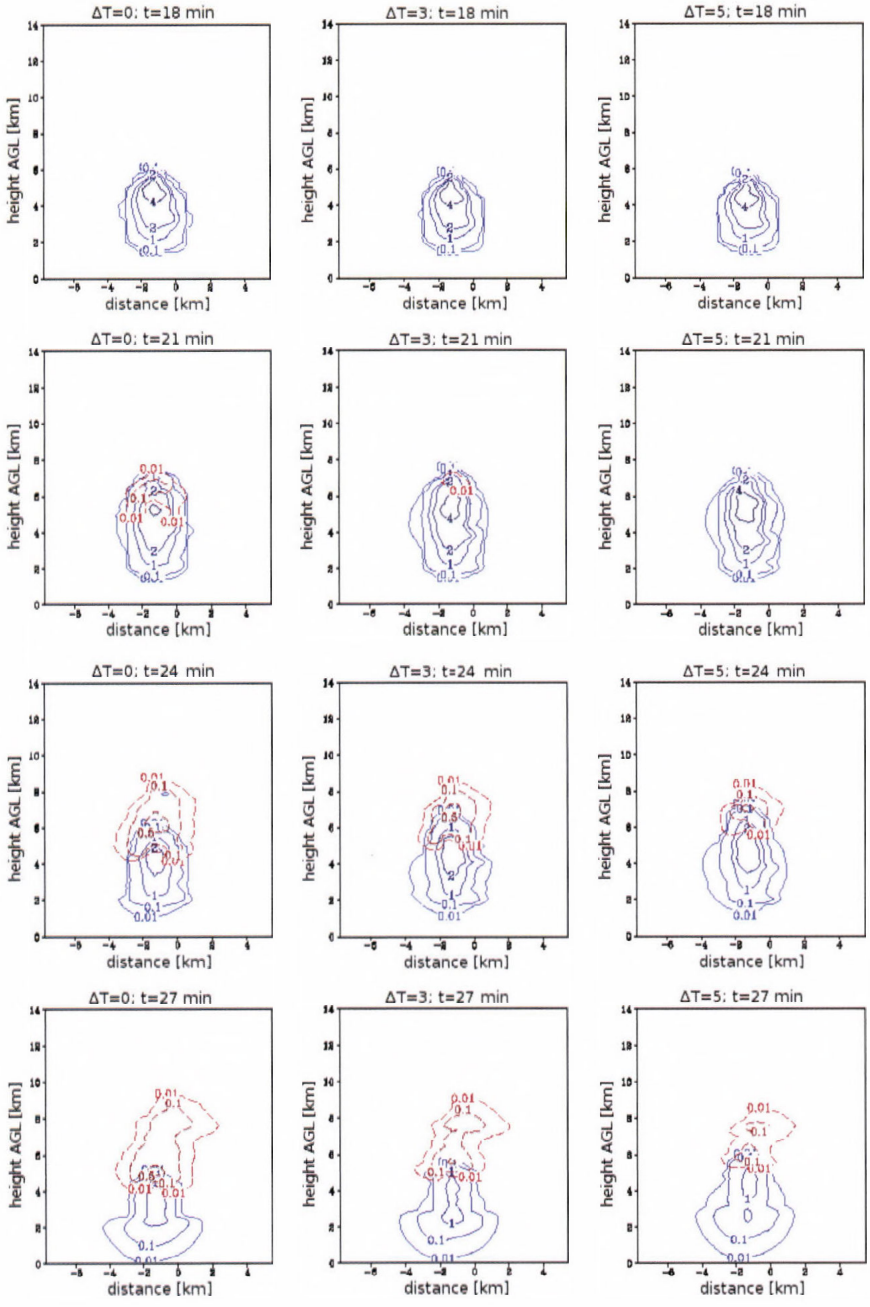

Fig. 17. Cloud B: sum of rain and cloud water mixing ratios (solid) and sum of pristine ice, snow, and aggregates mixing ratios (dashed) at 18 min MT, 21 min MT, 24 min MT, and 27 min MT (from top to bottom panel) for ΔT=0, 3, 5 (left, middle, and right panel, respectively).

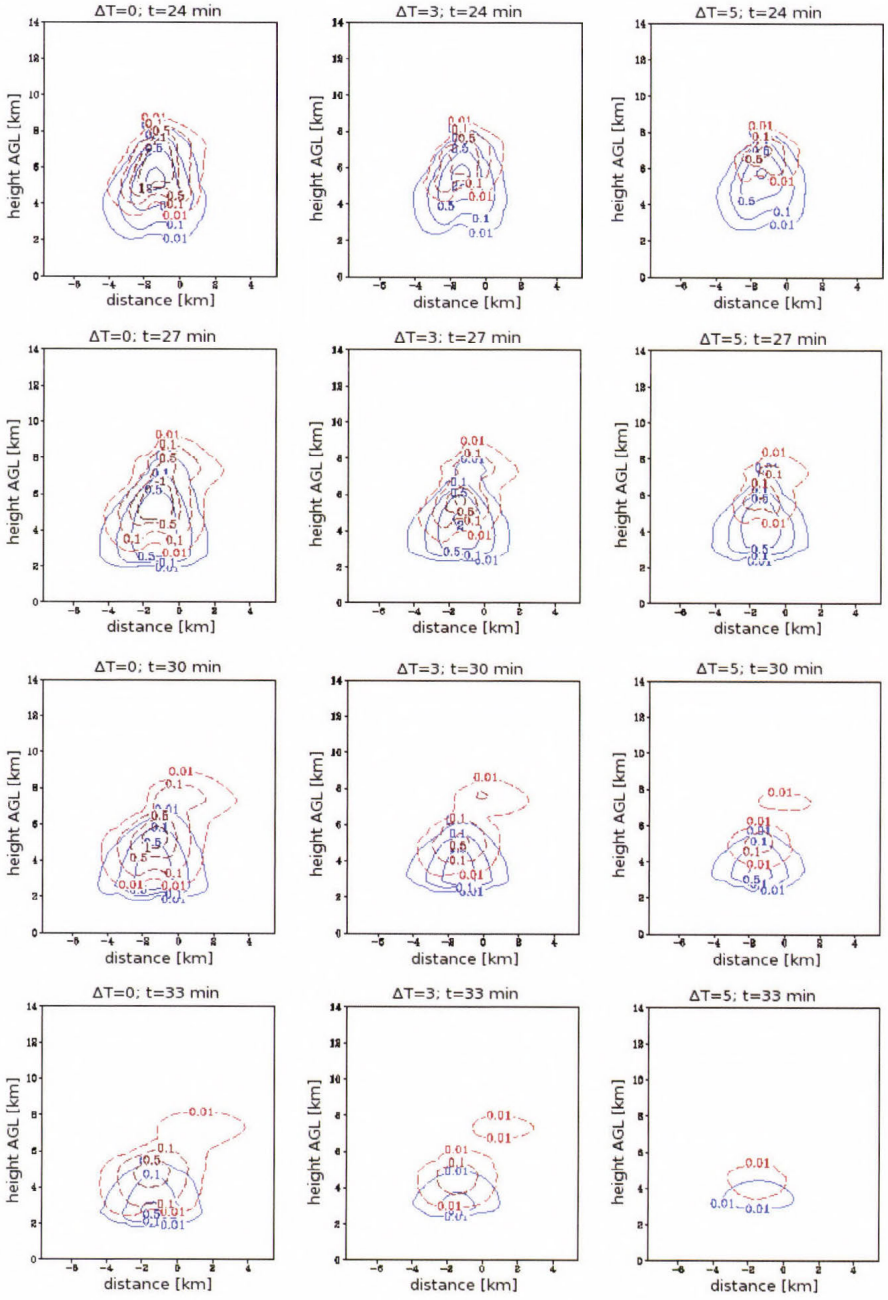

Fig. 18. Cloud B: hail (solid) and graupel (dashed) mixing ratios at 24 min MT, 27 min MT, 30 min MT, and 33 min MT (from top to bottom panel) for ΔT=0, 3, 5 (left, middle, and right panel, respectively).

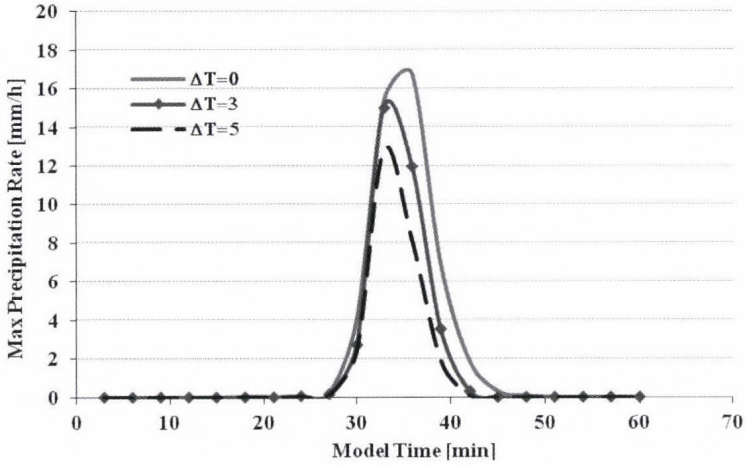

Fig. 19. Cloud B: peak rainfall rate as a function of time for ΔT=0, 3, 5.

5. Conclusions

In the present study, the impact of projected changes of the temperature and humidity profiles in the mid-latitude troposphere (IPCC, 2007) on the development and precipitation from summertime convective clouds is investigated. One typical sounding from Sofia is selected, and two scenarios of projected changes, according to IPCC, 2007, are imposed on this sounding. Two clouds with different dynamics are simulated, identified here as a 'big' one and a 'small' one.

The results can be summarized in the following way for the clouds developed in a warming environment – in comparison with the "control" clouds. For both clouds ('big' and 'small'):

- Sum of space and time integrated mixing ratios of graupel and hail decreases.
- Precipitation intensity has a more rapid increase in the beginning and its maximum occurs earlier.

Big cloud (A):

- Liquid water mixing ratio increases.
- Small ice particles (pristine, snow, and aggregates) mixing ratios increase.
- The updrafts are more intensive.

- Accumulated precipitation and total rainfall volume are higher.

Small cloud (B):

- Liquid water mixing ratio decreases.
- Small ice particles (pristine, snow, and aggregates) mixing ratios decrease.
- The updrafts are more intensive in lower levels and suppressed at higher levels of the cloud.
- Accumulated precipitation and total rainfall volume are significantly lower.

Results show that there are two sides of the expected pattern of change in the thermodynamic structure of the troposphere – it leads to the suppression of cloud dynamics and reduction of precipitation in the "small" cloud and to the intensification of the updraft and increase of precipitation in the "big" cloud. Our study analyzes the reasons for the contrary impact of climate warming depending on cloud intensity. For both types of cloud ("big" and "small"), the projected warming leads to higher values of liquid mixing ratio in low cloud layers and a delay in freezing, which takes place higher in the cloud. The study demonstrates that when the forcing conditions are strong enough ("big" cloud) for the cloud to reach levels with low temperatures, especially where homogeneous freezing occurs, more latent heat is released due to the freezing of a larger quantity of liquid water in warmer cases. This leads to higher content of ice particles and cloud intensification – increase of cloud updraft and cloud top. The quantity of ice precipitation particles increases and adds to the amount of liquid precipitation after melting. In these cases, the projected warming amplifies precipitation rate, accumulated precipitation, and total rainfall volume. In the cases with weaker forcing conditions ("small" cloud), when the cloud does not have enough energy to rise to higher levels (especially the level of homogeneous freezing), in a warming environment, less liquid water freezes, leading to the occurrence of a smaller quantity of ice precipitation particles inside the cloud, which in turns leads to the decrease of contribution of ice particles to the liquid precipitation. Thus, the decrease of precipitation rate, accumulated precipitation, and total rainfall volume in the "small" clouds at the increase of environmental temperature can be explained by the decrease of mixing ratios of liquid and solid precipitating particles at ΔT =3 and ΔT =5 in comparison with ΔT =0.

Results indicate the importance of the ice phase evolution in the formation of precipitation in continental mid-latitude convective clouds. Within the limitations of the model used in this study, one can conclude that in a warming environment intensive storms will have enhanced power, so they will create greater damage. On the other hand, warming can also lead to droughts by

suppressing the development of smaller cumuli. Since the present work is based on only one case study, we have to stress that different conclusions might emanate from further modeling runs encompassing wide ranges of meteorological conditions and combinations of other climate change factors. The thermodynamic forcing, investigated in the present paper, acts in the same direction as the forcing created from increasing aerosol concentrations, as explained by the conceptual model of *Rosenfeld et al.* (2008), so it is a challenging question how convective clouds and precipitation will change when those two factors work together.

It is also worth mentioning that the scenario tested in the present study is based on the concept of constant relative humidity. If the moisture above the continents is not enough and the relative humidity decreases, probably the effect of the thermodynamic changes in the environment air on convective clouds microphysics, dynamics, and precipitation would be reduced.

Furthermore, since the evaporation from the surface and the interactions between adjacent clouds are also important, real cases with larger domains and more than one cloud or even whole mesoscale systems should be simulated, in order to investigate the potential impact of climate warming on mid-latitude convective precipitation.

Acknowledgements —The present work is partially supported by EC through FP6 project ACCENT (GOCE-CT-2002-500337), the NATO SfP – ESP.EAP.SFPP 981393, and the Science Foundation of Sofia University (grant 153/2009).

References

Allen, M.R. and *Ingram, W.J.*, 2002: Constraints on future changes in climate and the hydrologic cycle. *Nature 419*, 224–232.

Cotton, W., Pielke Sr, R., Walko, R., Liston, G,. Trembecack, C., Jiang, H., McAnelly, R., Harrington, J., Nicholls, M., Carrio, G., McFadden, J., 2003: 'RAMS 2001: Current status and future directions', *Meteorol. Atmos. Phys. 82*, 5–29.

Demott, P.J., Meyers, M.P., and *Cotton, W.R.*, 1994: Parameterization and impact of ice initiation processes relevant to numerical model simulation of cirrus clouds. *J. Atmos. Sci. 51*, 77–90.

Elliot, W.P. and *Angell, J.K.*, 1997: Variations of cloudness, precipitable water, and relative humidity over the United States;1973-1993, *Geophys. Res. Lett.*, *24*, 41–44.

IPCC, 2007: Climate Change 2007: Report of the Intergovernmental Panel on Climate Change, *Cambridge University Press*, 921.

Kharin, V.V. and *Zwiers, F.W.*, 2005: Estimating extremes in transient climate change simulations. *J. Clim. 18*, 1156–1173.

McCaul Jr., E.W., Cohen, C., Kirkpatric, C., 2005: The sensitivity of simulated storm structure, intensity and precipitation efficiency to environmental temperature, *Mon. Weather Re.133*, 3015–3037.

Meyers, M., Walko, R., Harrington, J.,and *Cotton, W.*,1997: New RAMS cloud microphysics parametrization. Part II: The two-moment scheme. *Atmos. Res. 45*, 3–39.

Meehl, G.A., Washington, W. M, Santer, B.D., Collins, W.D., Arblaster, J.M., Hu, A., Lawrence, D.M., Teng, H., Buja, L.E., and Strand, W.G., 2006: Climate Change Projections for the Twenty-First Century and Climate Change Commitment in the CCSM3. *J. Climate 19*, 2597–2616.

Mitzeva, R., Tsenova, B., Todorova, A., and *Latham, J.*,2008: Comparative modeling study of the impact of aerosols and climate changes on microphysics and dynamics of mixed-phase convective clouds. *15th International Conference of Clouds and Precipitation, Cancun-Mexico*, July 7–13, 2008.

Philips, V.T.J., Donner, L.J., and *Garner S.T.*, 2007: Nucleation processes in deep convection simulated by a cloud-system resolving model with double moment bulk microphysics. *J. Atmos. Sci. 64*, 738–761.

Pielke, R.A., Cotton, W., Walko, R., Tremback, C.J., Lyons, W.A., Grasso, L.D., Nicholls, M.E., 1992: A Comprehensive Meteorological Modeling System RAMS. *Meteorol. Atmos. Phys. 49*, 69–91.

Rosenfeld, D., Lohman, U., Raga, O'Dowd, G., Kulmala, M., Fussi, S., Reissell, A., and *Andreae, M*, 2008: Flood or drought: How do aerosols affect precipitation, *Science*, *321*, 1309–1313.

Santer, B.D, Sausen, R., Wigley, T M.L., Boyle, J S., Rao, A., Doutriaux, K., Hansen, C., Meehl, J.E., Roeckner, G.A., Ruedy, E., Schmidt, R., G., and *Taylor, K.E.*, 2003: Behaviour of tropopause height and atmospheric temperature in models, reanalyses and observations. Decadal changes, *J. Geophys. Res. 108*, D1, 4001.

Semenov, V.A. and *Bengtsson, L.*, 2002: Secular trends in daily precipitation characteristics: greenhouse gas simulation with a coupled AOGCM. *Clim. Dyn. 19*, 123–140.

Takemi T., 2010: Dependence of the precipitation intensity in mesoscale convective systems to temperature lapse rate. *Atmos. Res. 96*, 273–285.

Trenberth K, Dai, A., Rasmussen, R., and *Parsons, D.*, 2003: The changing character of precipitation. *B.Am.Meteorol.Soc. 84*, 1205–1217.

Van den Heever, S.C., Carrio, G.G., Cotton, W.R., Demott, P.J., and *Prenni, A.J.*, 2006: Impacts of nucleating aerosols on Florida Storms. Part I: Mesoscale simulations. *J. Atmos. Sci.* 63, 1752–1775.

IDŐJÁRÁS

Quarterly Journal of the Hungarian Meteorological Service
Vol. 116, No. 4, October–December 2012, pp. 281–295

Spatial and temporal evolution of drought conditions at various time scales in the Czech Republic during growing period

Vera Potop[1]*, **Constanţa Boroneanţ**[2], **Martin Možný**[3], **Petr Štěpánek**[4], and **Petr Skalák**[4]

[1]*Czech University of Life Sciences Prague, Faculty of Agrobiology, Food and Natural Resources, Department of Agroecology and Biometeorology, Kamycka 129, 165 21 Prague 6 – Suchdol, Czech Republic*

[2]*Center for Climate Change, Geography Department, University Rovira I Virgili, Campus Terres de l'Ebre, Av. Remolins 13-15, 43500 Tortosa, Spain*

[3]*Czech Hydrometeorological Institute, Na Šabatce 2050/17 143 06 Prague 412-Komořany, Czech Republic*

[4]*Global Change Research Centre AS CR, Bědila 986/4a, 603 00 Brno, Czech Republic*

**Corresponding author E-mail: potop@af.czu.cz*

(Manuscript received in final form April 24, 2012)

Abstract—This paper analyzes the characteristics of spatial evolution of the standardized precipitation evapotranspiration index (SPEI) at various time scales during the growing period (April-September) over the Czech Republic. The SPEI was calculated from monthly records of mean temperature and precipitation totals measured at a dense network of 184 climatological stations for the period 1961–2010. Using various lags, 1, 3, 6, 12, and 24 months. The drought at these time scales is relevant for agricultural, hydrological, and socio-economic impacts, respectively. The study refers to the warm season of the year (from April to September). The principal modes of variability of the SPEI calculated at these five time scales were identified by using the empirical orthogonal functions (EOF) analysis. The explained variance of the leading EOF ranges between 71 and 61% as the time scale for calculating the SPEI increases from 1 to 24 months. The explained variance of EOF2 and EOF3 ranges between 5 and 9%, and 4 and 6%, respectively, as the SPEI is calculated for 1–24 months. With a few exceptions at stations at the highest altitudes, the spatial coefficients of the EOF1 for all SPEI time scales have the same sign over the country´s territory. Based on the spatial distribution of

the spatial coefficients of EOF2 and EOF3, at all SPEI time scales we have identified three climatically homogenous regions, corresponding to the altitudes below 400 m, between 401 and 700 m, and above 700 m. This regionalization corresponds to some extend to that which was previously used in other studies. These three regions reflect different land use types corresponding to: (i) mostly intensive agriculture, (ii) less intensive agriculture, and (iii) limited agricultural production and mostly forested, respectively. For these three regions, the frequency distribution of the SPEI values in 7 classes of drought category (%) were calculated based on station records for each region. The normal conditions represent around 65% out of the total values of SPEI for all time scales, in all three regions, while moderate drought and moderate wet conditions are almost equally distributed around 10.5%. As the SPEI time scale increases, the difference between the percentages of extremely dry and extremely wet conditions changes on average from 0.2% (SPEI 1-month) to 4% (SPEI 24-month).

Key-words: standardized precipitation evapotranspiration index, frequency distribution, empirical orthogonal function, Czech Republic.

1. Introduction

Drought indices associated with specific time-scales are useful tools for monitoring and management of drought. For quantifying the drought conditions, *Vicente-Serrano et al.* (2010) have developed a new drought index – the standardized precipitation evapotranspiration index (SPEI) based on precipitation and potential evapotranspiration (PET). The SPEI combines the sensitivity of the Palmer drought severity index (PDSI) to changes in evaporative demand (related to temperature fluctuations and trends) with the multi-temporal nature of the Standardized Precipitation Index (SPI). The various time scales provided by the SPEI can be related to different drought types in a region. Short time scales show a high relationship with variations of soil moisture, which determine water availability for vegetation and agriculture, while water resources in reservoirs are related to longer time scales (*Dai*, 2011; *Vicente-Serrano et al.,* 2011).

In previous studies (*Potop et al.*, 2011, 2012), drought was extensively analyzed by comparing results from the most advanced drought indices (e.g., SPI and SPEI), which take into account the role of antecedent conditions in quantifying drought severity in the lowland regions of the Czech Republic. Decadal trend in the drought extent detected by the SPEI are apparent, however, with higher values of drought incidences in the 1940s, early 1950s, and 1990s, and with fewer drought episodes in the 1910s, 1930s, and 1980s. These episodes coincide with the secular drought evolution recorded in the central part of Europe (*Brázdil et al.*, 2009; *Dai*, 2011). Consequently, SPEI and SPI showed large differences in the evolution drought severity during decades with the lowest summer negative temperature anomalies combined with the lowest precipitation (cold and dry; the first two decades of the 20th century), the highest summer positive temperature anomalies (the end of the 20th century), both high spring positive temperature and precipitation anomalies (warm and

wet; the beginning of the 20th century), and the lowest deficit of water balance (1947, 2003, 1994, 1983, and 1933) (*Potop et al.*, 2012). On the other hand, similarities between two indices were reported during the decades with high fluctuations of positive spring temperature and lower precipitation (warm and dry; 1950s, 1990s, and 2000s); extremely long sunshine durations (155% of the normal amount in extremely dry June of 2006 and August 2003, up to twice the norm for April of 2007 and 2009, in the reference period of 1961–1990); and consecutive dry days. Therefore, the role of temperature was evident in summer drought episodes which depend on the intensity and duration of temperature anomalies, generating a higher water demand by potential evapotranspiration at the end of the last century.

New detailed results on the temporal evolution of the SPEI at various time-scales and the impact of drought on vegetable crops were discussed and presented in broader climatological and European contexts in, e.g., *Potop* and *Možný* (2011a, 2011b), *Potop* and *Soukup* (2011). However, more in-depth analysis is required to explore the vulnerability to drought in the context of climate change based on a denser station network to better representation of various climate conditions across the Czech Republic (*Potop et al.* 2012a; *Potop et al.* 2012b).

The present study aims at the analysis of the spatial evolution of the SPEI at various time scales during the warm period (April-September) over the Czech Republic. To this aim, the principal modes of variability of SPEI are examined based on data from a dense network of climatological stations in the Czech Republic during the period of 1961–2010 in order to reveal the regional characteristics of drought variability. Frequency distribution of SPEI values over the three regions in 7 classes of drought category (%) at time scales of 1, 3, 6, 12, and 24 months, and the spectral analysis of the series of the SPEI ≤ -1 were also analyzed.

2. Data and methods

The SPEI was calculated from monthly records of mean temperature and precipitation totals using a dense network of 184 climatological stations from the Czech Republic for the period of 1961–2010. The selected stations as input dataset in calculation of the SPEI are uniformly covering the Czech Republic. Station elevations range between 158 and 1490 m above sea level (*Fig. 1*). The selected stations represent various climate conditions both in lowland and highland regions and reflect the differences between the maritime and continental weather regimes which manifest across the Czech Republic. Monthly series of temperature and precipitation were taken from the Czech Hydrometeorological Institute (CHMI) CLIDATA database. Measured data were subjected to quality control, gap filling, and homogenization by means of

ProClimDB and AnClim software (*Štěpánek,* 2010*)*. The approach of quality control of daily and monthly temperature and precipitation series combines several methodologies such as differences of neighbor stations comparison, comparison with "expected" values calculated by means of geostatistical methods, etc. Interpolation, where needed, was carried out applying an approach adopted at CHMI. It is based on local linear regression (dependence of given meteorological element on altitude) and universal kriging interpolation, and inverse distance weighting methods (*Šercl* and *Lett,* 2002). The homogeneity of monthly precipitation and temperature series was tested using the Alexandersson's SNHT, bivariate test, and Vincent methods (*Štěpánek et al.,* 2009; *Štěpánek,* 2010*)*.

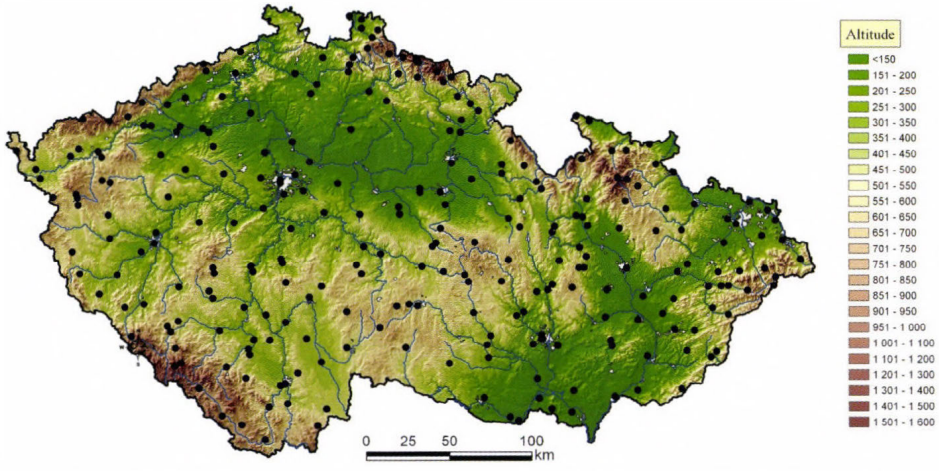

Fig. 1. Location of stations used for the calculation of the SPEI drought index in the Czech Republic.

For the SPEI calculations, the algorithm developed by *Vicente-Serrano et al.* (2010) was used. The SPEI is based on a monthly climatic water balance (precipitation (*P*) minus potential evapotranspiration (*PET*)). *PET* is calculated using the method of *Thornthwaite* (1948). The documentation and executable files for SPEI calculation are freely available at http://digital.csic.es/handle/10261/10002. A batch script was created and used for optimizing the calculation of the SPEI for the 184 stations and five accumulated periods: 1, 3, 6, 12, and 24 months. The SPEI was calculated for each month of the year, but this study refers only to the warm season of the year (from April to September). The drought at these time scales is relevant for agricultural (1-, 3-, and 6-month), hydrological (12-month), and socio-economic

impacts (24-month), respectively. A drought episode was defined as a continuous period of months when the SPEI values were less than –1, while values between –0.99 and 0.99 were considered as normal conditions. Drought categories according to the SPEI are presented in *Table 1*.

Table 1. Drought categories according to the SPEI

SPEI	Drought category	Probability
≥ 2.00	Extreme wet	0.02
1.50 – 1.99	Severe wet	0.06
1.49 – 1.00	Moderate wet	0.10
0.99 – (–0.99)	Normal	0.65
(–1.00) – (–1.49)	Moderate drought	0.10
(–1.50) – (–1.99)	Severe drought	0.05
≤ (–2.00)	Extreme drought	0.02

Taking into consideration the climatic characteristics in the Czech Republic such as the degree of continentality and the diversity of physico-geographic conditions (topography, soil type), the evaluation of drought was carried out in more details for the selected climatic regions. To identify the principal modes of variability of the SPEI at the various time scales, the empirical orthogonal functions (EOF) have been calculated over the territory of the Czech Republic. This approach has been widely used to explore regional patterns of the drought over Europe and various regions of the world (*Dai*, 2011). Based on the patterns of the spatial coefficients of the EOF2 and EOF3 of the SPEI at the considered time scales, we have identified three regions, corresponding to the altitudes below 400 m, between 401 and 700 m, and above 700 m. They correspond, to some extend, to a previous regionalization used in other studies (*Quitt,* 1971*; Tolasz et al.* 2007; *Trnka et al.* 2009*)*. These regions correspond to different land use types with mostly intensive agriculture, less intensive agriculture, and mostly forested with limited agricultural production, respectively. Moreover, these regions also correspond to the climatic classification according to *Quitt* (1971), where three main climatic regions (warm, moderate warm, and cold) were defined on the basis of 14 climatic characteristics [annual number of warm, frost, and ice days, number of overcast and clear days, number of days with snow cover, number of days with precipitation of 1 mm or more, mean air temperature in January, April, July, and October, sum of precipitation in warm (April-September) and cold (October-March) periods of year, as well as the number of days with mean temperature 10 °C and more]. For each station, the SPEI values were analyzed in order to assess the frequency distribution and the drought severity during the warm period of the year in the given regions.

The following analysis was carried out to assess the regional drought characteristics over the Czech Republic:

(1) numerical values of the SPEI at five accumulated periods (1, 3, 6, 12 and 24 months) calculated for each station, which then allowed to evaluate the drought conditions both for entire territory of the Czech Republic and the selected climatic regions;
(2) averaged number of drought episodes (SPEI ≤ -1) during the growing season at various time scales for three SPEI series: (1) at each station, (2) at each climatic region, and (3) at the entire country territory;
(3) averaged number of drought episodes (SPEI ≤ -1) counted during the growing season at various SPEI time scales both for country level and each of the three climatic regions; and
(4) frequency distribution of monthly SPEI values in 7 classes of drought category (%) at five accumulated periods for the above mentioned SPEI series.

3. Results and discussion

3.1. The principal modes of variability of the SPEI

For each station, the monthly series of the SPEI were averaged over six months of the warm season (from April to September). These SPEI series at five accumulated periods (1, 3, 6, 12, and 24 months) were used for the empirical orthogonal functions (EOF) analysis in order to identify the characteristics of drought variability over the territory of the Czech Republic. The patterns of the three leading EOFs of the SPEI are very similar for all of the five accumulated periods. *Figs. 2 a,b,* and *c* show, as example, the spatial patterns of the three leading modes of variability of the SPEI calculated at 6-month lag and averaged over the warm season (from April to September). The spatial coefficients of the EOF1, with few exceptions, have the same sign over the country (*Fig. 2a*). The time series of the principal component (PC1) coefficients shows the temporal evolution of the EOF1 pattern, identifying the dry and wet years, and the intensity of its anomalies in terms of the standard deviation of the PC1 time series (*Fig. 3*). The periods with consecutive dry warm season were 1967–1969, 1981–1983, 1988–1994, and 1998–2000. The year 2003 was the driest during the period of 1961–2010 according to the PC1 of the SPEI at the 6-month accumulation period. The explained variance of the EOF1 ranges between 71 and 61% as the time scale of the accumulated period for calculation of the SPEI increases from 1 month to 24 months (*Table 2*). The pattern of the spatial coefficients of the EOF2 roughly separates the lowland and highland regions (*Fig. 2b*). The explained variance of the EOF2 and EOF3 ranges from 5 to 9% and 4 to 6%, respectively, as the SPEI is calculated for 1–24 months. The spatial

distribution of the EOF2 for all time scales of the SPEI corresponds, to some extend, to the regionalization previously used in other studies (*Tolasz et al.* 2007; *Trnka et al,* 2009) which identified three climatically homogeneous regions, corresponding to the altitudes below 400 m, between 401 and 700 m, and above 700 m (*Fig. 1* and *Fig. 2*). This station classification according to the altitude was further used in this study to assess the spatial and temporal drought characteristics over the Czech Republic.

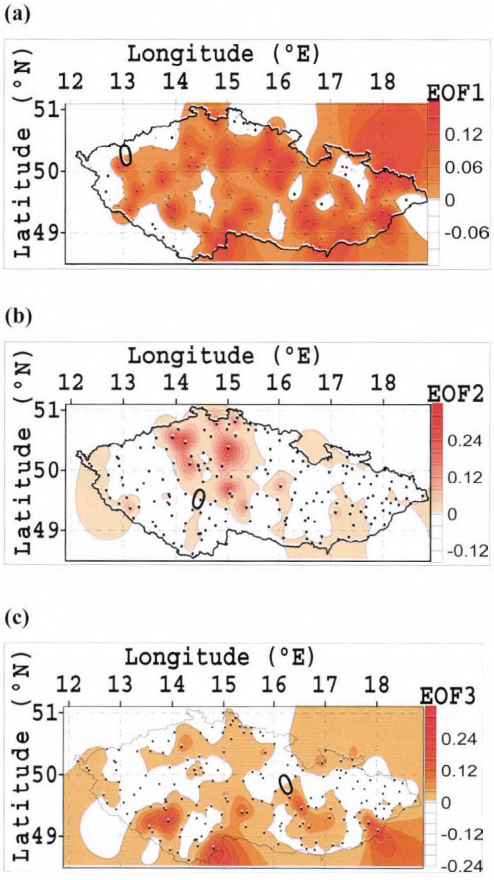

Fig. 2a, b, c,. Spatial patterns of the three leading modes of variability from an EOF of average SPEI values during the warm season (Apr-Sept) over the Czech Republic (1961–2010) at time scale of 6-month.

Table 2. Explained variance of the leading EOFs of averaged SPEI (April-September) over the Czech Republic, 1961–2010

	Explained variance (%)				
	SPEI-1	**SPEI-3**	**SPEI-6**	**SPEI-12**	**SPEI-24**
EOF1	71.68	70.03	69.14	64.46	61.49
EOF2	5.68	6.31	7.33	8.44	9.35
EOF3	4.36	4.12	4.65	5.32	6.05

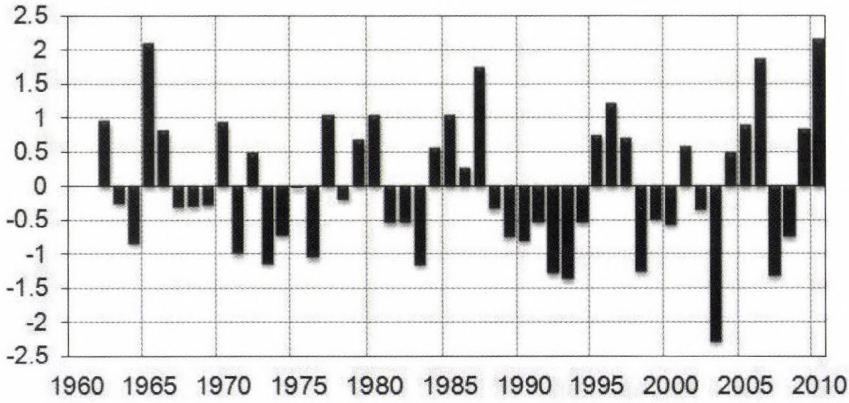

Fig. 3. Standard deviation of principal components (PC1) of SPEI series at 6 months during the warm season (Apr-Sept) over the Czech Republic (1961–2010).

3.2. Frequency distribution of the SPEI values

In this subsection, drought occurrences are analyzed on the basis of frequency distribution of the SPEI values in 7 classes (see *Table 1*). The frequency distribution was calculated as the ratio between the number of occurrences in each SPEI category and the total number of events counted for all stations in a given region for a given time scale (1, 3, 6, 12, and 24 months). The aim here is to identify the areas with high drought frequency detected by the SPEI during the growing season (i.e., April-September). The occurrences in varying drought categories at multiple scales are also analyzed on a regional basis inside the three main climatic regions: warm, moderate warm, and cold (*Quitt,* 1971). For these three regions, the frequency distribution of the SPEI values were calculated based on station records inside each region.

In the *Table 3*, percentage of drought occurrences is expressed in 7 classes of drought categories (%) at time scales of 1, 3, 6, 12, and 24 months for the period of 1961–2010. Normal conditions represent around 65% out of the total

values of SPEI for all times scales, in all three regions, while moderate drought and moderate wet conditions are almost equally distributed at around 10.5%. As the SPEI time scale increases, the difference between the percentages of extremely dry and extremely wet conditions changes on average from 0.2% (SPEI 1-month) to 4% (SPEI 24-month). As it is shown in *Table 3*, the frequency of extreme moisture conditions occurrence (the SPEI values outside ±2) shows a slight tendency toward dry conditions, especially at long time-scales (12 and 24 months).

Table 3. Frequency distribution of monthly SPEI values in 7 classes of drought category (%) at time scales of 1, 3, 6, 12, and 24 months averaged per regions

Region	Extreme drought	Severe drought	Moderate drought	Normal	Moderate wet	Severe wet	Extreme wet
				SPEI-1			
I	2.10	5.37	10.13	64.66	10.22	5.59	1.93
II	2.24	4.71	10.53	64.52	10.56	5.61	1.83
III	1.92	5.06	10.20	65.39	10.24	5.26	1.92
				SPEI-3			
I	2.17	5.57	9.92	65.15	9.70	5.48	2.01
II	1.94	5.53	10.20	65.19	10.13	4.96	2.05
III	1.62	5.64	10.47	64.91	10.62	4.94	1.80
				SPEI-6			
I	2.85	4.83	9.87	64.90	9.96	6.01	1.58
II	2.64	4.86	10.42	64.71	10.24	5.59	1.53
III	2.56	4.39	10.38	65.47	10.08	5.65	1.47
				SPEI-12			
I	3.71	5.67	10.33	62.58	10.70	5.54	1.46
II	3.54	5.36	10.30	63.02	10.91	5.49	1.38
III	3.09	5.55	10.35	63.36	11.09	5.61	0.95
				SPEI-24			
I	5.27	5.89	11.09	60.26	10.42	5.91	1.16
II	5.18	5.4	11.02	60.53	11.33	5.44	1.10
III	4.98	4.95	10.98	61.92	11.36	5.02	0.77

I : altitudes below 400 m,
II : altitudes between 401, and 700 m
III: altitudes above 700 m.

The results of the SPEI values for each station and the corresponding drought categories were mapped using a Surfer program. The Surfer program allows us to generate calculated data points (184 of station observations) on a regular spaced grid. We used the grid to generate the contour map (gridding by

Kriging interpolation technique) of the spatial frequency distribution of moderate, severe, and extreme drought at 1, 3, 6, 12, and 24 months time scales (*Fig. 4*). The spatial interpolation of SPEI values ranges from the longitude of 12.2°E to18.8°E and the latitude of 48.6°N to 51.0°N. The lowest and highest grid points in the dataset have the elevation of 158 and 1490 m, respectively, with 1332 m elevation range (*Table 4*).

Table 4. Frequency distribution of moderate, severe, and extreme drought (%) occurrences during the warm period of the year at different time scales. It is spatially averaged over all stations (λ=12.2°E - 18.8°E; φ=48.6°N - 51.0°N, h=158 1490 m a.s.l.)

	Coordinates			SPEI-1	SPEI-3	SPEI-6	SPEI-12	SPEI-24
	λ° *E*	φ° *N*	h, m					
Moderate drought								
Mean	15.5	49.7	450	10.3	10.1	10.2	10.3	11.1
Minimum	12.2	48.6	158	6.7	6.3	5.7	5.0	4.0
Maximum	18.8	51.0	1490	15.7	14.7	15.0	15.3	17.0
Range	6.6	2.4	1332	9.0	8.3	9.3	10.3	13.0
Severe drought								
Mean	15.5	49.7	450	5.1	5.6	4.8	5.5	5.6
Minimum	12.2	48.6	158	2.7	2.3	1.7	2.3	2.3
Maximum	18.8	51.0	1490	8.7	10.3	8.7	8.7	8.7
Range	6.6	2.4	1332	6.0	8.0	7.0	6.3	6.3
Extreme drought								
Mean	15.5	49.7	450	2.1	2.0	2.7	3.6	5.2
Minimum	12.2	48.6	158	0.7	0.3	1.0	2.0	4.0
Maximum	18.8	51.0	1490	3.7	3.7	5.0	5.7	8.0
Range	6.6	2.4	1332	3.0	3.3	4.0	3.7	4.0

These maps show that the shortest time scales (1 and 3 months) produce clear spatial patterns for the drought frequency. In other words, great percentage of frequency distribution of moderate, severe, and extreme drought occurrences at 1, 3, and 6 months (associated with meteorological and agricultural drought) were identified in regions with relatively low precipitation and high potential evapotranspiration (region I with mostly intensive agriculture, corresponding to the altitudes below 400 m).

The spatial analysis of the SPEI values with **moderate drought** occurrences during the growing period indicates that they tend to occur in the rain shadow of the Ore Mountains, in the south-eastern, south-western, and central parts of Elbe lowland at 1–3 months time-scales. Regions with elevations above 600 m are characterized by the lowest frequencies (lower than 9%) at the

same time scales (left panel of *Fig. 4*). The spatial distribution of frequencies of moderate drought ranges between 6.3% and 15.7% (*Table 4*). The maximum frequencies of moderate drought (15.7% occurrences) are shown in region I (stations situated in lowland region below 400 m a.s.l.). As the time-scale increases from 6 to 12 months, no major changes are observed for maximum frequencies (reached 15.3% at SPEI-12), rather a shift in the low drought occurrences toward the Bohemian Upland region is detected. At 24-month time scale, the moderate droughts occur more frequently and cover more than 60% of the country territory. Their spatial occurence varies between 4% and 17%.

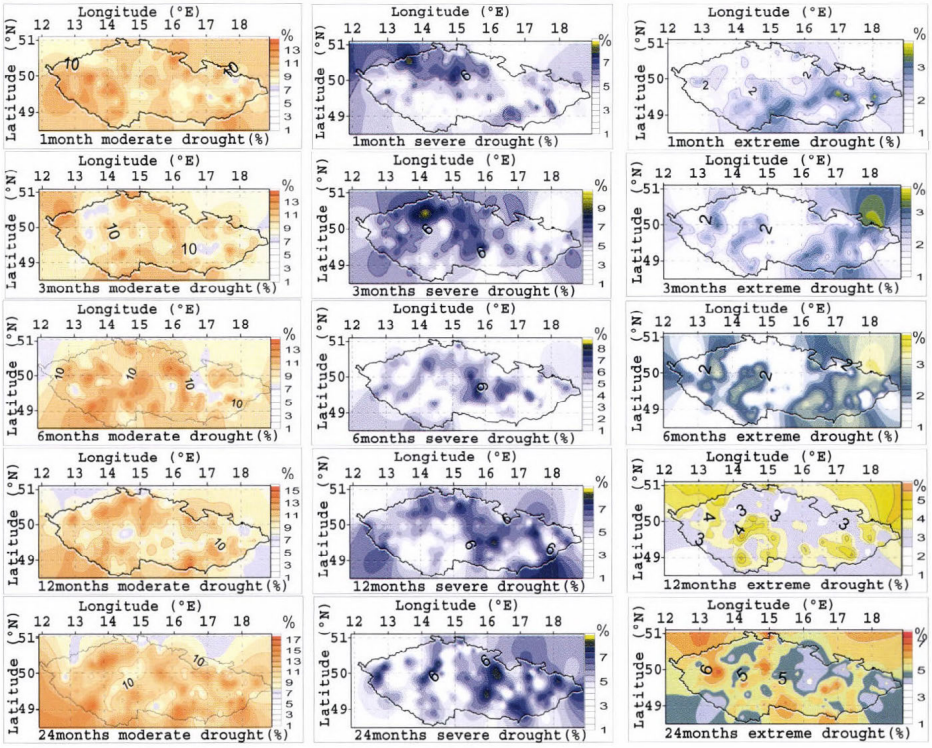

Fig. 4. Frequency distribution of SPEI values in moderate (left panel), severe (central panel), and extreme (right panel) drought categories (%) at time scales of 1, 3, 6, 12, and 24 months averaged for 50 years (1961–2010).

The occurrence of the **severe droughts** at shorter time-scales (1–3 months) was identified within the regions with the highest drought risk in the Czech Republic. According to the SPEI values, we found that high frequency of severe drought occurrences was detected in the following regions: lowlands of the Elbe river valley, central Bohemia, southern Moravia, and lowlands of southeastern

and southern Bohemia (central panel of *Fig. 4*). The same results obtained by different drought indices are highlighted in other studies (*Tolasz et al.* 2007; *Potop et al.* 2008; *Trnka et al.* 2009; *Potop et al.* 2010; *Možný et al.* 2012; *Potop et al.* 2011). These maps show the spatial distribution of severe drought which shifts from short-term (1 month, meteorological drought) and medium-term (3 and 6 months, agricultural drought) to long-term droughts (12 and 24 months, hydrological drought). Severe meteorological drought (SPEI at 1 month) identified first in the north-western Bohemia and southern Moravia have then extended at longer time scales in Elbe lowland and south-eastern areas. Not significant differences are shown in the spatial distribution of severe drought occurrences as the time scale for calculation of SPEI was increased (*Table 4*). The maximum frequency of severe drought occurrences ranges between 8.7% and 10%, while on average at country level it is 5.5%.

As for the **extreme droughts,** regional differences in its occurrence are observed when increasing the SPEI time-scales (right panel of *Fig. 4*). The areas affected by extreme drought evolve gradually, and the regions turn to be affected by higher frequency of extreme drought from shorter time-scales (meteorological drought) to longer time-scales (hydrological drought). The resulted maps show more spatial variability in frequency of drought at 12 and 24 months than for shorter time scales. In general, the SPEI at the 24 months time-scale indicates the more complex patterns of extreme drought frequency (right panel of *Fig. 4*). The highest percentage of extreme drought occurrences is 3.7% at short-term scale (SPE-1), whereas at medium-term (SPEI-3 and SPEI-6 months) and long-term (SPEI-12, SPEI-24) the drought ranges from 5.7 to 8.0%. The frequency of extreme drought is the lowest or missing at stations with altitude more than 1000 m (0.3%).

3.3. Spectral analysis

The periodograms via fast fourier transform spectral techniques were also applied to search for significant periodicities in the time series of the SPEI≤–1 (moderate to extreme drought) averaged for the six months of the growing season (April-September). *Table 5* presents the results of the spectral analysis: the peak frequency and the length of cycles exceeding the 95% confidence level at various time-scales. The frequency is calculated as the number of cycles per time unit (where each observation is treated as one unit of time). The results of the peak frequency and the length of cycle in spectral analysis calculated for the three regions have been analyzed. Thus, at 1 month SPEI, the peak frequency of 0.41 (the number of units of time necessary to complete one full cycle) corresponds to a 2.5-year drought occurrence in the region I, while in the region II and region III the frequency of 0.34 corresponds to the occurrence of drought in every 3 years. This means that frequent meteorological drought events from moderate to severe in the SPEI-1 series are observed in every 2.5 years in the

region I that is considered the warmest and driest area in the country, while in the regions II and III the frequency of meteorological drought slightly decreased (*Table 5*). A clear peak frequency and cycle length of 3-month and 6-month (corresponding to agricultural drought) was 0.20 standing for the drought occurence in every 5 years in all regions. The same result was reported in previous studies (*Potop et al.*, 2008; *Potop et al.*, 2010) which combine the three drought indices as a tool for the identification of the drought frequency in the Czech Republic. At the time-scale of 12-month (hydrological drought), the frequency peak was 0.11 corresponding to a drought occurrence period of 9.4 years. As the results in *Table 5* show, at time scale of 24-month (the largest socio-economic impact) there is a well-defined regional drought frequency pattern. In the region with the altitudes below 400 m, the frequency peak of drought was 0.13 corresponding to a period of drought occurrence of 7.6 years, while in the regions with altitudes between 401 and 700 m and above 700 m the frequency peaks were at 0.11 and 0.06, standing for the occurrence of drought in every 9.4 and 15.3 years, respectively (*Table 5*).

Table 5. Spectral analysis of SPEI≤-1 series (at 95% confidence level) at time-scales 1, 3, 6, 12, and 24 months (1961–2010) per regions

	SPEI-1	SPEI-3	SPEI-6	SPEI-12	SPEI-24
I: the altitudes below 400 m					
Peak of frequency, %	0.41	0.20	0.20	0.11	0.13
Length of cycle, years	2.50	5.00	5.00	9.40	7.60
II: the altitudes between 401 and 700 m					
Peak of frequency, %	0.34	0.20	0.20	0.11	0.11
Length of cycle, years	3.0	5.0	5.0	9.4	9.40
III: the altitudes above 700 m					
Peak of frequency, %	0.34	0.20	0.22	0.11	0.06
Length of cycle, years	3.0	5.0	5.00	9.40	15.30

4. Conclusions

In this study, the characteristics of drought over the Czech Republic at various time-scales during the growing season (April-September) were analyzed. The drought was quantified with the standardized precipitation evapotranspiration index (SPEI) at 184 climatological stations during the period of 1961–2010. The main results can be summarized as follows:

(a) In order to identify the drought variability over the territory of Czech Republic the empirical orthogonal functions (EOF) approach was used.

According to spatial distribution of coefficients of the EOF2, three drought homogeneous regions were distinguished, corresponding to the altitudes below 400 m, between 401 and 700 m, andabove 700 m: the lowlands and the high altitude regions.

(b) Regarding the drought time scales, most parts of lowlands and partially of highland regions are vulnerable to moderate agricultural drought during growing season. For the entire period of study, the vulnerability of extreme agricultural drought is low. However, the evolution of agricultural drought in the second half of the 20th century and the first decade of the 21st century showed increasing frequency that has been reinforced by long dry periods in the 1990s and 2000s. The drought during these periods was associated with high temperature anomalies (i.e., more than 2.5 °C). Consequently, the SPEI has the ability to detect the reinforcement of drought severity due to the temperature increasing during the 1990s and 2000s.

(c) The occurrences of various drought time-scales and severity categories show distinct patterns. The maximum frequencies of **moderate and severe drought** were identified at stations situated in lowland regions below 400 m. High number of severe meteorological and agricultural drought events also occured in the southern Moravia, the north-western Bohemian areas, the south-eastern areas, and in the Elbe lowland. In other words, the majority of the historical droughts occurred in the regions corresponding to the altitudes below 400 m and between 401 and 700 m. The highest percentage of **extreme drought** occurrences was 3.7% at short-term scale, whereas the highest percentage of medium-term and long-term droughts ranges from 5.7 to 8.0%. The frequency of extreme drought is the lowest in the region with stations with altitude higher than 1000 m (0.3%).

(d) The short-term drought (meteorological drought) and mid-term drought (impacting agricultural production) occur at the whole territory of the country approximately in every three and five years, respectively. The long-term drought (impacting the water system) can occur in every nine years in all of the regions.

Acknowledgements: The research on drought conditions in the Czech Republic was supported by S grant of MSMT CR and projects OC10010, 6046070901, CzechGlobe – Centre for Global Climate Change Impacts Studies, Reg. No. CZ.1.05/1.1.00/02.0073. The authors would like to thank Sergio M. Vicente-Serrano (Instituto Pirenaico de Ecologia-CSIC, Zaragoza, Spain) for providing the detailed algorithm to calculate the SPEI.

References

Brázdil, R., Trnka, M., Dobrovolný, P., Chroma, K., Hlavinka, P. and *Žalud, Z.*, 2009: Variability of droughts in the Czech Republic, 1881-2006. *Theor. Appl. Climatol. 97*, 297–315.

Dai, A., 2011: Characteristics and trends in various forms of the Palmer Drought Severity Index during 1900–2008. *J. Geophys.Res.116*, D12115.

Možný, M., Trnka, M., Žalud, Z., Hlavinka, P., Nekovař, J., Potop, V. and *Virag, M.*, 2012: Use of a soil moisture network for drought monitoring in the Czech Republic. *Theor. Appl. Climatol.* 107, 99–111.

Potop, V., Türkott, L. and *Kožnarová, V.*, 2008: Spatiotemporal characteristics of drought in Czechia. *Sci. Agr. Bohemica 39*, 258–268.

Potop, V., Türkott, L., Kožnarová, V. and *Možný, M.*, 2010: Drought episodes in the Czech Republic and their potential effects in agriculture. *Theor. Appl. Climatol. 99*, 373–388.

Potop, V. and *Možný, M.*, 2011a: The application a new drought index - standardized precipitation evapotranspiration index in the Czech Republic. In: *Mikroklima a mezoklima krajinných struktur a antropogenních prostředí.*(eds*: Středová, H., Rožnovský, J., Litschmann, T), Skalní mlýn*, 2. – 4.2. 2011. (CD).

Potop, V. and *Možný, M.*, 2011b: Examination of the effect of evapotranspiration as an output parameter in SPEI drought index in Central Bohemian region. In: Bioclimate: Source and Limit of Social Development, International Scientific Conference, (eds: Šiška, B., Hauptvogl, M., Eliašová, M.) 6–9. September 2011, Topoľčianky, Slovakia. (CD).

Potop, V. and *Soukup J.*, 2011: Assessing risk of dry episodes during growing seasons of vegetable crops in Polabí, Czech Republic. In: *1st Climate Change, Economic Development, Environment and People Conference.* 14-16 September, 2011, Novi Sad, Serbia.

Potop, V., Soukup, J., and *Možný, M.*, 2011: Drought at various time-scales for secular lowland climatologically stations in the Czech Republic. *Meteorologické Zpravy 64*, 177–188.

Potop, V., Možný, M., and *Soukup, J.*, 2012: Drought at various time scales in the lowland regions and their impact on vegetable crops in the Czech Republic. *Agric. Forest Meteorol. 156*, 121–133.

Potop, V., Boroneanț, C., Možný, M., Štěpánek, P. and *Skalák, P.*, 2012a: Observed evolution of drought episodes assessed with the Standardized Precipitation Evapotranspiration Index (SPEI) over the Czech Republic. In: *EGU General Assembly 2012. Geophysical Research Abstracts Vol. 14, EGU2012-7681*, 2012, 22–27 April, Vienna.

Potop, V., Boroneanț, C., Štěpánek, P., Skalák, P. and *Možný, M.*, 2012b: Projected changes in the evolution of drought assessed with the SPEI over the Czech Republic. In: *EGU General Assembly 2012. Geophysical Research Abstracts Vol. 14, EGU2012-7681,* 2012, 22–27 April, Vienna.

Quitt, E., 1971: Climatic regions of Czechoslovakia. *Studia Geographica, sv. 16. Brno: Czechoslovak Academy of Science – Institute of Geography. 79.*

Šercl, P. and *Lett, P., 2002:* Výpočet rastru srážek v prostředí GIS (s využitím ArcView Spatial Analyst). *Uživatelská příručka verze 2.0.1,* ČHMÚ, OPV, Praha.

Štěpánek, P., 2010: ProClimDB – software for processing climatological datasets. CHMI, regional office Brno. http://www.climahom.eu/ProcData.html.

Štěpánek, P., Zahradníček, P. and *Skalák, P.*, 2009: Data quality control and homogenization of air temperature and precipitation series in the area of the Czech Republic in the period 1961–2007. *Adv. Sci. Res. 3*, 23–26.

Thornthwaite, C.W., 1948: An approach toward a rational classification of climate. Geogr Rev. 38, 55–94.

Tolasz, R., (ed), 2007: Atlas podnebí Česká. Climate Atlas of Czechia. ČHMÚ, Univerzita Palackého v Olomouci, Praha-Olomouc, 254.

Trnka, M., Dubrovský, M., Svoboda, M.D., Semeradová, D., Hayes, M.J., Žalud, Z. and *Wilhite. D.A.*, 2009: Developing a regional drought climatology for the Czech Republic for 1961–2000. *Int J Climatol 29*, 863–883.

Vicente-Serrano, S.M., Beguería, S. and *López-Moreno, J.I.*, 2010: A Multi-scalar drought index sensitive to global warming: The Standardized Precipitation Evapotranspiration Index – SPEI. *J. Climate 23*, 1696–1718.

Vicente-Serrano, S.M., Beguería, S. and *López-Moreno, J.I.*, 2011: Comment on "Characteristic and trends in various forms on the Palmer Drought Severity Index (PDSI) during 1900-2008" by Aiguo Dai. *J. Geograph. Res.116*, D19112.

IDŐJÁRÁS

Quarterly Journal of the Hungarian Meteorological Service
Vol. 116, No. 4, October–December 2012, pp. 297–321

Comprehensive assessment of climate change policies and measures in Hungary: concerns and tasks in an underestimated challenge

Sándor Molnár[1]* and **Márk Molnár**[2]

[1] *Szent István University, Faculty of Mechanical Engineering, Institute of Mathematics and Informatics, Páter K. u.1,H- 2103 Gödöllő,Hungary*

[2] *Szent István University, Faculty of Economics and Business Management, Institute of Economic Sciences, Páter K. u.1,H- 2103 Gödöllő,Hungary*

**Corresponding author E-mail: Molnar.Sandor@gek.szie.hu*

(Manuscript received in final form Oktober 15, 2012)

Abstract—Parties included in Annex I to the UNFCCC are requested to submit national communications to the Secretariat. This report strives to present a review of the results of the 5th National Communication (NC5) of Hungary with respect to the relevant provisions of the Convention and Article 8 of the Kyoto Protocol.

Key-words: greenhouse gas emissions, inventory, projections, National Communication

1. Introduction

For Hungary, the Convention entered into force on May 25, 1994 and the Kyoto Protocol on February 16, 2005. Under the Kyoto Protocol, Hungary committed itself to reducing its net greenhouse gas (GHG) emissions by 6 percent compared with the average level for the period 1985–1987 (base year) during the first commitment period from 2008 to 2012.

Hungary's 5th National Communication (NC5) complies in general with the UNFCCC Guidelines for the preparation of national communications, and

Hungary considered most of the recommendations provided in the report on the in-depth review of the 4th National Communication (NC4) of Hungary.

The NC5 covers all of the sections required by the UNFCCC reporting guidelines and most of the supplementary information required under Article 7, paragraph 2, of the Kyoto Protocol, except for information on supplementarity relating to the mechanisms pursuant to Articles 6, 12, and 17 of the Kyoto Protocol (see Section 2). The NC5 does not include information required by the UNFCCC reporting guidelines on steps undertaken to limit or reduce GHG emissions from aviation and marine bunkers and on international activities relating to systematic observations, including Global Climate Observing System (GCOS) activities.

2. Assessment of the current situation

In its NC5, Hungary has provided an overall description of the national circumstances and has elaborated on the framework legislation and key policy documents on climate change. Information has been provided on the government structure, population, geography, climate, settlement structure and building stock, economy and relevant economic sectors. However, while national circumstances were well described in the NC5, the analysis of how these national circumstances and changes affect GHG emissions and removals in Hungary could be further enhanced.

The main drivers of emission trends in Hungary include overall restructuring and reducing the levels of economic activity, and restructuring of primary energy supply, since Hungary undertook a transition from a centrally planned economy to a market based economy that has taken place in the 1990s. Since 1995, the economy has grown, with associated small growth in energy consumption, while GHG emissions have remained relatively stable and have decreased even further since 2005. The transparency of future national communications can be further enhanced by providing more information on the changes in sectoral emissions (e.g., transport, energy, industrial, and agricultural emissions) and the relationship between sectoral emissions and changes in activity, and on how the national circumstances are driving these changes. *Table 1* summaries the relevant indicators of emissions and removals for Hungary.

The Hungarian Meteorological Service (together with the Forestry Directorate of the Central Agricultural Office and the Forest Research Institute) is responsible for the national GHG inventory. Climate change policy is underpinned by the National Climate Change Strategy 2008–2025 (NCCS), and a significant proportion of the PaMs are implemented at the national level. The implementation of climate change policy is set out in the National Climate Change Programme.

*Table 1.*Indicators relevant to greenhouse gas emissions and removals for Hungary

	1990	1995	2000	2005	2008	Change[a] 1990–2000 (%)	Change 2000–2008 (%)	Change[a] 1990–2008 (%)
Population (million)	10.4	10.3	10.2	10.1	10.0	–1.5	–1.7	–3.2
GDP (USD 2 000 billion using PPP)	115.1	102.1	123.7	152.2	160.8	7.5	30.0	39.8
TPES (Mtoe)	28.7	25.9	25.0	27.6	26.5	–12.8	5.9	–7.7
GDP per capita (USD 2 000 thousand using PPP)	11.1	9.9	12.1	15.1	16.0	9.2	32.2	44.4
TPES per capita (toe)	2.8	2.5	2.4	2.7	2.6	–11.4	7.7	–4.7
GHG emissions without LULUCF (Tg CO_2 eq)	114.5[a]	78.7	77.1	79.8	73.1	–32.7	–5.1	–36.1
GHG emissions with LULUCF (Tg CO_2 eq)	112.3[a]	71.9	75.9	75.3	68.6	–32.5	–9.5	–38.9
CO_2 emissions per capita (Mg)	8.2	5.9	5.7	6.0	5.6	–30.0	–2.3	–31.6
CO_2 emissions per GDP unit (kg per 2 000 USD using PPP)	0.7	0.6	0.5	0.4	0.4	–35.9	–15.4	–45.8
GHG emissions per capita (Mg CO_2 eq)	11.0	7.6	7.5	7.9	7.3	–30.3	–3.5	–32.7
GHG emissions per GDP unit (kg CO_2 eq per 2 000 USD using PPP)	1.0	0.8	0.6	0.5	0.5	–36.2	–27.0	–53.4

Abbreviations: GDP = gross domestic product, GHG = greenhouse gas, LULUCF = land use, land-use change and forestry, PPP = purchasing power parity, TPES = total primary energy supply.

Sources: (1) GHG emissions data: Hungary's 2010 greenhouse gas inventory submission; (2) Population, GDP and TPES data: International Energy Agency.

Note: The ratios per capita and per GDP unit are calculated relative to GHG emissions without LULUCF; the ratios are calculated using the exact (not rounded) values and may therefore differ from a ratio calculated with the rounded numbers provided in the table.

[a] For emissions, base year data are used instead of 1990 data, whereas GDP, TPES, and population data are for 1990, which may lead to some inconsistency in the calculation of GHG emissions per capita and per GDP unit.

GHG emission trends are provided for the period 1985–2007. This information is consistent with the 2009 national GHG inventory submission. Total GHG emissions excluding emissions and removals from land use, land-use change, and forestry (LULUCF) decreased by 36.1 percent between the base year and 2008, whereas total GHG emissions including net emissions or removals from LULUCF decreased by 38.9 percent. This was mainly attributed to CO_2 emissions, which decreased by 33.8 percent over this period. Emissions of methane (CH_4) also decreased by 28.5 percent, while emissions of nitrous oxide (N_2O) decreased by 56.9 percent. Most of these decreases were experienced during the years 1987–1995 (trends for 1987–1995: CO_2 27.3 percent, CH_4 21.3 percent, N_2O 56.0 percent, and total GHGs 31.1 percent). Emissions of F-gases accounted for about 0.30 percent of total GHG emissions

in 1995 and 1.28 percent in 2008. Total GHG emissions have decreased, mostly due to GHG emission reductions in industry (manufacturing industry and industrial processes), agriculture, and energy use in the sector "others" (residential and commercial sectors), driven chiefly by a decline in industrial output, restructuring and associated energy use, and agricultural production. During the same period that emissions from transport grew substantially, those from waste also increased. *Table 2* provides an overview of GHG emissions by sector from the base year to 2008.

Table 2. Greenhouse gas emissions by sector in Hungary, 1990–2008

	GHG emissions (Tg CO_2 eq)							Change (%)		Shares[a] by sector (%)	
Sector	**BY**	**1990**	**1995**	**2000**	**2005**	**2007**	**2008**	**BY [a] –2008**	**2007 –2008**	**BY**	**2008**
1. Energy	82.9	70.5	60.8	57.8	59.8	56.7	55.5	–33.1	–2.1	72.3	75.9
A1. Energy industries	27.3	22.2	23.9	23.6	18.8	20.6	19.7	–27.8	–4.3	23.8	26.9
A2. Manufacturing industries and construction	20.1	15.0	11.0	8.5	8.7	7.2	7.0	–65.4	–3.7	17.6	9.5
A3. Transport	7.8	8.2	7.0	8.8	12.2	12.8	12.9	65.7	0.4	6.8	17.6
A4.–A5. Other	25.0	22.7	16.4	14.5	17.9	13.9	13.8	–44.7	–0.5	21.8	18.9
B. Fugitive emissions	2.7	2.4	2.5	2.5	2.2	2.2	2.1	–21.7	–1.1	2.4	2.9
2. Industrial processes	10.9	8.9	5.5	6.3	7.0	6.0	4.7	–56.5	–20.6	9.5	6.5
3. Solvent and other product use	0.3	0.2	0.2	0.2	0.4	0.4	0.4	42.8	11.0	0.2	0.6
4. Agriculture	17.5	14.5	8.7	9.1	8.8	8.9	8.8	–49.8	–1.4	15.3	12.0
5. LULUCF	–2.3	–2.9	–6.8	–1.2	–4.6	–2.9	–4.5	100.8	57.0	–2.0	–6.2
6. Waste	3.0	3.3	3.5	3.7	3.9	3.8	3.7	25.3	–1.6	2.6	5.1
7. Other	NA	NA	NA	NA	NA	NA	NA	NA	NA	NA	NA
GHG total with LULUCF	**112.3**	**94.4**	**71.9**	**75.9**	**75.3**	**72.8**	**68.6**	**–38.9**	**–5.8**	**NA**	**NA**
GHG total without LULUCF	**114.5**	**97.4**	**78.7**	**77.1**	**79.8**	**75.7**	**73.1**	**–36.1**	**–3.4**	**100.0**	**100.0**

Abbreviations: BY = base year, GHG = greenhouse gas, LULUCF = land use, land-use change and forestry, NA= not applicable.

Note: The changes in emissions and the shares by sector are calculated using the exact (not rounded) values and may therefore differ from values calculated with the rounded numbers provided in the table.

[a] The shares of sectors are calculated relative to GHG emissions without LULUCF; for the LULUCF sector, the negative values indicate the share of GHG emissions that was offset by GHG removals through LULUCF.

After the sharp decline in emissions during the period 1987–1995, Hungary's GHG emissions remained relatively stable until 2005 against the backdrop of stable economic growth. This suggests a decoupling of economic growth from the GHG emissions for that period. During the last three years

between 2008 and 2009, Hungary's emissions decreased even further, by 8.4 percent, mainly due to a decrease in energy consumption, the extreme mild winter in 2007, and modernization in the chemical industry. Transparency of the reporting on GHG emission trends could be improved by providing additional information on sector-specific trends and relevant drivers.

3. Policies and measures

The key framework for climate and energy policy is the NCCS 2008–2025. The National Climate Change Programme (NCCP) gives effect to the implementation of the strategy, and the progress made in implementing the NCCS is reviewed every two years. The NCCS attaches priority to meeting the objectives of the EU directives and international conventions related to climate change that lead to a lower carbon economy, avoid adverse, ecological and social economic effects, and promote awareness of climate change.

Hungary expects to meet its Kyoto Protocol emission reduction target without any further measures. In accordance with the 'without measures' scenario, Hungary expects its emissions to be 11.8 percent below the base year level compared to the Kyoto target of 6 percent below the base year level. Hungary joined the EU ETS in 2005. Most emissions allowances are allocated freely during 2008–2012; however, from 2012, the quantity of free allowances will decrease by 17.4 percent compared to the average annual total quantity of allowances currently issued by EU member States.

Improvements to the energy efficiency of the residential sector have provided the most cost-effective and biggest impact on reducing GHG emissions in Hungary. The Hungarian residential sector is dominated by large pre-fabricated apartment blocks built prior to the 1990s with low thermal efficiency, heated by district heating, and commonly fueled by oil and coal. Emissions from this sector decreased by 64 percent in 2008 compared to the base year level due to energy-efficiency improvements and the shift from coal to gas in the residential sector. In the 1990s and 2000s, policies to improve energy efficiency in the residential sector were strengthened and their benefits, in terms of improving air quality and human health and providing employment opportunities during the recession, were recognized.

The NC5 provided estimates of the effects of PaMs by sector and by gas for most sectors except for the agriculture, industrial processes, and waste sectors. Reduction in agriculture emissions would predominantly be from N_2O.

Limited information is available on the implementation costs of PaMs. Retrofitting and improving the energy efficiency of the building stock has largely been funded through the Green Investment Scheme (GIS) with finance raised from the sale of assigned amount units (AAUs). Hungary has invested 7.5 billion Hungarian forints (HUF) from the GIS into retrofitting and improving the

energy efficiency of the building stock. Hungary anticipates using the GIS further to fund investment in renewable energy supply.

Hungary has no PaMs in the agriculture sector that could potentially increase emissions through a growth in the output of livestock and cropping. None of the PaMs in the agricultural sector directly addressed GHG emission reduction. Further, the potential effects can hardly be quantified so that no precise information is available on the effects of PaMs on agriculture emission. *Table 3* provides a summary of the reported information on the PaMs of Hungary.

*Table 3.*Summary of information on policies and measures

Major policies and measures	**Examples/comments**
Policy framework and cross-sectoral measures	
National Climate Change Strategy (NCCS)	National framework for making climate change related decisions. The National Climate Change Programme is adopted every two years to implement the NCCS
Emissions trading	European Union emissions trading scheme (EU ETS) from 2005. The existing installations have been allocated an average of 26.1 Mt of CO_2 emission allowances per year during the period 2008–2012. About 13.1 Mt are reserved for new entrants during this period
Policies and measures by sector	
Energy	
National Energy Efficiency Action Plan (NEEAP)	The NEEAP spans from 2007 to 2013 and encompasses a number of national energy-saving programmes and measures, including the Energy Saving Credit Fund and the Energy Certificate
Promotion of renewable energy sources	The Renewable Energy Strategy (RES) includes feed-in-tariffs for renewables and waste, and certificates of origin for RES electricity. It also supports various projects, including those promoting biomass, biogas, geothermal energy, and small-scale wind turbines
	In line with the EU renewable energy directive, the renewables target is set to be 13 percent by 2020, which translates to 96 PJ based on a post-economic recession projection of energy supply
Energy-efficiency improvements	The Hungarian Energy Efficiency Strategy and Action Plan designates the following areas for policy intervention: residential buildings, institutional buildings, energy transformation, traffic and transport, architecture, and typical energy consumption product groups that may have a more significant influence on the volume of energy needs
	Energy efficiency in housing, funded through the Green Investment Scheme (GIS)
	Energy efficiency in communal residences, which includes the upgrading of district heating systems and the conversion from coal to gas
Combined heat and power generation	Obligatory takeover of electricity produced through combined heat and power
Nuclear power	Refurbishment and extension of existing capacity (6–10 Mt CO_2 eq)

Major policies and measures	Examples/comments
Transport	
Renewable transport target	Target of 10% renewable transport through biofuels and electric motives (including passenger cars)
Road pricing	Tolls for heavy vehicles
Industrial processes	
Joint implementation	Project implemented to eliminate almost all N_2O emissions from nitric acid production
Fluorinated gases	Hungary is implementing the EU directive on F-gases
Agriculture	
New Hungary Rural Development Strategic Plan	Increase of energy plantations and energy forests
	EU nitrates directive
	Modernization of agriculture livestock production, crop production and machinery
	Financial support for improved environmental management and animal management
Forestry	
Afforestation	Grants for afforestation
	Restrictions on deforestation: any deforestation must be offset with equal or greater afforestation elsewhere
	Emphasis on natural regeneration and the return to the natural state wherever possible
Waste	
	Waste prevention (including hazardous waste) and packaging reduction, as mandated by the EU
	Landfill gas flaring or capture if economically viable
	Upgrading waste incineration in Budapest, employing heat used for electricity and district heating
	Reduction of landfill sites and rehabilitation of old sites

Note: The greenhouse gas emission reduction estimates given for some measures (in parentheses) are reductions in CO_2 or CO_2 eq for the year 2020.

3.1. Policy framework and cross-sectoral measures

The current climate change policy is elaborated in the NCCS 2008–2025. The NCCS sets out the overall strategy for Hungary to address climate change, including mitigation and adaptation, as well as the communication of climate change. The NCCS was to be reviewed after two years and then every five years. However, the 2010 review was deferred to 2011 because of a substantive government restructuring and the preparation for the presidency of the EU

during the first half of 2011. The NCCP implements the climate change measures, outlined in the NCCS and is reviewed every two years, and a new two-year programme is produced.

Hungary's 2020 pledged emissions reduction target compared to 1990 levels is a reduction of 16 –25 percent if the EU target is 20 percent, or a reduction of 27–34 percent if the EU target is 30 percent. The target for 2050 is a reduction of 80 percent, and Hungary's vision for 2050 will be further elaborated in the revised NCCS during 2011. The higher end of the less stringent target (16–25 percent) is commensurate with the 'with measures' projected reduction relative to 1990 of 26 percent, and the higher end of the more stringent target (27–34 percent) is commensurate with the projected reduction in emissions under the 'with additional measures' projection for 2020 relative to 1990. Hungary could be expected to meet the less stringent target with existing measures and the more stringent target with additional measures. Hungary has not reported on how it intends to make use of forestry removals to meet its 2020 and 2050 targets.

Under the EU directive on energy efficiency, Hungary is to improve energy efficiency by 20 percent between 2008 and 2020 in the non-EU ETS trading sector. The energy efficiency allocation plan is yet to enter into force. EU directive 2009/28/EK sets a renewable energy target for Hungary's primary energy supply of 13 percent by 2020.

Hungary complies with the climate change related directives of the EU; Hungary is planning to implement the EU directive on F-gases. Under the EU renewable energy target directive (2009/29/EK), Hungary's target is to meet 13 percent of total primary energy demand from renewable sources. The target, in absolute terms, equates to 96 PJ (13 percent of total projected energy supply in 2020 of 740 PJ) by 2020 and was lowered to take into consideration lower-than-expected energy demand in 2020 due to the recent global financial recession. The transport sector's target is to meet 10 percent of its energy demand from renewable sources, including biofuels and the electrification of road and rail transport. In addition, energy efficiency is to be improved by 20 percent between 2008 and 2020 in the non-EU ETS trading sector. The energy efficiency allocation plan is yet to enter into force.

3.2. Policies and measures in the energy sector

Between the base year and 2008, GHG emissions from the energy sector decreased by 33.1 percent (27,392.9 Gg CO_2 eq), mainly driven by reductions in energy demand in manufacturing industries and construction (–65.4 percent or –13,154.6 Gg CO_2 eq), and in the residential sector (–45.8 percent or –7,643.4 Gg CO_2 eq). Between the base year and 1993, Hungary's economic activity was substantially reduced during the transition to a market-based economy, causing the large reduction in emissions from manufacturing

industries and construction. Emissions from the residential and commercial sectors were reduced by the shift from coal-fired to natural gas in heating plants and improvements in the thermal efficiency of the residential and commercial sectors.

The share of fossil-based fuel consumption in Hungary's energy supply declined from 1990 to 2007 due to changes in economic activity. Between 1990 and 2007, coal consumption decreased by 60 percent (from 186.4 to 74.2 PJ), oil consumption decreased by 57 percent (from 80.9 to 35.1 PJ), and gas consumption decreased by 47 percent (from 159.6 to 83.9 PJ). Over the same period, nuclear power increased by 7 percent (from 149.7 to 160 PJ), and renewables are estimated to have increased by 65 percent (from 18.5 to 30.6 PJ). Hungary also intends to make use of geothermal heat for district heating.

Nuclear power provided almost 40 percent of Hungary's electricity supply in 2007. Hungary has implemented a parliamentary decree to extend the lifetime of the existing nuclear power plant and to increase the capacity of each of the four units from 440 MW to 500 MW. The refurbishment will ensure that at least 40 percent of future electricity needs are met from nuclear power. Depending on the assumed fuel mix for generation, the refurbishment of the nuclear power plant will reduce Hungary's GHG emissions by 6–10 Mt CO_2 eq annually.

Renewable energy sources. The renewable energy target has been set using energy projections made since the onset of the global recession, as expectations of future energy demand are now lower than projected before the recession. Preliminary sectoral targets to achieve this aggregate target are divided as follows: 14.3 percent for heating and cooling, 13.8 percent for power generation, and 10 percent for transport. Hungary has not yet determined how the renewable target will be financed but expects to make use of GIS funds.

Energy efficiency. Hungary has successfully reduced GHG emissions in the energy sector by increasing the energy efficiency of buildings, and the estimates suggest that there is still scope for further improvement. Buildings in need of thermal efficiency improvements are firstly graded for their thermal efficiency. The building owners finance the improvements to their building and the building is then graded again for thermal efficiency. A grant of up to 60 percent is paid for successful improvements. Larger grants may be paid if the upgrade exceeds expectations and a higher grade is achieved. Funding for the programme is provided from the GIS. The returns, in terms of energy savings to the programme, are high. From an initial investment of HUF 3.3 billion, the energy savings are estimated to be HUF 30 billion. The benefits of the scheme appear large and could possibly occur under 'business as usual'. There is a need for Hungary to continue to re-evaluate the scheme in order to ensure that the improvements do not occur under 'business as usual', and because the benefits of the scheme are likely to diminish over time as energy efficiency is improved.

Residential and commercial sectors. Emissions from the residential and commercial sectors have decreased from 16.7 Mt CO_2 eq to 9.1 Mt CO_2 eq

between the base year and 2008. The reduction is largely due to improvements in energy efficiency and the shift from coal-fired heating to gas as well as improvements to the thermal efficiency of pre-1992 residential and commercial buildings. Other PaMs for the residential sector include: voluntary measures and awareness-raising campaigns, including labelling of appliances and household boilers; and financial incentives for the replacement of refrigerators and freezers with more efficient appliances. Buildings in Hungary are required to have energy rating certificates prior to sale.

Transport sector. In contrast to the other sectors where emissions declined, emissions from the transport sector increased by 65.7 percent during the period 1990 –2008. This reflects changes in lifestyle and a major shift from public transport to private cars. The transport fleet underwent significant modernization during the 1990s and up to 2004, from an old car fleet with a high proportion of 2-stroke engines to modern vehicles meeting EU emissions standards. However, the average age of the cars increased from 10.5 years to 11.7 years between 2004 and 2008, largely due to financial difficulties preventing individuals from financing new vehicles. Hungary's road infrastructure is still expanding in order to catch up with the level of road infrastructure in more developed EU countries. Hungary applies a differentiated road tax on purchases of motor vehicles (irrespective of age) graduated on emissions standards, which is in inverse relationship to the vehicle emissions standard. Environmental testing for smoky vehicles was previously annual for cars older than four years. In recent years, each has to go through a mechanical test every second year, however, this includes environmental testing too. Compliance with vehicle testing is still strictly enforced, but with less frequency, which is more cost effective for the vehicle owners.

Hungary has a 10 percent domestic reduction target for emissions from transport relative to projected transport emissions in 2020. Much of the emissions reduction is expected to be made through the renewables transport target. Other transport policies include: the improved integration of public transport systems; park and ride systems; the modernization of the transport fleet; and tolls on heavy vehicles. Existing measures in the transport sector are expected to reduce transport emissions by 7 percent relative to projected transport emissions in 2020. How the remaining 3 percent emissions reduction will be achieved remains unclear. Hopefully, the introduction of more stringent emission standards, and the EU-wide regulation on decreasing the GHG emissions (caps) of a producer's car fleet will help to close the gap.

Hungary is land-locked but can use the Danube River for some international shipping. Currently, there are no Hungarian flagged ships engaged in international shipping on the Danube River. Shipping on the Danube River is largely unscheduled and informal, over which Hungary has no specific jurisdiction. Historically, Hungary has used the Danube River for freight transportation and believes that an opportunity exists to use the river for freight transport, again with a view to reducing road freight emissions

Industrial sector. The focus of PaMs in the industrial sector is on improving energy efficiency through financial support programmes, energy audits, and voluntary programmes. Funding is available through financial assistance on a grant basis provided by the EU programme, Poland and Hungary: Assistance for Restructuring their Economies (PHARE). Funds have been set aside to increase renewable energy and reduce energy loss in energy carriers. Beneficiaries also include municipalities, private and municipality-owned companies. The technologies are mainly efficient street lighting, small-scale combined heat and power systems, improvements of production processes, and – to a lesser extent – projects involving renewable energies.

Financial incentives in the form of grants are also available under the efficient energy consumption instrument to reduce energy consumption in buildings and to modernize district heating and buildings for small- and medium-sized enterprises. Large energy consumers are required by law to employ an energy manager and to report on energy consumption and efforts being implemented to improve energy efficiency. Reporting of PaMs in the industrial sector could be improved by separating out the activities related to the non-industrial sector (e.g., improving the efficiency of street lighting) and wherever several PaMs target one activity (e.g., improving boiler efficiency).

3.3. Policies and measures in other sectors

Between the base year and 2008, GHG emissions from industrial processes (including solvent and other product use), agriculture, and waste decreased by 44.2 percent (14,013 Gg CO_2 eq), mainly driven by reductions in emissions from agriculture and industrial processes. The trend in GHG emissions from industrial processes (including solvents and other product use) showed a notable decrease of 54.0 percent (or 6,039 Gg CO_2 eq). The decrease in emissions from agriculture was of the same range, 49.8 percent (or 8,728 Gg CO_2 eq). In contrast, emissions from the waste sector increased by 25.3 percent (753 Gg CO_2 eq).

Industrial processes. The decrease in GHG emissions from the industrial processes sector (including solvents and other product use) between the base year and 2008 was mainly driven by reductions in economic activity and the closing down of some industrial facilities following Hungary's transition to a market economy. A joint implementation project also contributed to a reduction of N_2O emissions from nitric acid production by 1,423 Gg CO_2 eq between 2006 and 2008.

Agriculture. Between the base year and 2008, the decrease in GHG emissions from the agriculture sector was mainly driven by reductions in agriculture activity following Hungary's transition to a market economy (*Kovács-Székely* and *Szalai*, 2009). Total emission reductions due to agriculture measures were reported to be 1,244.56 Gg CO_2 eq by the year 2020; however, information on

the effect of agriculture policies was not provided separately for N_2O and CH_4 emissions. Most of the abatement in agricultural emissions was expected to come from reduced emissions of N_2O driven by the implementation of the EU nitrates directive. The focus of the implementation of this directive in Hungary is on improved farming practices.

Most of the reduction in agriculture emissions would be from N_2O from protein forage optimization and derived nitrogen (N) excretion reductions. The N excretion reductions are driven by EU directives and implemented through improved farming practices. PaMs were modeled jointly to correctly account for the overlap (or double counting) between policies.

Other PaMs in the agriculture sector focus on the modernization of farming systems, financial support for improved environmental practices, and afforestation on agricultural land.

LULUCF. The LULUCF sector was a net removal of 4,515 Gg CO_2 eq in Hungary in 2008, and the net GHG removal increased by 2,267 Gg CO_2 eq from the base year. The trend was mainly driven by afforestation policies. Information on policies to effect LULUCF activities under Article 3, paragraphs 3 and 4, of the Kyoto Protocol was not provided in the NC5.

Hungary has implemented a new Forestry Act of 2009 replacing the 1996 Forestry Act. The emphasis of forestry policy in Hungary is on the promotion of afforestation. In accordance with this policy, any deforestation (settlements and highways) must be compensated by an equivalent or greater amount of afforestation elsewhere. Deforestation for agriculture and over-thinning is not permitted. Forests must be allowed to regenerate to the most natural state possible wherever applicable. Until 2004, funding for afforestation was provided by the Hungarian Government but now the EU provides funding for most of the afforestation activities. Within the agri-environmental programme, 44,000 ha have been approved for afforestation, and the total area for afforestation under the programme (69,000 ha) appears feasible. The effects of PaMs in the forestry sector which were reported in the re-submission of the 2010 annual inventory on November 8, 2010 are as follows: removals in 2008 totaled 1.16 Mt CO_2 from afforestation and reforestation activities and 2.8 Mt CO_2 from forest management activities under Article 3, paragraph 4.

Waste management. Between the base year and 2008, GHG emissions from the waste sector increased by 25.3 percent (or 753 Gg CO_2 eq). Information on the effects of policies on the waste sector by gas has not been provided. The key policy to reduce waste and waste emissions is implemented in the context of the EU waste management directive and is under transposition into domestic legislation. The directive focuses on waste prevention and minimization, separation, reuse, and recycling. This includes the prevention of hazardous waste and the reduction of the amount of packaging.

The number of solid waste disposal sites across Hungary was approximately 2,600 in year 2002 of which only 1,000 sites operated. Between

2002 and 15 July 2009 their number decreased to 75, out of which the number of municipal solid waste disposal sites dropped from approximately 150 to 57. Closed sites are rehabilitated and checked to ensure that there is no wastewater leaching. Landfill sites are assessed for landfill gas capacity. Sites determined to have a positive economic value of landfill gas use landfill capture, otherwise the gases are flared. Whether the gas is captured or flared depends on the economic assessment. One waste management facility in Budapest has been retrofitted and the waste is burned for district heating and electricity generation.

4. Projections and the total effect of policies and measures, and supplementarity relating to the Kyoto Protocol mechanisms

4.1. Projections overview, methodology, and key assumptions

Hungary submitted three scenarios in its NC5, with 2005 as the starting year: (a) a 'without measures' (WOM) scenario, also called the 'baseline' scenario, which is presented as a theoretical trend line for comparison under the assumption of 'frozen technology' (no efficiency improvements in the power sector and energy demand, and no increase in the renewables share), while activities change; (b) a 'with measures' (WM) scenario (called 'with existing measures' in the NC5), which includes the effects of full implementation of existing and adopted measures, as well as the assumption that renewables targets will be met according to the base case in the Renewable Energy Strategy (RES) (an 11–13 percent renewables share of total primary energy consumption by 2020); and (c) a 'with additional measures' (WAM) scenario, which assumes that renewables targets will be met according to the more ambitious scenario defined in the RES (a 13 –15 percent renewables share of total primary energy consumption by 2020), and that other planned and possible new measures will be implemented, in addition to the ones already included in the WM scenario. This scenario also envisages that the EU ETS (covering power and heating plants, oil refineries, and production installations in industry) will continue until 2020 with a carbon price of EUR 24 –30/t, while the non-EU ETS sector (covering households, transport, waste, agriculture, and services) will achieve a 10 percent reduction in emissions.

The methodology used for preparing projections is well described in the NC5. Different approaches are used in different sectors. For most sectors (energy, waste, transport, industry, households, and the tertiary sector) the HUNMIT model is used. HUNMIT is a modeling framework that uses a bottom-up approach to estimate the demand of useful energy (i.e., energy for lighting and heating), rather than projecting energy demand based on fuel use. Input factors to the model are the population forecast, fuel prices, demand for electricity, and industrial and district heating. The model works out the most cost-effective fuel mix for the whole energy system. The HUNMIT model can

assess multiple policies simultaneously, thus ensuring that abatement estimates are not double counted. For LULUCF (forestry), a carbon accounting model called CASMOFOR is used, which takes into account the afforestation rate (total area in ha/year), site fertility, and species composition (slow- versus fast-growing species). For the agriculture sector, projections are based on work undertaken by the Agricultural Economics Research Institute (AERI), which uses several models: (1) the HUSIM model for developing major macro indicators; (2) the FARM-T model to analyze structural changes in agriculture; and (3) the MICROSIM model for farm-level forecasts on the farms which could become bankrupt.

The NC5 presents key assumptions on GDP growth, fuel prices, power production, emission factors for electricity generation, population, waste disposal, number of kilometres traveled by passenger cars, and the thermal efficiency of fossil plants for the years 2010, 2015, and 2020 in tabular format. Assumptions on the carbon price up to the year 2020 are also given in the text. Assumed changes in the activity rate in preparing projections are given in an appendix to the NC5 as five-year averages (2005–2010, 2010–2015, 2015–2020 and 2020–2025) for the following subcategories: different power plants in power generation and heat production; different subsectors in industry; housing stock and appliances used in households; building stock and appliances used in the tertiary sector; and waste management. Assumptions on GDP and population are similar to those in the NC4. Assumptions and, accordingly, projections do not take into account the recent economic crisis.

The sensitivity of the results using different input parameters is discussed in the NC5. The main parameters that have been considered are discount rates, energy prices, and CO_2 emission factors for electricity. The impact of a variation in these parameters on the projected GHG emissions is discussed in the NC5 only qualitatively, and no resulting numbers/uncertainty ranges are provided.

4.2. Results of projections

Hungary's base year emissions were fixed at 115.4 Mt CO_2 eq during the initial review. Hungary's quantified emission reduction commitment is 94 percent. This yields a target of 108.5 Mt CO_2 eq annual emissions for the Kyoto Protocol first commitment period (2008–2012). Hungary is on track to overreach this target by domestic efforts alone. In 2008, Hungary's total aggregated GHG emissions were 36.6 percent below base year levels, and 32.6 percent below the Kyoto Protocol target. The 'with measures' projections indicate that Hungary's GHG emissions will be 31.8 percent below the Kyoto Protocol target in 2010. Activities under Article 3, paragraphs 3 and 4, of the Kyoto Protocol are expected to provide further annual emission reductions and relevant removal units of 3.8 Mt CO_2 eq in 2010.

Table 4 summarises the projected emissions. Under the 'with measures' scenario, between the base year and 2010, CO_2 emissions are expected to decrease by 36.2 percent, CH_4 emissions by 17.3 percent, N_2O emissions by 47.6 percent, while F-gases are expected to increase by 203 percent.

Table 4. Summary of greenhouse gas emission projections for Hungary

	Greenhouse gas emissions (Tg CO_2 eq per year)	**Changes in relation to base year level (%)**	**Changes in relation to 1990 level (%)**
Inventory data 1990 [a]	97.365	–15.63	0.00
Inventory data 2008 [a]	73.139	–36.62	–24.88
Kyoto Protocol base year[b]	115.397	0.00	18.52
Kyoto Protocol target[b]	108.473	–6.00	11.41
'Without measures' projections for 2010[c]	85.915	–25.55	–11.76
'With measures' projections for 2010[c]	73.949	–35.92	–24.05
'With additional measures' projections for 2010[c]	73.489	–36.32	–24.52
'Without measures' projections for 2020[c]	100.865	–12.59	3.59
'With measures' projections for 2020[c]	73.276	–36.50	–24.74
'With additional measures' projections for 2020[c]	66.562	–42.32	–31.64

Sources: [a] Hungary's 2010 greenhouse gas (GHG) inventory submission; the emissions are without land use, land-use change and forestry (LULUCF).
[b] Based on the initial review report contained in document FCCC/IRR/2007/HUN.
[c] Hungary's 5th National Communication.

Beyond the first commitment period of the Kyoto Protocol, according to the 'with measures' projections, between 2005 and 2020 total CO_2 emissions will decrease by 3.8 percent, CH_4 emissions will increase by 3.7 percent, N_2O emissions will increase by 9.8 percent, and F-gases are expected to increase by 15.5 percent. Under the 'with measures' scenario, the relative contribution to the total GHG emissions (in CO_2 eq) in 2010 is 74 percent for CO_2, decreasing to 72 percent in 2020; 11 percent for CH_4 in 2010, increasing to 12 percent in 2020; 14 percent for N_2O in 2010, increasing to 15 percent in 2020; and 1 percent for F-gases in 2010 and 2020. The past and forecasted emission trends are shown in *Fig. 1.*

The effects of the recent global recession was considered on the short term by setting activity rate changes between 2005 and 2010 to a very low level (stagnation).

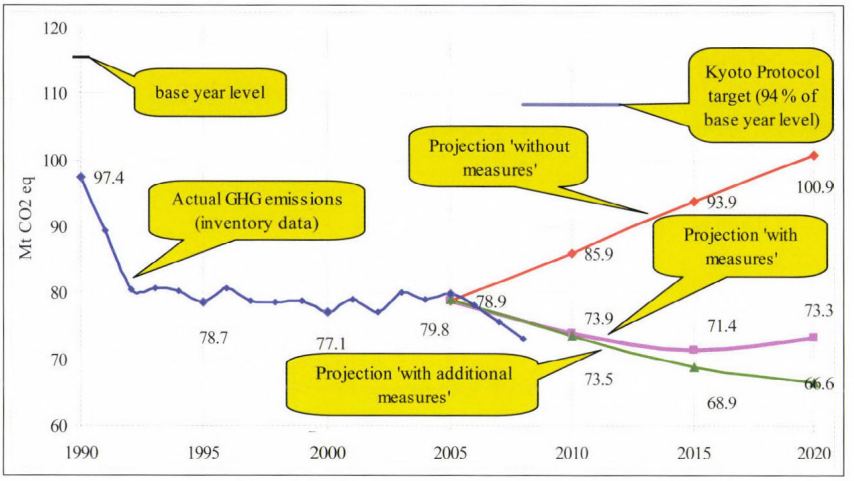

Sources: (1) Data for the years 1990–2008: Hungary's 2010 greenhouse gas inventory submission; the emissions are without land use, land-use change and forestry (LULUCF). (2) Data for the years 2005–2020: Hungary's 5th National Communication; the emissions are without LULUCF.

Fig. 1. Greenhouse gas emission projections.

Hungary has a conditional objective with regards to emission reductions up to 2020, defined in the NCCS: in the case of an EU emissions reduction target of 20 percent, Hungary would commit to a 16–25 percent reduction by 2020, compared to 1990 levels, and if the EU emissions reduction target is 30 percent, Hungary would commit to a 27–34 percent reduction by 2020. Based on Hungary's 1990 emissions figures in the latest NIR of 97.4 Mt CO_2 eq, these commitments would translate to an emissions target of 73.0–81.8 Mt CO_2 eq (for an EU target of –20 percent) or 64.3– 71.1 Mt CO_2 eq (for an EU target of –30 percent). The less ambitious commitment would be met under the current 'with measures' scenario, if all PaMs included in this scenario deliver emission reductions according to the expectations. The more ambitious commitment would be met under the 'with additional measures' scenario.

4.3. Total effect of policies and measures

In the NC5, Hungary presents the estimated and expected total effect of implemented and adopted PaMs in accordance with the 'with measures' definition, compared with a situation without such PaMs. Information is presented in terms of GHG emissions avoided or sequestered (on a CO_2 eq basis) in 2010, 2015, and 2020. It also presents relevant information on factors and activities for each sector for the years 2005–2020/2025.

Hungary reported that the total estimated effect of adopted and implemented PaMs is 10.7 Mt CO_2 eq in 2010, 18.2 Mt CO_2 eq in 2015, and

24.1 Mt CO_2 eq in 2020. According to the information reported in the NC5, the RES will deliver by far the largest emission reductions, followed by the EU ETS and the NEEAP. Within the NEEAP measures, PaMs in the industrial sector will deliver the largest emission reductions, followed by measures in the tertiary and household sectors. The most effective PaMs and drivers behind GHG emission reductions are described in Section 2. *Table 5* provides an overview of the total effect of PaMs as reported by Hungary.

Under the 'with measures' scenario, the power supply sector is the main source of emissions in 2005, contributing 27 percent of total GHG emissions, followed by industry with 18 percent. The contribution of the power supply sector to total GHG emissions decreases constantly until 2020, both in absolute and relative terms. In 2020, the power sector is expected to contribute 19 percent of total emissions. In contrast, transport emissions are constantly rising, and by 2020 the transport sector will replace power supply as the largest contributor of GHG emissions, with a 22 percent share of total GHG emissions. The relative contribution from the agriculture sector also increases constantly, from 12 percent in 2005 to 16 percent in 2020.

In absolute terms, under the 'with measures' scenario, the main reduction between 2005 and 2020 is expected to take place in the power supply sector, by 7.8 Mt CO_2 eq. Emissions in the transport sector are expected to increase in the same period by 3.6 Mt CO_2 eq, and in the agriculture sector by 2.0 Mt CO_2 eq. A reduction of 2.7 Mt CO_2 eq is expected in the industry sector between 2005 and 2020.

Table 5. Projected effects of planned, implemented, and adopted policies and measures in 2010 and 2020

Sector	Effect of implemented and adopted measures (Tg CO_2 eq)	Relative value (% of base year emissions)	Effect including planned measures (Tg CO_2 eq)	Relative value (% of base year emissions)	Effect of implemented and adopted measures (Tg CO_2 eq)	Relative value (% of base year emissions)	Effect including planned measures (Tg CO_2 eq)	Relative value (% of base year emissions)
	2010				2020			
NEEAP								
household	0.297	0.26	0.383	0.33	1.343	1.16	2.274	1.97
tertiary	0.375	0.32	0.424	0.37	1.504	1.30	2.210	1.92
industrial	0.502	0.44	0.693	0.60	2.236	1.94	3.996	3.46
transport	0.080	0.07	0.134	0.12	0.361	0.31	0.771	0.67
intersectoral	0.004	0.00	0.004	0.00	0.020	0.02	0.026	0.02
NEEAP total	1.258	1.09	1.638	1.42	5.464	4.73	9.277	8.04
RES	6.710	5.81	7.378	6.39	11.391	9.87	15.223	13.19
EU ETS	2.778	2.41	2.778	2.41	4.583	5.41	6.248	5.41
Total	**10.746**	**9.31**	**11.794**	**10.22**	**21.438**	**18.58**	**30.748**	**26.65**

Source: Hungary's 5th National Communication.

Abbreviations: EU ETS = European Union emissions trading scheme, NEEAP = National Energy Efficiency Action Plan, RES = Renewable Energy Strategy.

5. *Vulnerability assessment, climate change impacts, and adaptation measures*

In its NC5, Hungary has provided the required information on the expected impacts of climate change in the country and on adaptation options. Regional climate scenarios, using the REMO, NCAR RegCM, and ALADIN-Climate models for the Carpathian Basin, were provided for the years 2021–2040. The scenarios point to: a significant rise in temperature in all seasons; a decrease in the number of frost days; an increase in the number of days with heat alert; and an insignificant change in annual and seasonal precipitation. In June 2003, the Ministry for Environment and Water (KvVM) and the Hungarian Academy of Sciences (MTA) launched a joint research project entitled "Global climate changes, Hungarian impacts and responses", which recently became known as the VAHAVA project. Based on the modeling studies and activities as part of this project (*Bozó et al*, 2010a), Hungary's climate change impacts can generally be described as moderate, with an increasing probability of more severe impacts due to climate change. Agriculture, forestry, and human health are the sectors most likely to be affected (*Csete et al.*, 2012). Hungary's NCCS 2008–2025 sets out Hungary's long-term climate change policy direction. Adaptation is recognized as a key pillar of the policy, which will see its prominence increased in the revised NCCS due in 2011. *Table 6* summarizes the information on vulnerability and adaptation to climate change presented in the NC5.

The key vulnerabilities due to climate change for Hungary are attributed to water resource management (*Kovács et al.*, 2010). Increased surface temperature and heat, and a decrease in precipitation would have a direct impact on hydrology, leading to reduced water availability and the drying of soils. At the other extreme, increased frequency and intensity of precipitation can lead to floods, the inundation of low-lying areas, and hydromorphological changes (*Tanos et al.*, 2011). The NC5 did not demonstrate any rigorous assessments specific to Hungary; most information was adopted for the local situation. However, the VAHAVA study contained more specific examples which could have been included in the NC5. Such targeted information should be included in future national communications.

The NC5 recognizes the critical role of adaptation on a timely basis and examines the climate–security nexus in the critical areas of ecosystems, agriculture and forest management, infrastructure and water management. Particular issues arising out of the urban heat problem (i.e., the heat effect due to urbanization) are highlighted, given that Hungary's urban population is forecasted to rise to 80 percent of the total population in a few years. The importance of adaptation in the above areas is described, and possible adaptation measures to deal with the likely impacts of climate change are outlined. Many of the adaptation measures are generic responses to impacts as contained in the literature (*Szenteleki et al.*, 2012). There is scope for more targeted, localized

responses, which Hungary should include in its future national communications (*Kis-Kovács et al.*, 2011).

Table 6. Summary of information on vulnerability and adaptation to climate change

Vulnerable area	Examples/comments/adaptation measures reported
Agriculture and food security	*Vulnerability:* The vulnerability of the agriculture sector is estimated to be high *Adaptation:* The use of appropriate land use and cultivation, irrigation and relevant technologies are possible adaptation measures. Studies of the relationship between climatic variables and species and the agronomic characteristics of crops will underpin adaptation measures
Biodiversity and natural ecosystems	*Vulnerability:* Natural habitats and biodiversity are likely to be negatively impacted. The availability of water was recognized as a key driver. The social and economic services rely on healthy ecosystems *Adaptation:* More data and studies are needed to estimate specific climate change impacts on horticulture and other ecosystems
Drought	*Vulnerability:* The modelling results point to extremes of rainfall, with reduced amounts in some regions *Adaptation:* The use of technologies in specific sectors are possible adaptation measures
Forests	*Vulnerability:* Forests are also recognized as being vulnerable to water availability and temperature *Adaptation:* The use of technology and further studies on the behaviour of species in response to changes in climatic variables are suggested
Human health	*Vulnerability:* An increase in temperature would lead to an increase in the number of days with heat alert. This has implications on human health, especially among Hungary's ageing population *Adaptation:* No specific measures are mentioned
Infrastructure and economy	*Vulnerability:* This is recognized as a major security issue *Adaptation:* The need for further assessment of the effects of climate change on key infrastructure, such as roads, drainage and storage facilities, is recognized. The ability to respond to these challenges, through a risk-based approach, needs to be strengthened
Water resources	*Vulnerability:* This is a key sector that is vulnerable to the extreme situations of excess and reduced water availability as well as quality. It would affect many sectors, such as agriculture, forestry, health, and ecosystems *Adaptation:* The assessment and monitoring of water reserves, policies on water usage and flood control are possible adaptation measures

Vulnerability and impacts need to be based on solid scientific analysis and assessment. These in turn should form the basis of priority adaptation strategies and measures. Hungary should improve the linkages between the sections reporting on the scenarios, vulnerability, and adaptation in its future national communications.

6. Research and systematic observation

Hungary has provided information on its actions relating to research and systematic observation, mainly in relation to domestic activities. There is, however, a lack of details on international activities, including the World Climate Programme, the International Geosphere–Biosphere Programme (IGBP), the GCOS, and the IPCC. Hungary has not provided a summary of information on World Meteorological Organization (WMO) programmes and subprogrammes such as World Weather Watch (WWW), Global Atmosphere Watch (GAW), Global Observation System (GOS), GCOS, Global Ocean Observation System (GOOS), and Global Terrestrial Observing System (GTOS) activities. In addition, the NC5 does not reflect the action taken to support related capacity-building in developing countries. The lack of information in Hungary's NC5 on the observational networks, data management, QC, and data exchange is noticable. While this information was provided by the Hungarian Meteorological Service, Hungary should include this information explicitly in its future national communications.

The VAHAVA project, carried out by the Hungarian Academy of Sciences, provides the scientific and technical basis for the NCCS. The NCCP outlines a comprehensive list of research activities, including collaboration at the EU and international levels. The modeling work is carried out as a joint activity between the Hungarian Meteorological Service and the Department of Meteorology at Eötvös Loránd University (*Bozó*, 2011). The international research activities are currently limited to EU countries, and Hungary has not reported on any other international research collaboration.

Funding for climate change research stems mainly from EU sources, as part of the cooperation programme under the 7th Research Framework Programme. The National Office for Research and Technology also provides funds for climate change research under the Liveable and Sustainable Environment, and the Defence and Security Research subprogrammes. The national research efforts appear to be well coordinated and supported through the active participation of the Hungarian Academy of Sciences, the Hungarian Meteorological Service, and national universities and research institutions. As part of the VAHAVA project, the periodical *AGRO-21* has been developed, consisting of 18 volumes focusing on climate change and the required responses, covering almost all the main economic and social sectors, such as nature conservation, water management, agriculture, forestry, rural development, transport, energy, environmental health, settlements, and insurance. The largest positive result of this research project has been raising the awareness of the public to the importance of preparing for the adaptation to and mitigation of climate change and its impacts (*Bozó et al*, 2010b). However, Hungary has not reported on any initiatives to support capacity-building or research and development in developing countries.

The bulk of the observational activities are carried out by the Hungarian Meteorological Service and the Department of Meteorology at Eötvös Loránd University. Hungary, as a member of the European Organization for the Exploitation of Meteorological Satellites (EUMETSAT), participates in satellite observation networks. Hungarian institutions have also participated in several international research efforts on carbon balance projects such as CarboEurope-IP, Carbon-Pro, and COST Action 725. Hungary was also part of the Adam Project 2006–09, implemented by the University of East Anglia (United Kingdom of Great Britain and Northern Ireland) involving around 19 countries undertaking adaptation and mitigation projects.

6.1. Education, training, and public awareness

In the NC5, Hungary has provided information on its actions relating to education, training, and public awareness at three levels of action: environmental education; publicly available environmental education; and strengthening the role of the media in raising awareness. A comprehensive list of courses and programmes offered by Hungarian colleges and universities is provided in the NC5, which underlines the diversity of climate change related studies; collaborative programmes with institutions in Greece, Sweden, and the United Kingdom have been set up.

The NC5 outlined the governmental support for education programmes and training related to climate change. Various organizations and professional bodies such as the Energy Centre, the Hungarian Green Building Council, and the Association for Sustainable Economies carry out regular workshops and conferences on climate change and sustainable development. In its NC5, Hungary has not reported on any joint training programmes or capacity-building activities with developing countries. Such information should be present in future national communications.

A large and diverse range of activities to raise public awareness are highlighted in the NC5. These have been actively supported by non-governmental organizations (NGOs), churches, and business councils. The Hungarian Government organized a Climate Road Show in 2008 aimed at raising awareness of climate change throughout the country. A government-administered website – Liveable Environment (http://www.elhetokornyezet.hu)– is also dedicated to raising public awareness. Hungary used the opportunity provided through the EU-funded You Control Climate Change campaign to raise awareness about global climate change. International NGOs, such as Greenpeace and the World Wildlife Fund (WWF), have been active at global forums such as the Road to Copenhagen, and Earth Hour. Civil society in Hungary appears to be well organized and supported in its public awareness and advocacy campaigns. A survey conducted by the NGOs showed a high level of public awareness of climate change issues, although the behavioral change activities at the domestic level are often dictated by economic considerations.

7. *Conclusions and recommendations*

Hungary's emissions for 2008 were estimated to be 36.1 percent below its base year level excluding LULUCF and 38.9 percent below including LULUCF. Emissions decreases were driven by a downturn in the economy, fuel switching to less carbon-intensive fuels, and a restructuring of the economy.

Hungary presents GHG projections for the years 2010, 2015, and 2020, using 2005 as the starting point for the projections. Three scenarios are included: the baseline ('without measures') scenario; the 'with measures' scenario (called 'with existing measures' in the NC5); and the 'with additional measures' scenario. The projected reductions in GHG emissions under the baseline scenario, in relation to the base year, and under the 'with measures' and 'with additional measures' scenarios, are 25.6, 35.9, and 36.3 percent, respectively, for 2010. Thus, the projections indicate that Hungary can meet its Kyoto Protocol target (which is a 6 percent reduction), even under the baseline scenario with the domestic policies currently in place. Moreover, GHG emissions are not expected to exceed the Kyoto Protocol target even by 2020.

The National Climate Change Strategy 2008–2025 and the promotion of energy efficiency and renewable energy are among the most important PaMs in reducing GHG emissions. The benefits of the energy efficiency PaMs in Hungary appear to be high relative to the cost and could possibly occur under a 'business as usual' scenario. It is, therefore, important for Hungary to continue to re-evaluate the energy efficiency measures in place in order to ensure that the improvements would be additional to what could occur under 'business as usual', given that the benefits of the scheme are likely to diminish over time as the energy efficiency of the housing stock is improved.

Mitigating emissions from transport is the most challenging part of the overall mitigation strategy for Hungary. Under the PaMs currently in place, Hungary expects to reduce transport emissions by only 7 percent between 2005 and 2020. Additional PaMs need to be put in place in order to reach the national target of at least a 10 percent reduction in emissions from the transport sector. Further, options to support measures to achieve the renewable energy supply target in Hungary of 13 percent by 2020 need to be explored, given that no PaMs have been implemented yet to meet this target. The introduction of more stringent emission standards, and the EU-wide regulation on decreasing the GHG-emissions (caps) of a producer's car fleet will help to close the gap.

The key vulnerabilities are attributed to water resource management, which will be impacted by extremes of precipitation and temperature increase. Climate change impacts are expected to be visible in other sectors as well, including agriculture, forestry, biodiversity, and health. Various adaptation measures are explored as potential responses to these impacts.

Hungary has actions relating to research and systematic observation, and has effectively addressed its domestic activities. There are references to its

international activities, including the World Climate Programme, the IGBP, the GCOS, and the IPCC. Hungary contributes effectively to EU observation efforts and participates in a number of carbon monitoring projects. There is a growing emphasis on research activities on climate change and its impacts under the guidance of the Hungarian Academy of Sciences and various universities. There is also a substantial emphasis on integrating climate change education into formal programmes at the primary, secondary, and tertiary levels.

Several recommendations can be formulated related to the completeness and transparency of Hungary's reporting under the Convention and its Kyoto Protocol. The key recommendations are that, in its future national communications, Hungary includes information on:

a. The effects of PaMs on GHG emissions for all sectors and gases, especially for the agriculture, waste, and industrial processes sectors;
b. The steps undertaken to limit or reduce GHG emissions from aviation and marine bunkers;
c. The use of the mechanisms under Articles 6, 12 and 17 of the Kyoto Protocol and their supplementarity to domestic action.

It is recommended that Hungary undertakes a number of improvements regarding transparency and completeness of reporting as follows:

d. Provide a clearer link throughout the national communication between national circumstances, the GHG emissions profile and emission trends, and PaMs;
e. Provide more details on the climate change governance structure and explain how PaMs are implemented by municipal governments, in particular how central government can affect climate policies at the municipality levels given that municipalities have competencies over policy issues at those levels;
f. Provide more detailed information on how EU-directed policies are implemented in Hungary and their impact on emissions;
g. Provide a best estimate of the projected effects of the EU ETS in the PaMs chapter, and explain any overlap with existing PaMs;
h. Provide information on activities under Article 3, paragraphs 3 and 4, of the Kyoto Protocol;
i. Provide further information on its activities in the area of research, and data gathering, in particular on the collaboration with developing countries and other international agencies/organizations;
j. Provide further information on international activities relating to systematic observations, including GCOS activities;
k. Enhance the linkages between the sections on research, modeling, vulnerability assessments, and adaptation measures;

l. Provide further information on the minimization of adverse effects and impacts in accordance with Article 2, paragraph 3, and Article 3, paragraph 14, of the Kyoto Protocol;

m. Provide projections of the following indirect GHGs: carbon monoxide (CO), nitrogen oxides (NOX), non-methane volatile organic compounds (NMVOCs), and sulfur dioxide (SO2).

n. Provide strengths and weaknesses of modeling environments used for emission forecasting.

Acknowledgements—The authors would like to express their gratitude for the support of the TÁMOP-4.2.1.B-11/2/KMR-2011-0003 project titled "Az oktatás és kutatás színvonalának emelése a Szent István Egyetemen".

References

"Guidelines for the preparation of national communications by Parties included in Annex I to the Convention, Part II: UNFCCC reporting guidelines on national communications". FCCC/CP/1999/7. Available at <http://unfccc.int/resource/docs/cop5/07.pdf>.

"Guidelines for the preparation of national communications by Parties included in Annex I to the Convention, Part I: UNFCCC reporting guidelines on annual inventories". FCCC/CP/1999/7. Available at <http://unfccc.int/resource/docs/cop5/07.pdf>.

FCCC/SBI/2007/INF.6. Compilation and synthesis of fourth national communications. Available at <http://unfccc.int/resource/docs/2007/sbi/eng/inf06.pdf>.

FCCC/SBI/2007/INF.7. Compilation and synthesis of supplementary information incorporated in fourth national communications submitted in accordance with Article 7, paragraph 2, of the Kyoto Protocol. Available at <http://unfccc.int/resource/docs/2007/ sbi/eng/inf07.pdf>.

FCCC/ARR/2009/HUN. Report of the individual review of the greenhouse gas inventory of Hungary submitted in 2009. Available at <http://unfccc.int/national_reports/annex_i_ghg_inventories/national_inventories_submissions/items/4771.php>.

FCCC/IDR.4/HUN. Report on the in-depth review of the fourth national communication of Hungary. Available at <http://unfccc.int/resource/docs/2006/idr/hun04.pdf>.

4th national communication of Hungary. Available at <http://unfccc.int/resource/docs/natc/hunnc4.pdf>.

2009 GHG inventory submission of Hungary. Available at <http://unfccc.int/national_reports/annex_i_ghg_inventories/national_inventories_submissions/items/4771.php>.

2010 GHG inventory submission of Hungary. Available at <http://unfccc.int/national_reports/annex_i_ghg_inventories/national_inventories_submissions/items/5270.php>.

VAHAVA project (Change (VÁltozás) Impact (HAtás) Response (VÁlasz) – Joint scientific cooperation of the Hungarian Ministry for the Environment and Water (KvVM) and the Hungarian Academy of Sciences (MTA), 2003–2006.

National Climate Change Strategy (NCCS), 2008–2025, Ministry for the Environment and Water and the Hungarian Academy of Sciences.

Bozó, L., 2011: Hungarian National Report on IAMAS 2007–2010: Activities at the Hungarian Meteorological Service. *Acta Geodaetica et geopjysica Hungarica 46*, 215–231.

Bozó, L., Horváth, Á., Zsikla, Á., Hadvári, M., and *Kovács, A.,* 2010a: Szélsőséges meteorológiai helyzetek 2010. május-júniusban. *Klíma-21 Füzetek 16*, 7–15. (In Hungarian)

Bozó, L., Horváth, L., Láng, I., and *Vári, A.* (eds.), 2010b: *Környezeti Jövőkép – Környezet- és Klímabiztonság*. (Köztestületi Stratégiai Programok), Magyar Tudományos Akadémia, Budapest. (In Hungarian)

Csete, M. and *Horváth L.*, 2012: Sustainability and Green Development in Urban Policies and Strategies. *Appl. Ecol. Environ.Res. 10*, 185–194.

Kis-Kovács, G., Bozó, L., Lovas, K., Nagy, E., and *Tarczay, K.*, 2011: Adalékok az üvegház-hatású gázok antropogén kibocsátásának és elnyelésének vizsgálatához Magyarországon. In *Sebezhetőség és adaptáció, A reziliencia esélyei.* (eds.: *Tamás, P.* and *Bulla, M.*). MTA Szociológiai Kutatóintézet, Budapest, 305–314. (In Hungarian)

Kovács-Székely, I. and *Szalai, J.*, 2009: The impact of climate change on production conditions of Hungarian agriculture, especially on shallow groundwater supply.. *Proceedings of BBS*, ISBN 978-963-06-8171-1, 79–96.

Kovács, J., Kiszely-Peres, B., Szalai, J., and *Kovácsné Székely, I.*, 2010: Periodicity in shallow groundwater level fluctuation time series on the Trans-Tisza Region, Hungary. *Acta Geographica Ac Geologica Et Meteorologica Debrecina 4–5*, 65–70.

Szenteleki, K., Horváth, L., and *Ladányi, M.*, 2012: Climate Risk and Climate Analogies in Hungarian Viticulture. *International proceedings of chemical, biological and environmental engineering 28*, 250–254.

Tanos, P., Kovács, J., Kovácsné Székely, I., and *Hatvani, I.G.*, 2011: Exploratory data analysis on the Upper-Tisza section using single and multivariate data analysis methods. *Cent. Eur. Geol. 54*, 345–356.

IDŐJÁRÁS

Quarterly Journal of the Hungarian Meteorological Service
Vol. 116, No. 4, October–December 2012, pp. 323–335

Response of summer rainfalls in Pakistan to dust aerosols in an atmospheric general circulation model

Rashed Mahmood[1,2,3]* and **Shuanglin Li**[1]

[1]*Nansen-Zhu International Research Centre (NZC), Institute of Atmospheric Physics (IAP), 100029 Beijing China*

[2]*Graduate University of the Chinese Academy of Sciences (GUCAS), 100029 Beijing China*

[3]*Department of Meteorology, COMSATS Institute of Information Technology (CIIT), 44000 Islamabad Pakistan*

**Corresponding author E-mail: rashed@mail.iap.ac.cn*

(Manuscript received in final form August 29, 2012)

Abstract—Satellite data indicate that the dust concentration over Pakistan and its surrounding regions is substantially large especially in summer season when southwesterly winds actively bring additional dust (apart from local deserts) from eastern Africa and the Arabian Peninsula. To assess the potential response of summer rainfalls in Pakistan for dust concentrations, in this study we use an atmospheric general circulation model with prescribed sea surface temperatures and elucidate that the contribution of dust in modulating summer precipitation can be substantial with mainly positive responses over northern and southern Pakistan while negligibly small negative response over the central region. The anomalous results for dust aerosols in the model are calculated as the difference between two types of ensemble sensitive experiments with one ensemble simulation including dust while in the other ensemble the dust is removed over a selected domain. The maximum amount of enhanced rainfall is about 0.7 mm/day which is approximately 10% of the summer season rainfall in northern Pakistan. Such anomalous amplification in rainfall is realized through the advection of moist static energy into land regions of Pakistan as well as the additional supply of moisture from the Bay of Bengal and the Arabian Sea.

Key-words: dust aerosols, rainfall in Pakistan, south Asian monsoon, total ozone mapping spectrometer aerosol index (TOMS-AI), Arabian Sea

1. Introduction

Dust aerosols can play a significant role in modulating global and regional climates, primarily through absorbing and, to some extent, scattering of solar radiations (*Miller* and *Tegen*, 1998; *Andreae et al.*, 2005). The absorption of radiations in the atmosphere implicates changes in vertical profiles of atmospheric temperatures with heating in lower to middle troposphere while cooling near surface (*Hui et al.*, 2008). This reorganization of energy can modify the stability of the atmosphere, and thus, can potentially augment regional climate conditions (*Perlwitz* and *Miller*, 2010; *Hui et al.*, 2008). Therefore, understanding the role of dust aerosol in regional and global climate can be intriguing and has been one of the major focus points for research in climate science studies (e.g., *Tegen* and *Fung*, 1996; *Miller* and *Tegen*, 1998; *Miller et al.*, 2004; *Andreae et al.*, 2005; *Engelstaedter* and *Washington*, 2007; *Hui et al.*, 2008; *Perlwitz* and *Miller*, 2010).

Most of the dust aerosols instigate into the atmosphere through soil erosion driven by winds (*Miller et al.*, 2004). These aerosols can travel thousands of kilometers from their source regions depending on particle size and the prevailing atmospheric conditions (*Perlwitz* and *Miller*, 2010; *Engelstaedter* and *Washington*, 2007). Satellite data, such as total ozone mapping spectrometer (TOMS) aerosol index (AI) (*Torres et al.*, 1998; *Prospero et al.*, 2002), provides opportunities for visualizing large scale absorbing aerosol (mainly dust and black carbon) transport from vast deserts of Africa and Asia towards remote locations (*Fig. 1*). A considerable amount of dust is transported towards Arabian Sea and southern Pakistan through southwesterly boreal summer monsoonal winds (wind vectors in *Fig. 1*). In Pakistan, dust is not only transported from remote locations, but also the local deserts (such as Thar, Thal, and Cholistan) contribute to the total concentrations. Thus, the potential influence of dust aerosols on regional climate of Pakistan can be expected given the large concentrations therein and surrounding areas as well. These considerate motivate the present study in which we used an atmospheric general circulation model (AM2) from the National Oceanic and Atmospheric Administration's (NOAA) Geophysical Fluid Dynamics Laboratory (GFDL) (Anderson et al., 2004), to investigate the contribution of dust aerosols in regional summer climate of Pakistan.

2. Model basics

The AM2 model has been used frequently in many previous studies (e.g., *Anderson et al.*, 2004; *Randles* and *Ramaswamy*, 2008, 2010; *Ming* and *Ramaswamy*, 2009, 2011; *Mahmood* and *Li*, 2011, 2012; *Bollasina et al.*, 2011), and thus, it needs not to be fully discussed here in order to avoid repetition. Therefore, only the most important components that are helpful in understating

the results of current study would be discussed. For detailed and comprehensive information on physical parameterizations, readers may consult *Anderson et al.* (2004). The model is based on the finite-volume dynamical core of *Lin* (2004), with horizontal resolution of 2° latitude × 2.5° longitude and 24 levels in vertical with top at about 3 hPa. The model incorporates the scheme of *Freidenreich* and *Ramaswamy* (1999) for shortwave radiation algorithms with some modifications made by *Anderson et al.* (2004) to optimize computational efficiency. This scheme considers absorption by several greenhouse gases along with molecular scattering, and absorption and scattering by clouds and aerosols. The longwave radiation scheme is based on an improved version of simplified exchange approximation (*Schwarzkopf* and *Ramaswamy*, 1999) where aerosols and clouds are treated as absorbers, while the scheme considers absorption and emissions from several greenhouse gases.

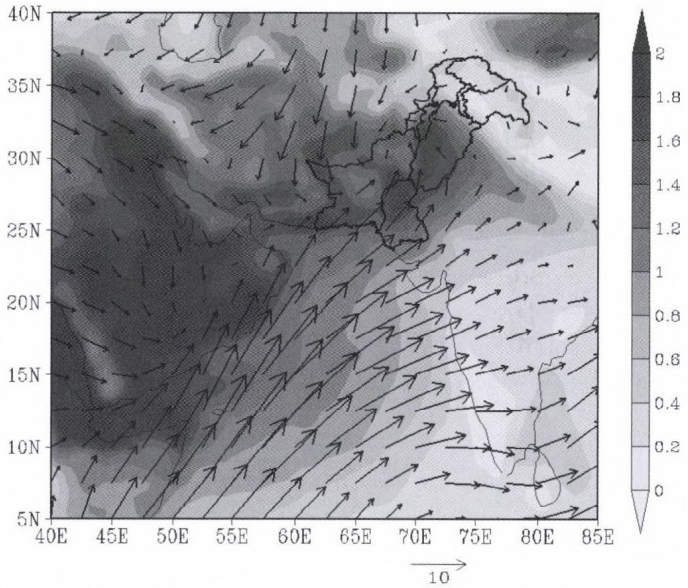

Fig. 1. TOMS-AI climatology (1979-1992) for Jun-Jul-Aug (JJA): climatological winds at 1000 hPa level (1961-1990) for the month of July from NCEP data. Reference wind vector is shown below the figure. Bold black polygons represent geographical location of Pakistan.

The aerosol climatologies, used as inputs in AM2, are calculated offline using a separate chemical transport model known as Model of Ozone and Related Chemical Tracers (MOZART) Version 2 (*Horowitz et al.*, 2003), which is driven by meteorological parameters. The dust aerosol climatology is

simulated in MOZART with meteorological parameters obtained from NCEP/NCAR reanalysis (*Kalnay et al.*, 1996), and dust sources specified from *Ginoux et al.* (2001).

Note that dust is assumed to be of natural origin and kept constant throughout the simulation period with climatological seasonal cycle in AM2 model (*Ginoux et al.*, 2006), therefore, our study is not concerned with "climate change" phenomenon as studied for post/pre industrial simulations in case of anthropogenic aerosol induced radiative forcing. Instead, this study is designed to evaluate the possible contribution of dust aerosols to the "routine" summer climate of Pakistan.

Two kinds of ensemble simulations (with each ensemble having five members) were performed by including/excluding dust in simulations. In the first experiment (i.e., control ensemble), the dust is included in all five simulations of the ensemble, while in the second experiment (i.e., sensitive experiment), the dust over a regional domain comprising eastern Africa and Asia (i.e. 0°-50°N, 25°E-130°E) is removed from simulations. The sea surface temperatures are prescribed according to the observed seasonal cycles. The multiple members of each ensemble were designed with similar characteristics except a slight change in their initial times. The model is integrated for 21 years starting from January 1980 to December 2000. The influence of dust on climate is isolated here by subtracting the sensitive experiment from control experiment (i.e. control-sensitive) for the last 20 years of model simulations.

3. Results and discussions

Fig. 2 shows column burden of dust for summer season. Comparing with *Fig. 1*, the spatial features of model simulated dust burden appears to be qualitatively in agreement with TOMS-AI. For example, the largest burdens over eastern and southern Arabian Peninsula and southern Pakistan correspond well with strongest AI values. Similarly, the dust from Taklamakan desert in western China is well captured by the model. However, the regions south of Himalayan Mountains show little correspondence with TOMS-AI. This is because in this study we only show the burdens for dust aerosols, while the TOMS-AI product includes contributions both from dust and black carbon. The later has high concentration near Himalayan Mountains (*Sahu et al.*, 2008). Therefore, the dust simulation in model can be considered reasonable, though the model biases are expected in common with many previous modeling studies (*Ginoux et al.*, 2006). Important to note is the extension of dust from Middle East and Arabian Peninsula towards southern Pakistan both in summer and spring seasons (spring season is not shown here), which can influence the behavior of summer monsoons in Pakistan as discussed next in this section.

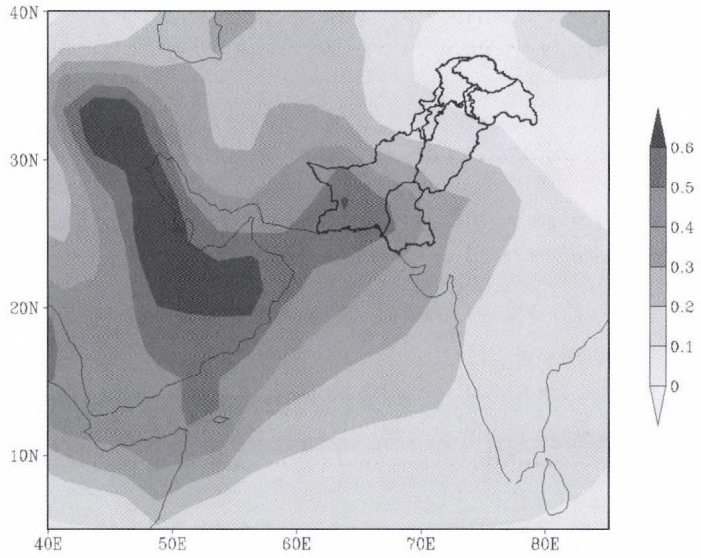

Fig. 2. Modeled column burden of dust aerosols for JJA. Unit: g/m^2

A substantial increase in clear sky shortwave radiative heating induced by dust over the longitudes of Pakistan can be seen visually in *Fig. 3*. The maximum heating region (about 0.5 K/day) lies between 900 and 800 hPa levels, while relatively less heating appear near the surface which is in agreement with previous conclusions that the dust aerosols absorb solar radiations in the lower troposphere, and hence, reduce the amounts reaching the surface (*Miller* and *Tegen*, 1998). Further, consistently with dust burdens, the heating is strongest over southern regions while less prominent near northern areas. Despite, even for the northern part, the magnitude is considerable with values reaching up to 0.35 K/day. Since the dust absorbs radiations in the lower troposphere, the anomalous changes in near surface air temperature over most of the highest dust concentration regions is negative (*Fig. 4*). The statistically significant (at 90% confidence level) negative temperature anomalies prevail over the maximum dust loading regions, i.e., southern Arabian Peninsula and Pakistan, while positive responses appear over China, especially the Tibetan Plateau, where dust loading were assumed to be small in the model (*Fig. 2*). Similarly, in most parts of the central Asian region the temperature changes are negative but statistically insignificant. These temperature changes are in line with the proposed mechanisms in that dust absorbs solar radiations in the atmosphere leaving fewer radiations reaching the surface (*Miller* and *Tegen*, 1998). However, some exceptions also exist, e.g., Taklamakan desert (about ~40N in western China) where small positive but less significant anomalies are found, although dust concentration is considerable in this region (*Figs. 1* and *2*). This implies that the strong cooling, especially over Pakistan with maximum values reaching up

to –0.7 K, may have been exaggerated by circulation changes such as horizontal and vertical dry advection of cooler air akin to elevated heat pump theorem proposed by *Lau et al.* (2006), however model biases, of course, may persist and cannot be ruled out for such anomalous changes.

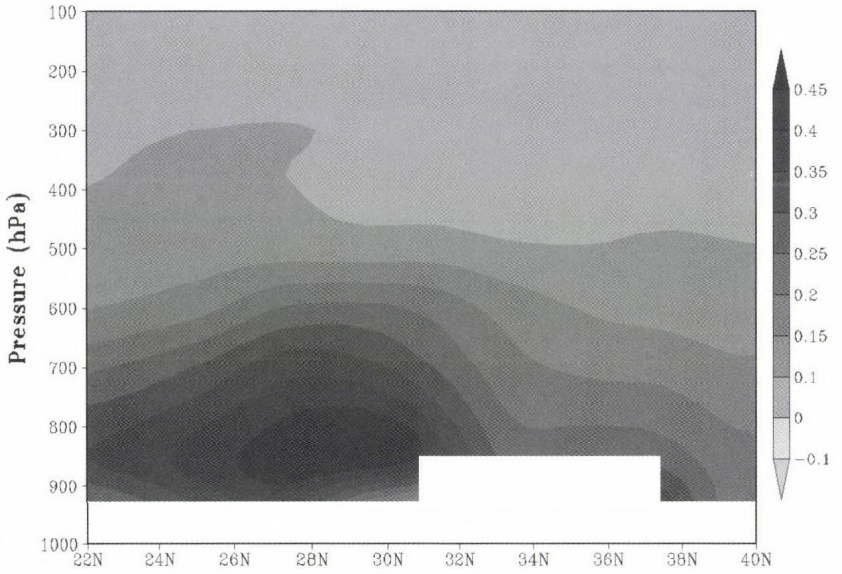

Fig. 3. Vertical cross section of clear-sky shortwave heating anomaly longitudinally averaged over Pakistan (60°E-75°E). White color is caused by the elevated topography. Unit: K/day

More important for the major considerate of the current study are changes in precipitation and circulation associated with dust aerosol (*Figs. 5, 6* and *7*) along with possible potential mechanisms as shown in *Fig. 8*. *Fig. 5* represents the anomalous precipitation changes over Pakistan. Significant positive rainfalls can be seen over the northern part of the country, especially over northern Punjab and parts of Azad Kashmir and Khyber Pakhtunkhwa provinces (which is approximately the climatologically mean location of summer rainfalls in Pakistan). Similarly, changes in rainfall are also significant over lower Sindh and Balochistan provinces, especially in coastal areas with maximum values approaching 0.7 mm/day, while negligibly small negative response occur over the central regions. This shows that, on average, the dust aerosols can induce a surplus of 10% to the seasonal rainfalls in Pakistan, where the observed summer season rainfall rate is about 7 mm/day (*Webster et al.*, 2011). Thus, the dust aerosols can have a significant contribution to the overall behavior of summer monsoon rainfalls in Pakistan.

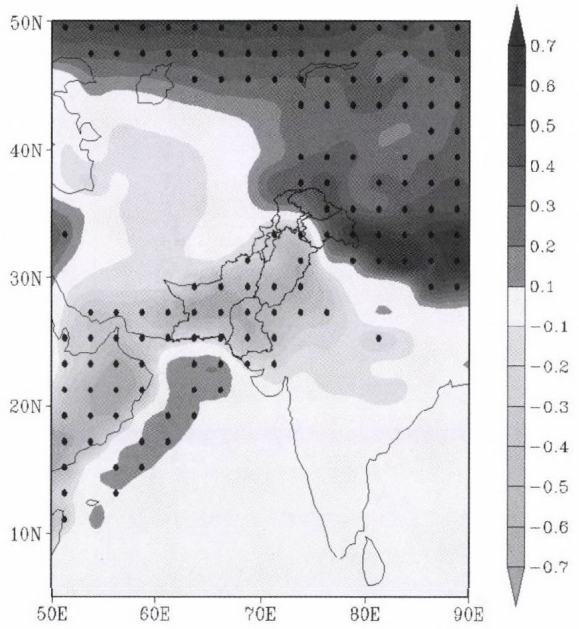

Fig. 4. Anomalous changes in near surface temperature (at 2m). Black dots represent the grid point values which are statistically significant at 90% confidence level. Unit: K.

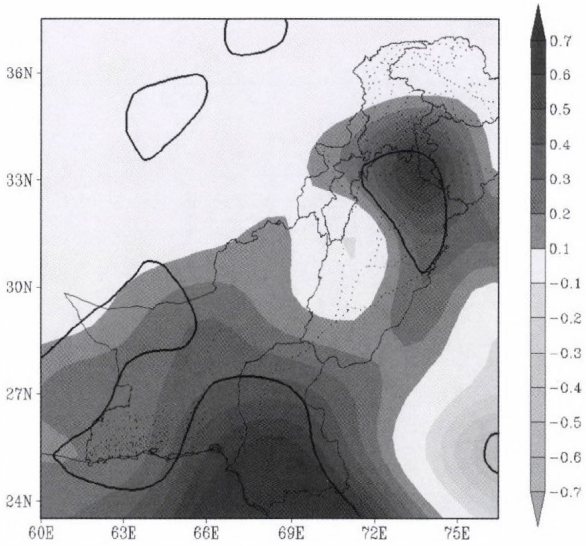

Fig. 5. Anomalous changes in precipitation (unit: mm/day). Thick black contour represents the values which are statistically significant at 90% confidence level. Thin dotted lines represent the Indus River and its major tributaries.

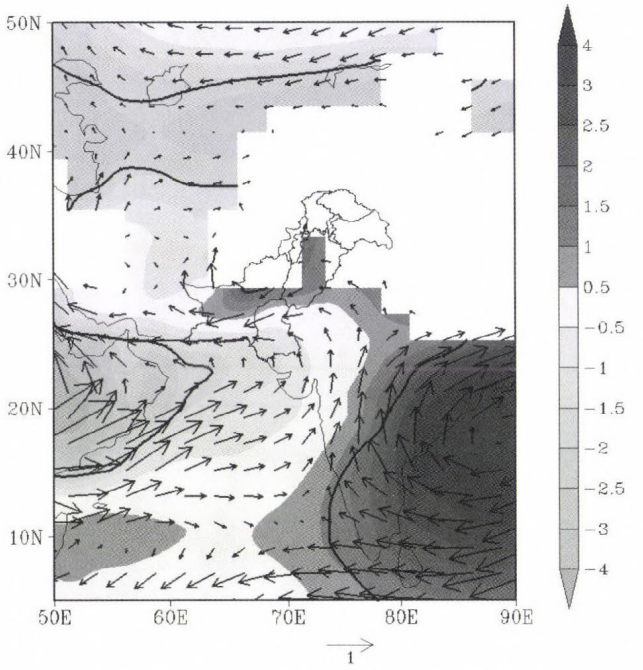

Fig. 6: Circulation anomalies at 850 hPa level; shading represents geopotential height (unit: gpm) and vectors represent wind (unit: m/s). Thick black contour represents height values which are statistical significant at 90% confidence level. White regions are caused by the elevated topography.

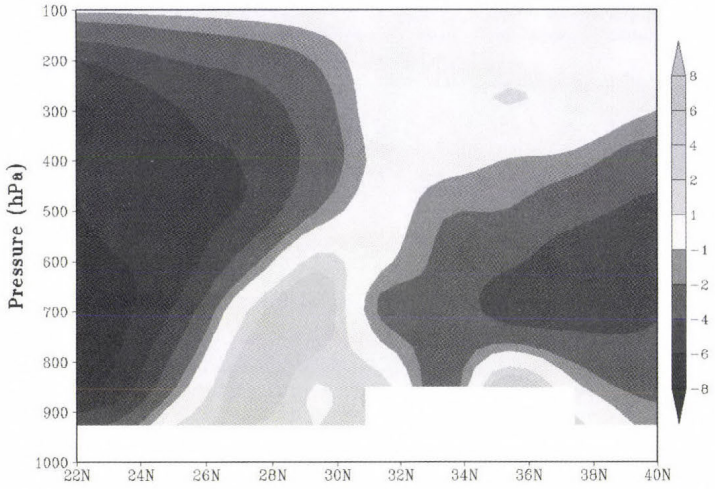

Fig. 7: Anomalous changes in vertical pressure velocity averaged over Pakistan (60°E-75°E) (negative values represent ascent). Unit: 10^{-3} Pa/s..

The corresponding changes in near surface (at 850 hPa level) geopotential height and winds are shown in *Fig. 6*. Strong dipole-like height anomalies prevail in northern Indian Ocean with significantly positive response over the Bay of Bengal and an extended low over Arabian Sea including southern Pakistan. Significant negative height anomalies also appear over central Asia and China. This distribution of height anomalies, especially stronger high pressure over Bay of Bengal, disperses moist winds from Bay of Bengal and also the Arabian Sea towards Pakistan as shown by the vectors in *Fig. 6*. The most favorable dynamics for enhanced rainfall in Pakistan in this case can be attributed to the strong anticyclonic circulations over Bay of Bengal which enhances the advection of anomalous winds with magnitudes up to 1 m/s towards northern Pakistan. Interestingly, for central Pakistan, where the rainfall response is negative, there exists a small positive height center which appears to deflect wind towards southern Pakistan implying further the consistency between precipitation and circulation anomalies.

The tri-polar precipitation anomalies over Pakistan (i.e., wetness over north/south regions and small dryness over central areas) can further be explored by analyzing the vertical velocity as shown in *Fig. 7*. Two ascending branches of anomalous vertical velocity can be seen near the coastal area (the stronger one), and the northern part implying strong convective activity taking place in these regions. These ascending motions are accompanied by a small descending branch in central Pakistan implying small dryness in this region (*Fig. 5*).

Wang et al. (2009) highlighted the importance of perturbation in moist static energy as a response to anthropogenic aerosol forcing, and argued that the changes in sub-cloud layer moist static energy can represent not only the northward migration of south Asian monsoons but also the strength of convection during the monsoon season. To see whether similar interpretations can be made for the current simulations, we calculated vertically integrated (1000–100 hPa) moist static energy (VMSE for short) as shown in *Fig. 8a*. Consistent with *Wang et al.* (2009), the VMSE is enhanced over Pakistan with a clear extension towards northern areas. The strongest anomaly in VMSE is, of course, near the southern moisture source region that is the northern Arabian Sea.

Finally, we calculated vertically integrated moisture flux (*Zhu* and *Newell*, 1998) to assess further the dust induced wet conditions in Pakistan (*Fig. 8b*). As shown by the figure, the moisture supply is enhanced towards Pakistan from three source regions, namely Bay of Bengal, eastern Arabian Sea, and the Persian Gulf. The strongest moisture flux is from Bay of Bengal and eastern Arabian Sea that travels along the foothills of Himalayas and finally converges over Pakistan.

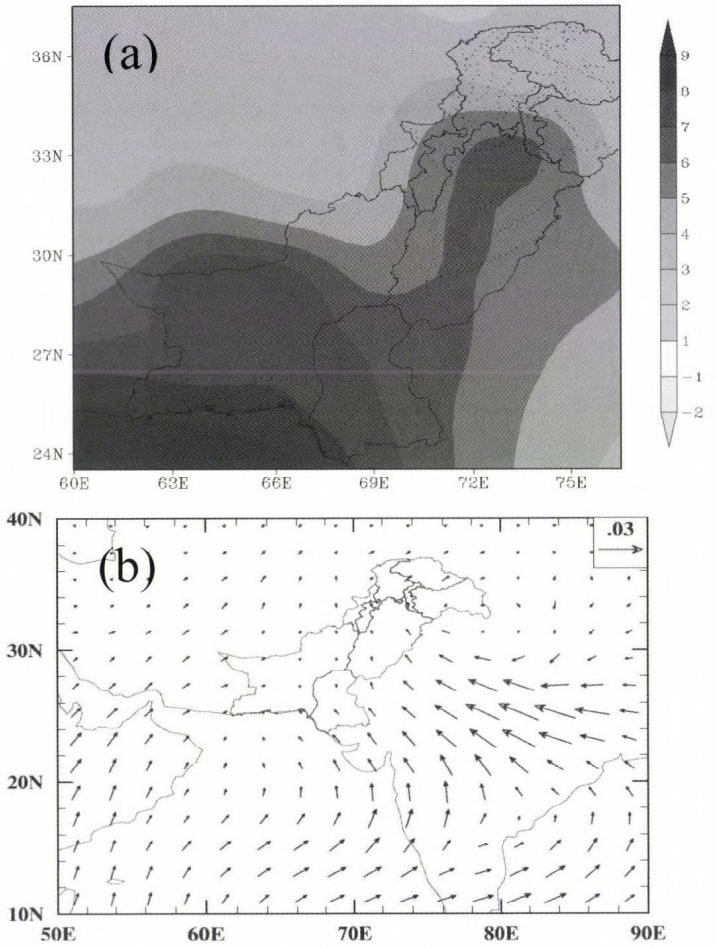

Fig. 8. Vertically integrated (1000-100 hPa) anomalous changes in (a) moist static energy (unit: 10^3 kJ/kg) and (b) moisture transport (unit: kg/ms). Reference vector for moisture transport is shown in upper right corner of (b).

4. Summary and remarks

In this study we investigate, using an atmospheric general circulation model AM2, the potential influence of Afro-Asian dust on regional summer climate of Pakistan. Two sets of ensemble simulations with and without dust aerosols were carried out to isolate the possible influence. Significant enhancement of rainfall over Pakistan was seen with maximum amount of anomalous rainfall reaching up to 0.7 mm/day. These modeled changes in precipitation are about 10% of the total observed summer rainfall in northern Pakistan (*Webster et al.*, 2011). The

anomalous circulation pattern show that a strong high over Bay of Bengal and a low pressure over the Arabian Peninsula/northern Arabian Sea including central Asia force the moister lower level winds towards northern Pakistan, some of which is deflected back to the southern coastal region and Arabian Sea.

The strong advection of moisture from the Arabian Sea and Bay of Bengal is further confirmed by the anomalous vertically integrated moisture transport towards Pakistan. Furthermore, the dust induced anomalous response was also observed by changes in VMSE which appeared to extend from northern Arabian Sea towards northern Pakistan. *Wang et al.* (2009) also found similar changes in (lower tropospheric) moist static energy over land regions of northwest subcontinent for anthropogenic aerosols using a different general circulation model. Thus, the collective affect of natural (e.g., dust) and anthropogenic aerosols may further exacerbate the above discussed rainfalls patterns. However, to explore the combined effects of natural plus anthropogenic aerosols on summer climate in Pakistan is beyond the scope of this study.

Further caveats of the study are the prescribed SSTs and missing indirect aerosol affects. Similarly, ground based observations of dust emission, transport, and overall concentrations in Pakistan are unfortunately not available. Thus, though the results from model simulations can be valuable, especially for studying aerosol influence on climate for which models are the primary diagnostic tools, they still need to be confirmed by ground based observations to make concrete conclusions. That the model results indicate significant change in circulations and precipitation over Pakistan in response to dust aerosols, which implies that we need to establish a network of ground based dust observations to fully grasp the interaction between strong dust concentrations and the relevant climate response in Pakistan. Therefore, further research is warranted, especially using ground based observations and multi-model simulations, to make conclusions more solid.

Acknowledgements—This study was supported by the Knowledge Innovation Program of the Chinese Academy of Sciences (Grant No. KZCX2-YW-Q11-03). The TOMS level 2 and 3 data sets are processed by NASA/Goddard Space Flight Center's Ozone Processing Team (OPT), we thankfully acknowledge them for making the data sets publically available.

References

Anderson, J.L., Balaji, V., Broccoli A.J., Cooke, W.F., Delworth, T.L., Dixon, K.W., Donner, L.J., Dunne, K.A., Freidenreich, S.M., Garner, S.T., Gudgel, R.G., Gordon, C.T., Held, I.M., Hemler, R.S., Horowitz, L.W., Klein, S.A., Knutson, T.R., Kushner, P.J., Langenhost, A.R., Lau, N.-C., Liang, Z., Malyshev, S.L., Milly, P.C.D., Nath, M.J., Ploshay, J.J., Ramaswamy, V., Schwarzkopf, M.D., Shevliakova, E., Sirutis, J.J., Soden, B.J., Stern, W.F., Thompson, L.A., Wilson, R.J., Wittenberg, A.T., and *Wyman, B.L.,* 2004: The new global atmosphere and land model AM2-LM2: Evaluation with prescribed SST simulations. *J. Climate 17*, 4641–4673.

Andreae, M.O., Jones, C.D. and *Cox, P.M.,* 2005: Strong present-day aerosol cooling implies a hot future. *Nature 435*, 1187–1190.

Bollasina, M.A., Ming, Y. and *Ramaswamy, V.,* 2011: Anthropogenic aerosols and the weakening of the south Asian summer monsoon. *Science 334*, 502–505.

Engelstaedter, S., and *Washington, R.,* 2007: Atmospheric controls on the annual cycle of North African dust. *J. Geophys. Res. 112*, D03103.

Freidenreich, S.M., and *V. Ramaswamy*, 1999: A new multiple-band solar radiative parameterization for general circulation models, *J. Geophys. Res. 104*, 31389–31409.

Ginoux, P., Chin, M., Tegan, I., Prospero, J.M., Holben, B., Dubovik, O., and *Lin, S.-J.,* 2001: Sources and distribution of dust aerosols simulated with GOCART model, *J. Geophys. Res. 106*, 20255–20273.

Ginoux, P., Horowitz, L.W., Ramaswamy, V., Geogdzhayev, I.V., Holben, B.N., Stenchikov, G., and *Tie, X.,* 2006: Evaluation of aerosol distribution and optical depth in the Geophysical Fluid Dynamics Laboratory coupled model CM2.1 for present climate. *J. Geophys. Res. 111*, D22210.

Horowitz, L.W., Walters, S., Mauzerall, D.L., Emmons, L.K., Rasch, P.J., Granier, C., Tie, X., Lamarque, J.-F., Schultz, M.G., Tyndall, G.S., Orlando, J.J., and *Brasseur, G.P.,* 2003: A global simulation of tropospheric ozone and related tracers: Description and evaluation of MOZART, version 2. *J. Geophys. Res. 108 (D24)*, 4784.

Hui, W.J., Cook, B.I., Ravi, S., Fuentes J.D., and *D'Odorico, P.,* 2008: Dust-rainfall feedbacks in the West African Sahel. *Water Resour. Res. 44*, W05202.

Kalnay, E., Kanamitsu, M.,Kistler, R., Collins, W., Deaven, D., Gandin, L., Iredell, M., Saha, S., White, G., Woollen, G., Zhu, Y., Chelliah, M., Ebisuzaki, W., Higgins, W., Janowiak, J., Mo, K.C., Ropelewski, C., Wang, J., Leetma, A., Reynolds, R., Jenne, R., and *Joseph, D.,* 1996: The NCEP/NCAR 40-year reanalysis project, *Bull. Amer. Meteor. Soc. 77*, 437–470.

Lau, K., Kim, M.K. and *Kim, K.M.,* 2006: Asian summer monsoon anomalies induced by aerosol direct forcing: the role of the Tibetan Plateau. *Clim. Dynam. 26*, 855–864.

Lin, S-J., 2004: A ''vertically Lagrangian'' finite-volume dynamical core for global models. *Mon. Weather Rev. 132*, 2293–2307.

Mahmood, R., and *Li, S.,* 2011: Modeled influence of East Asian black carbon on Inter-decadal shifts in East China summer rainfall. *Atmos. Oceanic Sci. Lett. 4*, 349–355.

Mahmood, R., and *Li, S.*, 2012: Delay in the onset of south Asian summer monsoon induced by local black carbon in an AGCM. *Theor. Appl. Climatol.* DOI 10.1007/s00704-012-0681-3.

Miller, R.L., and *Tegen, I.,* 1998: Climate response to soil dust aerosols, *J. Climate 11*, 3247–3267.

Miller, R.L., Tegen, I., and *Perlwitz, J.,* 2004: Surface radiative forcing by soil dust aerosols and the hydrologic cycle. *J. Geophys. Res. 109*, D04203.

Ming, Y., and *Ramaswamy, V.,* 2009: Nonlinear climate and hydrological responses to aerosol effects. *J. Climate 22*, 1329–1339.

Ming, Y., and *Ramaswamy, V.,* 2011: A model based investigation of aerosol-induced changes in tropical circulation. *J. Climate 24*, 5125–5133.

Perlwitz, J., and *Miller, R.L.,* 2010: Cloud cover increase with increasing aerosol absorptivity: A counterexample to the conventional semidirect aerosol effect. *J. Geophys. Res. 115*, D08203.

Prospero, J.M., Ginoux, P., Torres, O., Nicholson, S.E., and *Gill, T.E.,* 2002: Environmental characterization of global sources of atmospheric soil dust identified with the Nimbus 7 Total Ozone Mapping Spectrometer (TOMS) absorbing aerosol products. *Rev. Geophys. 40*, 1002.

Randles, C.A., and *Ramaswamy, V.,* 2008: Absorbing aerosols over Asia: A Geophysical Fluid Dynamics Laboratory general circulation model sensitivity study of model response to aerosol optical depth and aerosol absorption. *J. Geophys. Res. 113*, D21203.

Randles, C.A., and *Ramaswamy, V.,* 2010: Direct and semi-direct impacts of absorbing biomass burning aerosol on the climate of southern Africa: a Geophysical Fluid Dynamics Laboratory GCM sensitivity study.*Atmos. Chem. Phys. 10*, 9819–9831.

Sahu, S.K., Beig, G. and *Sharma, C.,* 2008: Decadal growth of black carbon emissions in India. *Geophys. Res. Lett. 35*, L02807.

Schwarzkopf, M.D., and *Ramaswamy, V.,* 1999: Radiative effects of CH4, N2O, halocarbons and the foreign-broadened H2O continuum: A GCM experiment. *J. Geophys. Res. 104*, 9467–9488.

Tegen, I., Lacis, A.A. and *Fung, I.,* 1996: The influence on climate forcing of mineral aerosols from disturbed soils, *Nature 308*, 419–422.

Torres, O., Bhartia, P.K., Herman, J.R., Ahmad, Z., and *Geason, J.,* 1998: Derivation of aerosol properties from satellite measurements of backscattered ultraviolet radiation: Theoretical bases. *J. Geophys. Res. 103(D14)*, 17099–17110.

Wang, C., Kim, D., Ekman, A.M.L., Barth, M.C., and *Rasch, P.J.,* 2009: Impact of anthropogenic aerosols on Indian summer monsoon. *Geophys. Res. Lett. 36*, L21704.

Webster, P.J., Toma, V.E. and *Kim, H.-M.,* 2011: Were the 2010 Pakistan floods predictable?. *Geophys. Res. Lett. 38*, L04806.

Zhu, Y. and *Newell, R.E.,* 1998: A proposed algorithm for moisture fluxes from atmospheric rivers, *Mon. Weather Rev. 126*, 725–735.

IDŐJÁRÁS

VOLUME 116 * 2012

BUDAPEST, HUNGARY

AUTHOR INDEX

TABLE OF CONTENTS

I. Papers

II. Book review

SUBJECT INDEX

T

U

V

W

X

Y

INSTRUCTIONS TO AUTHORS OF *IDŐJÁRÁS*

The purpose of the journal is to publish papers in any field of meteorology and atmosphere related scientific areas. These may be

- research papers on new results of scientific investigations,
- critical review articles summarizing the current state of art of a certain topic,
- short contributions dealing with a particular question.

Some issues contain "News" and "Book review", therefore, such contributions are also welcome. The papers must be in American English and should be checked by a native speaker if necessary.

Authors are requested to send their manuscripts to

Editor-in Chief of IDŐJÁRÁS
P.O. Box 38, H-1525 Budapest, Hungary
E-mail: journal.idojaras@met.hu

including all illustrations. MS Word format is preferred in electronic submission. Papers will then be reviewed normally by two independent referees, who remain unidentified for the author(s). The Editor-in-Chief will inform the author(s) whether or not the paper is acceptable for publication, and what modifications, if any, are necessary.

Please, follow the order given below when typing manuscripts.

Title page: should consist of the title, the name(s) of the author(s), their affiliation(s) including full postal and e-mail address(es). In case of more than one author, the corresponding author must be identified.

Abstract: should contain the purpose, the applied data and methods as well as the basic conclusion(s) of the paper.

Key-words: must be included (from 5 to 10) to help to classify the topic.

Text: has to be typed in single spacing on an A4 size paper using 14 pt Times New Roman font if possible. Use of S.I. units are expected, and the use of negative exponent is preferred to fractional sign. Mathematical formulae are expected to be as simple as possible and numbered in parentheses at the right margin.

All publications cited in the text should be presented in the *list of references*, arranged in alphabetical order. For an article: name(s) of author(s) in Italics, year, title of article, name of journal, volume, number (the latter two in Italics) and pages. E.g., *Nathan, K.K.,* 1986: A note on the relationship between photo-synthetically active radiation and cloud amount. *Időjárás 90,* 10-13. For a book: name(s) of author(s), year, title of the book (all in Italics except the year), publisher and place of publication. E.g., *Junge, C.E.,* 1963: *Air Chemistry and Radioactivity.* Academic Press, New York and London. Reference in the text should contain the name(s) of the author(s) in Italics and year of publication. E.g., in the case of one author: *Miller* (1989); in the case of two authors: *Gamov* and *Cleveland* (1973); and if there are more than two authors: *Smith et al.* (1990). If the name of the author cannot be fitted into the text: *(Miller,* 1989); etc. When referring papers published in the same year by the same author, letters a, b, c, etc. should follow the year of publication.

Tables should be marked by Arabic numbers and printed in separate sheets with their numbers and legends given below them. Avoid too lengthy or complicated tables, or tables duplicating results given in other form in the manuscript (e.g., graphs).

Figures should also be marked with Arabic numbers and printed in black and white or color (under special arrangement) in separate sheets with their numbers and captions given below them. JPG, TIF, GIF, BMP or PNG formats should be used for electronic artwork submission.

Reprints: authors receive 30 reprints free of charge. Additional reprints may be ordered at the authors' expense when sending back the proofs to the Editorial Office.

More information for authors is available: journal.idojaras@met.hu

Published by the Hungarian Meteorological Service

Budapest, Hungary

INDEX 26 361

HU ISSN 0324-6329